Titre: Title:	Optimized calibrations of RANS-based k-ω-γ-Reθt transitional turbulence models for aircraft applications
Auteur: Author:	Benjamin Barrouillet
Date:	2021
Type:	Mémoire ou thèse / Dissertation or Thesis
Référence: Citation:	Barrouillet, B. (2021). Optimized calibrations of RANS-based k-ω-γ-Reθt transitional turbulence models for aircraft applications [Thèse de doctorat, Polytechnique Montréal]. PolyPublie. https://publications.polymtl.ca/9241/

POLYTECHNIQUE MONTRÉAL
affiliée à l'Université de Montréal

Optimized calibrations of RANS-based k-ω-γ-$Re_{\theta t}$ transitional turbulence models for aircraft applications

BENJAMIN BARROUILLET
Département de génie mécanique

Thèse présentée en vue de l'obtention du diplôme de *Philosophiæ Doctor*
Génie mécanique

Septembre 2021

POLYTECHNIQUE MONTRÉAL
affiliée à l'Université de Montréal

Cette thèse intitulée :

Optimized calibrations of RANS-based k-ω-γ-$Re_{\theta t}$ transitional turbulence models for aircraft applications

présentée par **Benjamin BARROUILLET**
en vue de l'obtention du diplôme de *Philosophiæ Doctor*
a été dûment acceptée par le jury d'examen constitué de :

François GUIBAULT, président
Éric LAURENDEAU, membre et directeur de recherche
Yannick HOARAU, membre
James CODER, membre externe

DEDICATION

To Yao and Zoé,
you are my everything...

ACKNOWLEDGEMENTS

It has been a long journey since the beginning of this project. I am grateful that I did not walk this path alone.

First, I want to thank my advisor, Prof. Eric Laurendeau for always supporting me. Through all the setbacks you have remained positive and encouraging, until finally, our efforts paid off. I cannot think of anyone better for this role than you. From the bottom of my heart, thank you for trusting me. Secondly, I have to give many thanks to Dr. Hong Yang. You have been a great advisor and mentor. I have learned a lot from you. I am proud to have worked with you and to call you my friend.

Next, I want to thank my family. My wife Yao who has been my anchor for many years. None of this would be possible without you. Thank you to my mother and father who have always been at my side. I cannot repay all that you have given me. I am eternally grateful. Thank you Adrien and Marianne for your unshakable love. Thank you to my grandfather Tipa. You have inspired me to become a better person, man and father. Thank you to Tima for your love and advice. Thank you to Mamie, Boune and all the Barrouillet family. You kindness always pushes me forward. I also want to thank my mother in law Qi for her precious help and advice.

I want to thank the team of Advanced Aerodynamics of Bombardier Aircraft. In particular Pascal, Patrice, Charles, Ian, Amin, Hassan and Reza for all their help and the conversations we have had. I truly appreciate the time and effort that was dedicated to make this project come to fruition.

I would also like to thank my fellow students. Matthieu, Fred, Miguel and many others for all your support and friendship. Tanja for reading my thesis in detail and helping with the finishing touches. The brunch group for many good times and talks.

Finally, I want to thank my friends for their undying support. Coline, Galia, Antoine, Chloé, Tamer, Phillipe, Maude, Sofian, Diane and so many more. I will never forget the years of happiness I have had with you all in Montreal. I also thank my friends in France for all their love.

RÉSUMÉ

Le modèle de transition turbulente γ-$Re_{\theta t}$ de Langtry et Menter est implémenté dans le code RANS structuré à volumes finis FANSC (Full Aircraft Navier-Stokes Code) et couplé au modèle de turbulence $k\omega$-SST. Le modèle est modifié et recalibré pour mieux correspondre aux résultats expérimentaux. L'intensité turbulente locale est remplacée par une représentation des fluctuations turbulentes plus cohérente, de sorte à éviter d'obtenir des solutions non physiques au point de stagnation qui contamineraient les prédictions de la couche limite en aval. Le modèle est recalibré en modifiant des constantes de l'équation pour l'intermittence γ dans le terme de destruction de l'équation de l'énergie cinétique turbulente k. Un algorithme d'optimisation est développé afin de faciliter la calibration sur des cas tests 2D bien connus, tels que les plaques planes de la série T3 et de Schubauer et Klebanoff ainsi que l'aile NACA0012. Le modèle recalibré est ensuite validé sur les ailes 2D NLF-0416 et S809 qui n'ont pas été impliqués dans le processus d'optimisation. De plus, des cas test 3D tels que la Sickle shaped wing et le sphéroïde allongé sont également simulés et les résultats sont comparés à la littérature.

L'extension crossflow de Muller et Herbst est implémentée et recalibrée pour modéliser avec précision une série de résultats expérimentaux. Cette calibration est effectuée avec le même algorithme d'optimisation. La nouvelle extension est ensuite validée sur cinq cas tests 3D : La Sickle shaped wing du DLR, le sphéroïde allongé, l'aile DLR-F5, l'aile NLF(2)-0415 et le CRM-NLF. Les résultats montrent une nette amélioration par rapport au modèle de base. Certaines failles subsistent et une enquête est menée pour identifier les raisons potentielles des inexactitudes restantes. En conséquence, une solution potentielle au problème est suggérée.

Enfin, une étude est menée pour démontrer la sensibilité du modèle à l'intensité turbulente et à la résolution du maillage et pour établir des normes pour lesquelles le modèle peut être considéré comme fiable.

ABSTRACT

The γ-$Re_{\theta t}$ transition model from Langtry and Menter is implemented in the structured finite volumes RANS code FANSC (Full Aircraft Navier-Stokes Code) and coupled with the k-ω-SST turbulent model. The model is modified and re-calibrated to better match experimental results. The local turbulent intensity is replaced with a more consistent turbulent fluctuation representation, to avoid nonphysical solutions at the stagnation point that would contaminate the downstream boundary-layer predictions. A calibration is devised by customizing several constants involved in the equation for the intermittency γ and the destruction term for the turbulent kinetic energy k. An optimization algorithm is thus employed to facilitate the calibration on well-known 2D test cases, such as the flat plates of the T3 series and of Schubauer and Klebanoff as well as the NACA0012 airfoil. The calibrated $\gamma Re_{\theta t}$ model is then validated on the NLF-0416 and S809 airfoil cases that have not been involved in the optimization process. In addition, 3D test cases such as the sickle wing and prolate spheroid are also simulated with the presented model and then compared to the literature.

The Muller and Herbst crossflow extension is implemented and re-calibrated to fit the code and accurately model a variety of experimental results. This calibration is performed with the same optimization algorithm using the Nelder-Mead and Simulated Annealing methods. The new extension is then validated on five 3D test cases: The Sickle shaped wing, the prolate spheroid, the DLR-F5, NLF(2)-0415 and the CRM-NLF. The results show a clear improvement from the base model. Some flaws remain and an investigation is conducted to identify the potential reasons of the remaining inaccuracies. As a result, potential solution to the issue are suggested.

Finally, a study is conducted to shed light on the model's sensitivity to freestream turbulent intensity and mesh resolution and to establish standards for which the model can be considered reliable.

TABLE OF CONTENTS

LIST OF TABLES

LIST OF FIGURES

LIST OF SYMBOLS AND ACRONYMS

CFD	Computational Fluid Dynamics
RANS	Reynolds Averaged Navier Stokes
DNS	Direct Numerical Simulation
LES	Large Eddy Simulation
NLF	Natural Laminar Flow
BL	Boundary Layer

LIST OF APPENDICES

CHAPTER 1 INTRODUCTION

1.1 Overview and Problem Statement

A key element of the struggle against modern-day pollution is reducing the emission of greenhouse gas of transportation devices such as trucks, trains, planes, etc. Consequently, an important part of the scientific community is dedicated to finding ways to lower the fuel consumption of transports by minimizing their drag. In addition, lowering the drag of airplane would allow to complete missions with less fuel consumption, which in turn would permit to use smaller planes for similar missions. One way of minimizing airplanes' drag is to take advantage of the fact that laminar flow creates less drag than turbulent flow. Laminar flow design consists in maximizing the surface area covered by a laminar boundary layer. Natural laminar flow is hard to perform because laminar to turbulent transition is a sensitive phenomenon that can take many forms and can be triggered by a variety of instabilities. The DLR ATTAS tests [16], the European Telfona project [17], the development of the Boeing 737 MAX airplane [18] and ALFA project [19] are examples of industrial design applications of natural laminar flow.

Unfortunately, increasing the laminar area comes at a price. Indeed, transition can significantly affect the pressure distribution on the surface of the object by, among other things, delaying the detachment of a boundary layer or causing its reattachment, thus modifying the pressure induced drag and lift. In addition, laminar flows are more likely to separate. This is a problem because it suggests that laminar wings will stall at lower angles of attack. It also means that it is crucial to know exactly when the plane will stall as an error in estimating this feature can lead to accidents. This cannot be achieved with experiments only. Indeed, wind tunnel experiments, while necessary, are expensive, time consuming and often do not provide the correct Reynolds number. Moreover, they cannot be used to perform optimal optimization but rather stand only to validate the design. In addition, transition measurement methods are not very accurate and hard to use as they may affect the physics at play. They often require to carefully coat the model with paints or to make numerous measurements with invasive probes. Consequently, laminar flow design practically requires the use of computational modeling of transition.

However, modeling transitional turbulent flows also presents significant challenges. It is quite hard to model turbulent flows on large scale geometries. Modern computational resources only allow the use of Reynolds Averaged Navier-Stokes (RANS) methods for full aircraft simulations, as Large Eddy Simulations (LES) and Direct Numerical Simulations (DNS) remain

too computationally expensive [20]. Despite the limiting assumptions made when deriving the RANS equations, the community still tries to capture the effects of complex physical phenomena by using additional turbulence models. Several models have been developed for turbulent transition. The Langtry Menter 2009 model is a worthy option as it displays an impressive level of accuracy over many cases and configurations. However, the ever increasing demands of the industry require constant improvements of the modeling capabilities of the model. In this context, the transition model needs to be relatively accurate on a wide variety of cases, numerically robust and efficient, and its limitations must be explicitly known.

Consequently, the work presented in this thesis tackles the following overarching problem statement:

> *Natural laminar flow design requires the development of a numerical model accurate, robust and efficient on as wide a range of cases as possible.*

The following sections are dedicated to reviewing the knowledge necessary to understand this work.

1.2 Reynolds-Averaged Navier Stokes (RANS)

Fluid mechanics is a special scientific domain because we already know the equations governing all the physics involved. Indeed, the issue lies in solving the Navier Stokes (NS) equations (eq. 1.3) and understanding the phenomena that they model. Direct Navier Stokes Solving (DNS) is the practice of solving the NS equations as they are on a discretized domain. Current supercomputer capabilities only allow DNS methods to solve the equations for very limited domains (at the scale of a cubed centimeter for moderate Reynolds numbers). The enormous cost of solving the equations at flight Reynolds numbers directly pushed the scientific community towards the creation of simplified models.

The Reynolds Averaged Navier Stokes (RANS) method of modeling offers a way to treat turbulent flows for an affordable computational price. It relies on the averaging of the Navier Stokes equations based on the Reynolds decomposition and models flows by artificially considering them stationary. This strong assumption drastically simplifies the problem but potentially bypasses important physical effects associated with unsteadiness. RANS modeling has become very popular in industrial applications because it can efficiently predict drag, lift and moments on large scale geometries such as wings, nacelles or full aircrafts with engineering accuracy.

To derive the Reynolds Averaged Navier-Stokes equations (RANS), one considers the Boussi-

nesq velocity ($\vec{U}$) decomposition (eq. A.8) into the time averaged $\overline{\vec{U}}$ and perturbation $\vec{u'}$ components. By introducing this decomposition into the NS equations, averaging them through time and using the law $\overline{\vec{u'}} = 0$, we obtain a time averaged version of the NS equations called the RANS equations (1.6) with a turbulent cross-term $\frac{\partial \rho \overline{u_i' u_j'}}{\partial x_j}$ called Reynolds' stress tensor coming from the non-linear term of the original NS equations. This term needs to be approximated to close the system because if we derive another equation for $\vec{u'}$, another crossed term will arise and so forth [21].

$$\frac{Dy}{Dt} = \frac{\partial y}{\partial t} + U.\nabla y \tag{1.1}$$

$$\frac{\partial \rho}{\partial t} + \nabla.(\rho U) = 0 \quad \Leftrightarrow \quad \frac{D\rho}{Dt} + \rho \nabla.(U) = 0 \tag{1.2}$$

$$\frac{\partial \rho U}{\partial t} + \nabla(\rho U \otimes U) = -\nabla p + \nabla.\left(\mu\left[\nabla U + \nabla U^T - \frac{2}{3}\nabla.UI\right]\right) \tag{1.3}$$

$$\frac{\partial \rho \epsilon}{\partial t} + \nabla(\rho U \epsilon) = -\nabla.(Up) - \nabla.q + \nabla.(U\tau) \tag{1.4}$$

$$\frac{\partial \overline{U_i}}{\partial x_i} = 0 \tag{1.5}$$

$$\frac{\partial \overline{\rho}\overline{U_i U_j}}{\partial x_j} = -\frac{\partial \overline{p}}{\partial x_i} + \frac{\partial}{\partial x_j}.\left(\overline{\mu}\left[\left(\frac{\partial \overline{U_i}}{\partial x_j} + \frac{\partial \overline{U_j}}{\partial x_i}\right) - \frac{2}{3}\frac{\partial \overline{U_k}}{\partial x_k}\delta_{ij}\right]\right) - \frac{\partial \overline{\rho u_i' u_j'}}{\partial x_j} \tag{1.6}$$

Many turbulence models have been developed in the last few decades to approximate this term as faithfully as possible. Among them, two of the most common ones are the $k-\omega$ and Spallart Almaras models. They are widely used for industrial purposes for fully turbulent flows and constitute a solid base for transitional prediction. In this work, the transitional model is coupled with the $k\omega$-SST turbulence model.

1.3 Turbulence modeling

There are several methods one can use to simulate the effects of turbulence in RANS simulations. Most of them approximate the μ_t variable based on the Boussinesq assumption (eq. 1.11) which states that the Reynolds stress and the deformation tensor can be connected through a scalar μ_T instead of a tensor. A few corner stones of RANS turbulence modeling

methods are reviewed in the following sections.

1.3.1 Algebraic and half-equation models

A tempting option is to approximate the turbulent viscosity μ_t as a function of local variables. In 1978, B.S. Baldwin and H. Lomax [22] designed a turbulence model that determines an approximate value of μ_t in the boundary layer as a function of the velocity, the vorticity and the distance from the wall. This method is robust and cost effective but lacks accuracy in separated flows. It also does not take free stream turbulent intensity into account.

A famous example of such methods is the one equation Johnson King model [23]. This model solves for a transport equation for the maximum shear stress. It is referred to as a half equation model because it solves an ordinary differential equation (ODE) instead of a partial differential equation (PDE). Like the Baldwin Lomax model, it is not universal and is only designed for turbulent boundary layers with an adverse pressure gradient.

1.3.2 One equation models

A more refined way of solving turbulence in RANS simulations is to estimate that turbulence can be approximated via one or more transported variables. This allows the use of extra partial derivative transport equations to calculate an approximation of μ_t from the transported variables.

The Spallart Almaras (SA) model [24] consists of solving a single transport equation (1.8) meant to calculate the turbulent viscosity μ_T. Equation 1.8 is empirical and was developed by considering $\hat{\nu}$ (eq. 1.7) as a transported field and so as to match experimental results. Its value at the wall is forced to 0 while its free stream value is based on the viscosity ratio $\beta = \frac{\nu_t}{\nu}$ at the far field.

$$\nu_t = \hat{\nu}\frac{(\hat{\nu}/\nu)^3}{(\hat{\nu}/\nu)^3 + c_{v1}^3} \tag{1.7}$$

$$\frac{\partial \hat{\nu}}{\partial t} + u_j\frac{\partial \hat{\nu}}{\partial x_j} = \underbrace{c_{b1}(1-f_{t2})\hat{S}\hat{\nu}}_{\text{production term}} \underbrace{- \left[c_{w1}f_w - \frac{c_{b1}}{\kappa^2}f_{t2}\right]\left(\frac{\hat{\nu}}{d}\right)^2}_{\text{destruction term}} \underbrace{+\frac{1}{\sigma}\left[\frac{\partial}{\partial x_j}\left((\nu+\hat{\nu})\frac{\partial \hat{\nu}}{\partial x_j}\right) + c_{b2}\frac{\partial \hat{\nu}}{\partial x_i}\frac{\partial \hat{\nu}}{\partial x_i}\right]}_{\text{diffusion term}} \tag{1.8}$$

Even though it relies on a restricting physical approximation, the SA model grants out-

standingly low computational costs and generally satisfying fidelity to experimental results. The transport equation itself guaranties a positive solution all over the domain. However, maintaining positivity of $\hat{\nu}$ in the discrete domain remains challenging. Allmaras and al. [25] and Burgess and Mavriplis [26] have devised solutions to this problem but they still rely on heuristics.

Because the f_{t2} function of the model acts as a "trip" for transition to take place, some variations of the model [27,28] take transition into account by using an intermittency function to determine the transition onset location and damping the production of turbulence in the boundary layer prior to transition.

1.3.3 Two equation models

There exists many two-equation models ($k\epsilon$ [29], $k\omega$ [30], etc.). This work focuses on the two equations Menter model, also widely known as the k-ω SST model [30, 31], which is the compilation of two models of different qualities . The classic k-ω model [32] which is famous for its accurate capturing of the sublayer and logarithmic parts of the boundary layer and for its stability; and the k-ϵ which has the benefit of not being overdependent to the far field values of ω. Both these models consist in solving two transport equations. One for k the turbulent kinetic energy and the other either for ω the specific turbulence dissipation rate or ϵ the turbulent dissipation. The SST model takes advantage of both aforementioned models by gradually switching from the former to the latter in the wake region of the boundary layer (between the log layer and the far field). The free stream values are $k_{\mathrm{FS}} = \frac{3}{2}\left(\frac{Tu_{\mathrm{FS}}}{100}\right)^2 U_{\mathrm{FS}}^2$ and $\omega_{\mathrm{FS}} = \rho_{\mathrm{FS}} * \frac{k_{\mathrm{FS}}}{\beta}$ while the wall boundary values are $k_{\mathrm{wall}} = 0$ and $\omega_{\mathrm{wall}} = 60\frac{\mu_l}{0.075\rho l^2}$

$$\begin{aligned}
\frac{\partial \rho k}{\partial t} + \frac{\partial \rho U_i k}{\partial x_i} &= \tau_{ij}\frac{\partial u_i}{\partial x_j} - \beta\rho k\omega + \frac{\partial}{\partial x_i}\left[\left(\mu + \sigma_k\mu_t\right)\frac{\partial k}{\partial x_i}\right] \\
\frac{\partial \rho \omega}{\partial t} + \frac{\partial \rho U_i \omega}{\partial x_i} &= \frac{\gamma}{\nu_t}\tau_{ij}\frac{\partial u_i}{\partial x_j} - \beta\rho\omega^2 + \frac{\partial}{\partial x_i}\left[\left(\mu + \sigma_\omega\mu_t\right)\frac{\partial \omega}{\partial x_i}\right] + 2\left(1 - F_1\right)\rho\sigma_{w2}\frac{1}{\omega}\frac{\partial k}{\partial x_i}\frac{\partial \omega}{\partial x_i}
\end{aligned} \tag{1.9}$$

$$\begin{aligned}
\tau_{ij} &= \mu_t\left(\left(\frac{\partial u_i}{\partial x_j} + \frac{\partial u_j}{\partial x_i}\right) - \frac{2}{3}\frac{\partial u_k}{\partial x_k}\delta_{ij}\right) - \frac{2}{3}\rho k\delta_{ij} \qquad & F_1 &= \tanh(arg_1^4) \\
arg_1 &= \min\left[\max\left(\frac{\sqrt{k}}{\beta\omega d}, \frac{500\nu}{d^2\omega}\right), \frac{4\rho\sigma_{\omega 2}k}{CD_{k\omega}d^2}\right] & CD_{k\omega} &= \max\left(2\rho\sigma_{\omega 2}\frac{1}{\omega}\frac{\partial k}{\partial x_j}\frac{\partial \omega}{\partial x_j}, 10^{-20}\right)
\end{aligned} \tag{1.10}$$

$$\tau_{ij} = -\overline{\rho u_i' u_j'} = 2\mu_t\left(S_{ij} - \frac{1}{3}\frac{\partial u_k}{\partial x_k}\delta_{ij}\right) - \frac{2}{3}\rho k\delta_{ij} \qquad S_{ij} = \frac{1}{2}\left(\frac{\partial u_i}{\partial x_j} + \frac{\partial u_j}{\partial x_i}\right) \tag{1.11}$$

1.4 Of turbulent transition and its consequences

As described previously, transition can have a significant impact on the drag and lift. This phenomenon is not yet perfectly understood but many correlations have been formulated to theorize it. This section aims to summarize what is known of the transition phenomenon and modeling approaches.

1.4.1 Transition and its interpretation

Turbulent transition is the process a flow in contact with a solid object goes through when its boundary layer turns from laminar to turbulent as it travels downstream. Transition can be triggered by a variety of instabilities that can develop independently and for different reasons. One of the first instability responsible for transition to be documented was the Tollmien Schlichting (TS) waves [33] [34] that appear in low external disturbance environments. The waves progressively grow until they are strong enough to break the coherence of the boundary layer and shatter into turbulent spots of flow that later cover the whole boundary layer. This type of transition is called natural transition. Different types of transition triggered by other instabilities were later discovered. The list below references some of the most notorious ones:

- Bypass transition occurs at higher levels of external perturbation. In these conditions, another instability named "Klebanov modes" develops before the TS waves and triggers transition, hence the name "bypass" [35]. This type of transition is mostly found in turbomachinery cases [1].

- Cross-flow transition is a serious concern for modern transport planes as it becomes predominant in the case of a swept leading edge. Swept wings have the advantage of delaying the switch to transonic regime (this is discussed in section 1.4.2.2). The downsides are that it favors leading edge contamination and the development of other instabilities that can trigger an early transition. These instabilities are better described in the work of Kahoma [36] [37].

- Bubble transition is a peculiar phenomenon with dire consequences. It refers to cases where the laminar boundary layer detaches from the surface, transitions to a turbulent flow while detached, and reattaches as a turbulent flow, leaving a laminar bubble beneath the detached flow. It happens in extreme circumstances when the angle of attack and the curvature of the object are high or when a strong adverse pressure gradient appears. The reason why this type of transition is concerning is that the bubble stalls the expected fall of pressure as the flow progresses to the trailing edge. We can observe

this effect on figure 1.1 where two bubbles appear at the center of the S809 profile as two bumps on the pressure distribution. This stall of pressure causes a deficit of lift and a surplus of drag when compared to an attached flow. The size of the bubble is related to how strong the adverse pressure gradient is. This phenomenon represents a considerable waste if the bubble grows to significant proportions. It is described more in depth in the work of Hatman and Wang [38].

This bubble formation phenomenon can be especially dangerous when this bubble suddenly separates, leading to sudden loss of lift. This process called "laminar bubble burst stall" must be avoided to avoid accidents. Consequently, it is important to accurately predict this phenomenon.

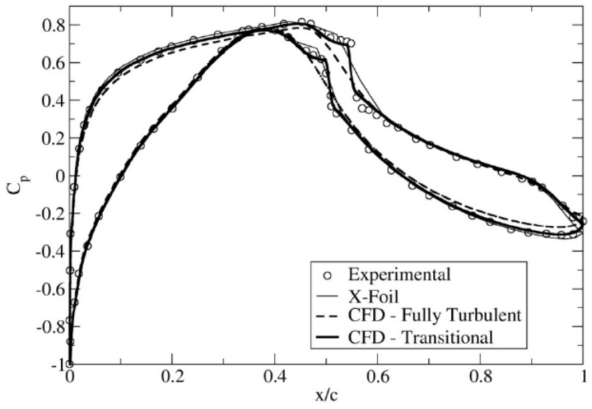

Figure 1.1 Pressure distribution (Cp) for the S809 airfoil at 1 degree angle of attack. [1]

Some of these phenomena are still not fully understood. Indeed, even though we have a fairly good understanding of the conditions in which they develop, there is no consensus over why one or the other takes place because the causes for most of them are hard to determine for certain.

In order to theorize and model transition, the concept of intermittency was introduced. The intermittency at a fixed physical point is the probability of the flow of being turbulent at that location at any time t. Intermittency is equal to 0 in a laminar flow, equal to 1 in a turbulent flow and ranges between the two in transition. This value was defined that way because of how transition has first been observed. Indeed, natural transition features intermittency, with the progressive apparition of turbulent spots, while others such as bypass transition show practically none. It still is practical to use in experimental studies as it allows to quantify transition.

The momentum thickness Reynolds number $Re_{\theta t}$ is a non-dimensional number based on the

momentum thickness θ and the free stream velocity. It was found that it has a connection with transition that can be exploited to better model the phenomenon. This discovery led to numerous empirical correlations between the location of transition and the momentum thickness Reynolds number [39] [40] [11] [41].

Most of the transition modeling developed and used today are based on empirical correlations. For instance, local correlation based models constitute a wide category of transition models and most of them rely on correlations that were initially interpolated from experimental results only. To some extent, this recourse is motivated by the need for efficient modeling with a limited understanding of the physics of some of the transition phenomena. A positive outcome is that anyone can improve the method by either fine-tuning the existing model with new experimental results, or by changing the correlation. The negative outcome is that everyone has a different version of the same model and they all locate transition at relatively different positions. This is also the result of researchers and companies not sharing the specifics of their methods, thus encouraging these differences. Figure 1.2 shows a comparison of the results provided by 3 different codes, all of them using the γ-$Re_{\theta t}$ transitional model. The differences are small yet clearly visible and this can turn out to be problematic when it comes to designing laminar wings with optimization techniques (further developed in section 1.4.3).

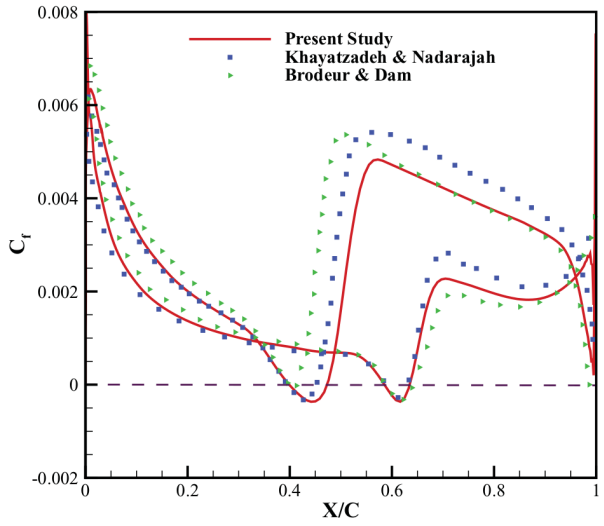

Figure 1.2 skin friction coefficient at AoA=0 for the NLF-0416 profile [2]

1.4.2 The effects of transition

When a plane is flying, it is subject to a variety of fluid forces. The sum of these forces can be divided into two components: the drag which is the component of fluid forces that resists the advance of an object and drags it in the direction of the flow and the lift which is the fluid force that pushes the object in the direction perpendicular to the oncoming flow (upwards for an aircraft). In the case of a plane, the position of transition onset and type of transition mostly have an effect on drag and occasionally on lift. These two quantities are essential to the design of an aircraft as they determine if it is fit to fly and at what cost. Drag and lift depend greatly on the speed at which the plane is moving compared to the speed of sound. We make the distinction between three types of flow : subsonic flows when the freestream Mach number $M = \frac{u}{c}$ is approximately lower than 0.7 (u is the velocity and c the speed of sound), transonic flows where the flow velocity comes close to the speed of sound at Mach numbers between 0.7 and 1.0 and supersonic when the flow is faster than the speed of sound. The physics involved in these different types of flows are different and so is the impact on a plane flying through them. The next sections (from 1.4.2.1 to 1.4.4) will be dedicated to clarify why and how drag and lift are affected by transition in different types of flows.

1.4.2.1 In subsonic flows

According to Joslin in his review of laminar flow control [42] and the Boeing EDGE report, over 50% of the total drag for subsonic transportation airplanes in cruise conditions is due to friction drag, 30% is due to induced drag (Weight, and Span Loading), 10% to wave drag (pressure distribution) and another 10% to defaults of the details of the design (gaps, internal flow etc.). Drag in subsonic flows is mainly caused by viscosity effects and turbulent friction. However, a laminar boundary layer creates 90% less skin friction than a turbulent boundary layer in equal conditions. Therefore, the position of turbulent transition determines what proportion of the wing or other part of the plane will be covered by a turbulent boundary layer and consequently be subject to significant skin friction. It is exemplified by figure 1.2 where the sudden increase of skin friction marks the position of the transition onset. The reason why skin friction is high at the leading edge ($x/c < 0.05$) is that the flow is highly accelerated there, hence even though the boundary layer is laminar, skin friction remains high. As the flow moves downstream from the leading edge, it slows down and skin friction decreases.

1.4.2.2 In transonic flows

For aircraft applications, the frontier between subsonic and transonic flow is demarcated by the so-called "critical Mach number", which is the Mach number at which some portions of the flow around the plane reach the speed of sound. An important limit is the "drag divergence Mach number" which is the Mach number at which the air compressibility causes shock waves to appear along the surface of the plane, starting the drag rise phenomenon. Drag rise is the name given to a sudden increase in drag that happens when the Mach number goes beyond the drag divergence Mach number (as shown in figure 1.3). Transonic shocks change the airflow around the profile and are the reason behind drag rise. Indeed, they cause the pressure along the surface of the object to drastically drop behind them, thus creating intense wave drag because of the pressure differential generated and, depending on the case, reducing lift. The drag divergence Mach number depends mostly on the shape of the wing. As the Mach number exceeds 1.0, drag slowly comes down and the flow becomes fully supersonic. The shocks move to the front of the wing and detach from the wall. The cruising speed of most modern transport planes is chosen so that the Mach number never goes beyond the drag divergence Mach number of its wings. The shape of the entire plane is made so as to delay the drag rise as much as possible. For instance, swept wings are known for postponing drag rise to higher Mach numbers. However, they are prone to leading edge contamination (section 1.4.4) and cross flow transition which are hard phenomena to deal with. More on the matter will be dealt with in section 1.4.3.

As the Mach number grows beyond its drag divergence value, the wave drag skyrockets and becomes predominant over the skin friction drag. The value of the wave primarily depends on the position of the transonic shocks along the surface. At constant temperature and Mach number, the shock location is determined by its interaction with the boundary layer. A lot of progress has been made on the intricate subject that Shock-Wave/Boundary-Layer Interaction is in the last 70 years and it would be unrealistic to review it all in this work. Extensive reviews on this subject can be found in the works of Babinsky and Délery [43] and Dolling [44]. What we can retain from those reviews for our topic is that the position of a transonic shock at constant Mach number depends mainly on the airflow temperature, wall temperature, on whether the flow separates after the shock and on the thickness of the boundary layer. Transition position having a major impact over the thickness of the boundary layer, it can be used to manipulate transonic shocks.

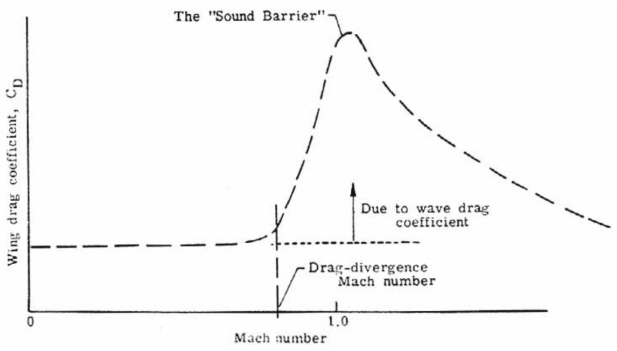

Figure 1.3 Variation of wing drag coefficient with Mach number. [3]

1.4.3 Laminar flow control

The idea behind Laminar Flow Control is that if one can postpone transition to a location farther from the leading edge, the laminar boundary layer will cover a larger area of the wing and the friction drag will drop significantly. This domain appeared in the 1930s when it was discovered that through favorable pressure gradients, wall cooling or wall suction one could stabilize the boundary layer and preserve its laminar state. Fully laminar profiles could be designed but they required the incorporation on flutes and tubes meant to enhance wall suction. The development of LFC encouraged the community to look for new designs meant to achieve laminar flow through appropriate shaping of a profile only. This technique is called Natural Laminar Flow (NLF) as the only boundary layer stabilizer is the shape of the object itself. The concept of laminar design is to create specific parts of the plane such as the nose, wings, engine nacelles and stabilizers with the Laminar flow control technology in order to reduce drag at cruising speeds and to enhance performance during landing and take off. Reducing the drag would not only allow to cut fuel consumption by a significant amount but could also leave enough leeway to make the plane smaller. To clarify this, let us consider the fact that planes are designed to complete a "mission". For instance, a plane could be designed to transport a 100 passengers from London to Tokyo. If the wings experience an intense drag, the plane will need a lot of thrust to compensate. This requirement translates to large amounts of fuel and powerful engines and the dimensions of the plane will follow this trend. If one can reduce the drag by a significant amount, the fuel tank can afford to be smaller, the thrusters can be less powerful and the entire plane can be smaller and considerably cheaper. In this context, natural laminar flow constitutes one of the major objectives of the aerodynamic industry.

One of the issues of natural laminar flow is that each flow has different optimal wing shapes that can achieve low drag and high lift, hence the need for supercritical wings for transonic

flows to replace subsonic wings. Therefore, the ideal aircraft would modify its shape depending on the characteristics of the surrounding flow and the load to be carried. This is the idea behind the development of shape morphing aircrafts. This field of aerodynamics has attracted a lot of attention in the last few decades thanks to the development of new smart materials such as shape memory alloy actuators which are metals that change shape with different temperatures, piezoelectric actuators which refers to materials that change shape through electric current passing through them, or shape memory polymers which are polymer materials that change shape with different temperatures or pressure conditions. CFD simulations predict a huge impact for fuel consumption and aircraft dimensions. For instance, Robitail predicts a 5% drop in drag for transonic flows [45]. Designing a functional morphing wing remains a major challenge as the material represents only a fraction of the problem. Indeed, precise and instantaneous measurement of the flow characteristics is required for the morphing wing to adapt appropriately and failure to do so could lead to catastrophic consequences. Some mechanical morphing is also possible. Attention has been given to wings with variable sweep angle in order to benefit from swept wings ability to postpone shock formation in transonic regimes while avoiding excessive leading edge contamination and crossflow effects in subsonic conditions. This vast subject is discussed further in the reviews of Barbarino [46] and Sofla [47].

1.4.4 Leading edge contamination

Leading edge contamination occurs when the turbulent flow on the fuselage follows the surface of the plane down to the front of the leading edge of the wings, thus contaminating the boundary layer, making it turbulent where it is supposed to be laminar. This phenomenon is characteristic of swept wings and can cause dramatic losses in maximum lift (lift at take off and landing). In his article on the experimental testing of the NLF-0115 airfoil [48], Selig suggests that due to leading edge contamination, the maximum lift of a swept airfoil can easily decrease by 15% if it is not designed properly. It creates considerably hazardous situations at take off or landing as the lift turns out to be significantly lower than it was supposed to be and the pilot loses control of the plane long enough for it to crash. The NACA 23015 profile has been a popular choice in transport planes for quite a while partly because of the small loss of maximum lift experienced in case of leading edge contamination. Further explanations on this topic are given by Spalart, Arnal, Hardy and many others in the AGARD conference proceedings on Fluid Dynamics of Three-Dimensional Turbulent Shear Flows and Transition of June 1989 [49].

1.5 Transition Modeling

Turbulent transition models have been developed to allow turbulence models to take transition into account. They usually work by predicting a transition position and preventing the turbulence model from producing turbulence within the laminar boundary layer upstream of the transition. Ideally, transition models should fit all experimental results perfectly, however, that is hardly realizable considering the complexity of the phenomenon and the difficulties related to it experimental measurements. In addition, the assumptions made when deriving the RANS equations rule out some physics that are sure to have significant influence over turbulent transition. Therefore, the models aim to be reasonably accurate on as many cases as possible. However, this necessary compromise is often unaligned with industrial expectations. Indeed, due to safety and competitivity reasons, the models need to achieve a demanding level of accuracy to be attractive for industrial applications.

There are two main categories of transition modeling for RANS applications: linear stability analysis and local correlation modeling. The former is separate from the RANS solver and examines the solution of the Prandtl equations along the stream lines of a RANS solution and determines the location of transition when a threshold is met. The later is integrated to the RANS solver and uses additional transport equations for variables correlated to turbulent transition onset. In this work, we focus on the Langtry Menter 2009 transition model using two transport equations. It uses a correlation between the Momentum thickness Reynolds number and transition onset. This correlation was made formulated based on experimental results and has been the subject of many studies and revisions since its publication.

The Langtry Menter 2009 model was originally meant to address internal flows but it has been adapted and used for various applications outside this scope. As many research group develop their own version of the model to fit more experimental results or to couple it with a different turbulence model, the scientific progress made is fragmented.

1.5.1 Linear stability Analysis

This method was created by Smith and Gamberoni in 1956 [50] and uses linear stability analysis of the Prandtl equations that leads to solving the so-called Orr-Sommerfeld equation for wave amplitudes. From that equation, one can deduce which of the waves are creating instability by comparing their amplitude. Following equation 1.12, an amplification rate $exp(N)$ is computed for each perturbation and N is compared to a critical value N_T that varies with the author (Smith and Gamberoni suggested $N_T = 9$) and the set of experimental results one uses to calibrate the method. If N is higher than the critical value, the perturbation

related to it triggers the transition. The problem with this is the non-universal nature of N_T as each set of data suggests another value (generally between 7 and 10). Here, x_0 is the stagnation point, x is a position on the streamline resulting from x_0 and α_i is the spatial amplification rate

$$\exp(N) = \exp\left[\int_{x_0}^{x} -\alpha_i dx\right] \tag{1.12}$$

It is one of the first transition prediction methods and the extension of this method to 3D cases was later developed by Arnal in 1994 [51]. The drawback of this method is that it is hard to utilize in the context of a RANS code as one needs the full velocity profile to perform the stability analysis. This forces the use of different instances for RANS and the e^N method; making the detection of separated transition complicated because the experimental position of transition influences the flow greatly and vice versa. Still, Krimmelbein and Krumbein [52] have proposed a coupling of RANS and e^N well suited for natural transition cases. The method suffers from a lack of precision when it comes to transition caused by stronger perturbations such as bypass and roughness transition. In a recent work by Bégou and al. [53], a new method is introduced. It consists in solving a transport equation (eq. 1.13 where σ is the growth rate of a given mode) for each N factor decoupled from the main set. Afterwards, the values of each factor N are extracted at the boundary layer edge and compared to the threshold value to determine if transition takes place. This approach solves two major issues of the e^N method, namely that calculating the path of streamlines is no longer necessary and that neither is calculating the integral along those lines. This makes the e^N method much more compatible with RANS solvers. Unfortunately, these perks come at the price of having to store ρN for each N factor in every cell even though the values are only needed at the boundary layer edge. In addition, the method is still non-local due to the necessity of calculating the boundary layer thickness and coefficients depending on pseudo-normal lines passing through each cell. This method has been validated only on 2D cases for Tollmien-Schlichting waves.

$$\frac{\partial \rho N}{\partial t} + \mathrm{div}(\rho N V) = \rho \|V\| \sigma \tag{1.13}$$

1.5.2 Local correlation-based transition modeling

Several models called "correlation based models" include solving additional transport equations for values characterizing the boundary layer and the transition to turbulent flow. The equations are developed by adding or modifying source terms of a transport equation in

order to match experimental results. They are gradually perfected by implementing new phenomena while preserving correctness on previous achievements.

1.5.2.1 Langtry-Menter 2009 transition model

The Langtry Menter γ-Re_{θ_t} model [54] is a transition model coupled with the $k\omega$-SST turbulence model and consists in solving two additional transport equations, one for the momentum-thickness Reynolds number $Re_{\theta t}$ and one for the intermittency γ. The intermittency γ at a point in space is the probability that the flow at that point is turbulent at any time. Consequently, its value is bounded between 0 and 1. $Re_{\theta t}$ is a mathematical tool related to the momentum thickness Reynolds number Re_θ and regulated by a correlation with transition onset that serves as an indication as to when intermittency should be activated in the boundary layer, thus triggering transition. Transition is located via a correlation inspired from the Abu-Ghannam and Shaw [39] one. We will use this model to simulate transition as it shows promising results. In the recent work of A. Mohasebi and E. Laurendeau [2], the authors present a robust, segregated version of the method implemented in a 2D CFD code. This code will be the starting point of the research.

In the model, the intermittency γ only has a direct influence on the equation for k and the transition momentum thickness Reynolds number $Re_{\theta t}$ only has a direct influence on γ. In this work, the original model is referred to here as Baseline formulation.

The model is not Galilean invariant, which would be a problem if one was to use the method for a case with moving transitional walls. As one of our long-term objectives is to use transition modelling in concert with the chimera method on moving wing elements, Galilean invariance would be a welcome addition. Fortunately, Menter and al. recently published a solution to that problem. It is discussed in section 1.5.2.3.

The model described here first appeared in the 2006 paper of Menter and Al. [55] and later completed in the work of Langtry and Menter 2009 [54]. Much like the SA and SST models, the two transport equations of the γ-$Re_{\theta t}$ model include convection, diffusion, destruction and production terms. They are formulated as eq. B.1 and B.2.

The production and destruction terms they include are described in equation B.5 through B.11. The first production term P_1 for γ is based on the strain S and two functions F_{length} and F_{onset}. Both these functions rely heavily on the local $Re_{\theta t}$ and constitute the influence of $Re_{\theta t}$ over γ. The model was designed so that F_{length} would determine the length of the transition region. However, it seems not to be the case for low free-stream turbulent intensity (approximately below 0.5%) as in these cases, the model produces sharp transitions. It also

has some influence on the position of transition onset and has been reformulated or replaced with a constant by several authors in the past decade [56–59]. F_{onset} is the function supposed to dictate the position of transition onset. It is calculated by the difference of two other functions F_{onset2} and F_{onset3}. F_{onset2} determines whether a point is eligible for transition or not based on a local comparison between $Re_{\theta t}$ and the strain rate. F_{onset3} limits F_{onset2} when ω is strong compared to k. The interaction between F_{onset2} and F_{onset3} is a critical part of the model. Both functions include a fair part of empiricism and should be considered carefully when calibrating the model.

1.5.2.2 Modifications, adaptations and crossflow extensions

In 2011, Medida and Baeder succeeded in coupling the $\gamma - R_{e\theta}$ transitional model to the SA turbulence one [60] which should significantly reduce computation time with one equation less. The same authors also released an extension to the γ-Re_{θ_t} model in order to better describe cross-flow transition [59]. This work was expanded by Piotrowsky and Zingg in their subsequent work on the coupling of the $\gamma - R_{e\theta}$ transitional model to the SA turbulence, smoothing the model and extending the model to model crossflow transition [61, 62].

Several attempts have been made to improve the model so as to include the crossflow transition phenomenon into the model's features. Back in 2009, Watanabe and al. devised an extension to the γ-Re_{θ_t} model using a new transition onset criterion based on the experimental results of Kahoma and al.. In 2013, Medida and Baeder introduced a novel empirical onset criterion [59] based on the streamline radius of curvature parallel to the wall. The model experiences some numerical instabilities around the onset. A helicity based crossflow extension was devised by Müller and Herbst in 2014 [58] but even though experimental results were met on winglike geometries, the results on the 6:1 spheroïd [63] test case were inconclusive. Grabe and Krumbein [64] [65] [11] developed two extensions to the $\gamma - R_{e\theta_t}$ model to take better account of cross-flow effects in 3 dimensional boundary layers. The first one called CFC1 is based on the C1 correlation [66] and is limited to winglike geometries while the second one called CFHe based on helicity is subject to less geometrical restrictions. The models were validated on a wide range of test cases and are well known for their reliability. Robin Langtry himself contributed to this effort with his own extension [41] based on streamwise vorticity. This version of the model has the considerable benefit of also modelling roughness induced transition. Choi and Kwoon are developing their [67] [68] extension based on a house made crossflow criterion affecting both transition onset and length. Their latest addition is focused on the interaction between the Tollmien–Schlichting instability and the crossflow instability. Sa and Park showed promising results with a supposedly simple

extension of the model [69]. The authors do not give the specifics of their method in their article. Jung and Baeder recently proposed a Spalart Allmaras coupled γ-Re_{θ_t} model [70] working with a Hamiltonian-Strand grid flow solver. It is based on Baeder previous work on the method and Müller's Crossflow extension of the γ-Re_{θ_t} model based on helicity. Nie, Krimmelbein, Krumbein and Grabe recently exhibited remarkable results [71] obtained by combining the $\gamma - Re_{\theta_t}$ model with the so-called SSG/LRR-ω Reynolds stress model [72]. Very close matching to experimental results is achieved. Ströer, Krimmelbein, Krumbein and Grabe also recently developed a new transition model [73] using 4 transport equations based on the ADH criterion [66]. This model shows promising grid convergence and performs well on some challenging test cases but does not take crossflow transition into account at the moment.

1.5.2.3 One equation correlation based transitional models based on the intermittency function

Based on the γ-Re_{θ_t} method, the γ method by Menter et al. [74] gets rid of the Re_{θ_t} equation by approximating the turbulence intensity Tu and the pressure gradient parameter λ_θ locally so as to not include the interaction with $\tilde{Re}_{\theta_t}$. The correlations were also simplified, and a few other minor tweaks were applied as well. The model shows satisfying results when tested for bubble transition and it is mentioned that a crossflow extension was made for this method and that it would be presented later but nothing has appeared yet.

While it shows promise, this model still needs to be perfected so as to detect all types of transition. In an effort to improve this method, Zhou and al. recently published an improved version of the model [75] to include crossflow transition in hypersonic flows. Vallinayagam and Lardeau also made a contribution at the 8^{th} AIAA Theoretical Fluid Mechanics Conference in 2017 with their own intermittency-based one equation transition model featuring crossflow effects [76]. Lee and Baeder also contributed to the improvement of this method by coupling it to the Spalart Almaras turbulence model and developing two crossflow extensions for it [77].

1.6 Critical assessment

Transition modeling in RANS applications has been the object of research interest for decades but still has unresolved issues.

Linear stability analysis is often very accurate but suffers from the need to determine the N factor. Recommended values and correlations have been developed that can help with this

decision, however different cases may require a different N factor for optimal results. This method also suffers from being separated from the RANS solver. Linear stability analysis usually requires a preliminary solution of the flow. It can be an Euler solution or a laminar one and from it, the streamline data must be extracted. Then the boundary layer of this solution is examined and linear stability analysis can predict a transition onset location. Finally, A RANS solver can calculate the turbulent solution with a forced laminar boundary layer and transition as per the prediction. This multi-step process makes the use of this method hard to automatize and to use for optimization and design purposes. As mentioned in section 1.5.1, solutions have been developed for this issue but they come with their own problems. There is also a debate about what preliminary solution should be used for the boundary layer analysis. Indeed, results vary if the solution is Euler, laminar of fully turbulent. For instance, in the case of transonic flows, these solutions do not model the transonic shock at the same place, leading to significant inconsistencies.

Local correlation models tend to be less accurate but much more practical. Indeed, The γRe_θ model is integrated in the RANS solver, which means that both turbulence and transition are taken into account in one single computation. This means that tasks requiring multiple simulations are much easier to perform and to automatize. However, the model is known for occasionally struggling with mesh grid convergence and some authors have had to modify the model in order to make its residuals converge [61, 71]. Its implementation is complex as is shown by the multitude of different versions of the model available in the literature. In addition, second order discretization remains a challenge for the transition model.

1.7 Objectives and thesis outline

The goal of the current work is defined as follows:

> *Develop numerical and optimization approaches for the implementation of local correlation-based transition models and assess the limitation of the resulting model.*

The methodology and techniques used in this work are presented in Chapter 2. This chapter presents the model's formulation and the methods used for turbulence decay correction, transition detection and calibration optimization. Chapter 3 details the implementation of the original Langtry Menter 2009 model in the RANS code FANSC and its validation on 2D cases. FANSC is a parallelized CFD code for full-aircraft configurations developed at Bombardier Aerospace [78]. It performs on multi-block structured grids and carries out 3D finite volumes cell centered RANS calculations. FANSC uses artificial dissipation with

a centered scheme to achieve second order discretization in space and comprises both the SA and k-ω SST turbulence models. In chapter 4, following the 2D model integration, a crossflow extension is implemented and validated on 3D cases. The extension developed by Muller et al. [58] is chosen to be implemented in FANSC. Muller's model relies on helicity and is fairly easy to modify due to its simple formulation and integration to the base model. Modifications are made to both the base model and the extension, and they are recalibrated. These changes are made to solve stability and accuracy issues of the original implementation. An optimization algorithm is developed combining the Nelder Mead and Simulated annealing methods. This algorithm is used to perform the recalibration of the transition model more efficiently. Finally, in chapter 5 a sensitivity study is conducted to outline the capabilities of the model and its limits. These results give a reference of how sensitive the model is to specific parameters, and provide a better understanding of how different parameters influence the model's performance.

CHAPTER 2 Methodology

The γ-$Re_{\theta t}$ model by Langtry and Menter [40, 54] was implemented in FANSC [79]: a finite volume structured solver with second-order implicit Euler pseudo-time marching and second-order Roe solver for the RANS equations using the $k\omega$-SST turbulence model. In this work, the model is used as an extension of the $k\omega$-SST turbulence model [80], as was originally intended.

Following its implementation in FANSC, the model was modified to improve its synergy with the solver algorithms to improve residual convergence rate and robustness. These adjustments are described in [79] with validation results on non-crossflow cases. A sensitivity study was conducted to establish the reliability of the model in [81]. In FANSC the flow is solved segregated from the turbulence and the 4 equations of turbulence with transition are solved, in turn, in a segregated fashion. The equation for γ is solved first, followed by the $Re_{\theta t}$, k, and finally ω equations. This segregation method was developed by Mosahebi and Laurendeau [2, 82].

The jacobians for the γ and $Re_{\theta t}$ equations are assembled using the method used by Spalart and Allmaras in [24]. All four equations have under-relaxed solution updates with a relaxation factor of 0.7. In addition, the calculation of γ_{eff} for the production term in the equation for k is also under-relaxed with a factor of 0.1. All the meshes used in this work were generated with either the Pointwise commercial software or Bombardier's in-house mesh generator MBGRID [83]. All the cases in this work consider external flows. All meshes have a farfield boundary condition between 40 and 50 chords away from the solid. The first wall cell is located at $y^+ < 1$ with an expansion ratio under 1.1 for at least 16 cells starting from the surface. The grids use a multi-block structured architecture and were smoothed as described in the work of Hasanzadeh et al. [83, 84] to maintain wall orthogonality.

2.1 Model formulation

The γ-$Re_{\theta t}$ model adds 2 transport equations to the 7 equations system of RANS and k-ω-SST [80]. In the model, the intermittency γ only has a direct influence on the equation for k and the transition momentum thickness Reynolds number $Re_{\theta t}$ only has a direct influence on γ. The original model, referred to here as Baseline formulation, is formulated as in equation 2.1 [40, 54]. The $k\omega$-SST turbulence model reads equation 2.2. Further details of the formulation of the $k\omega$-SST model can be found in [80].

$$\frac{\partial \rho\gamma}{\partial t} + \frac{\partial (\rho u_i \gamma)}{\partial x_i} - \frac{\partial}{\partial x_j}\left[\left(\mu_l + \frac{\mu_t}{\sigma_\gamma}\right)\frac{\partial \gamma}{\partial x_j}\right] = P_1 + P_2 - D_1 - D_2$$

$$\frac{\partial \rho\tilde{Re}_{\theta t}}{\partial t} + \frac{\partial \left(\rho u_i \tilde{Re}_{\theta t}\right)}{\partial x_i} - \frac{\partial}{\partial x_j}\left[\sigma_{\theta t}\left(\mu_l + \mu_t\right)\frac{\partial \tilde{Re}_{\theta t}}{\partial x_j}\right] = P_3 - D_3 \tag{2.1}$$

$$\frac{\partial \rho k}{\partial t} + \frac{\partial \rho U_i k}{\partial x_i} = P_{k_{\mathrm{SST}}} - D_{k_{\mathrm{SST}}} + \frac{\partial}{\partial x_i}\left[\left(\mu + \sigma_k \mu_t\right)\frac{\partial k}{\partial x_i}\right]$$

$$\frac{\partial \rho\omega}{\partial t} + \frac{\partial \rho U_i \omega}{\partial x_i} = P_{\omega_{\mathrm{SST}}} - D_{\omega_{\mathrm{SST}}} + \frac{\partial}{\partial x_i}\left[\left(\mu + \sigma_\omega \mu_t\right)\frac{\partial \omega}{\partial x_i}\right] + 2\left(1 - F_1\right)\rho\sigma_{w2}\frac{1}{\omega}\frac{\partial k}{\partial x_i}\frac{\partial \omega}{\partial x_i} \tag{2.2}$$

The production and destruction terms they include are described in equation 2.3 through 2.9. The first production term P_1 for γ is based on the strain S and two functions F_{length} and F_{onset}. Both these functions rely heavily on the local $Re_{\theta t}$ and constitute the influence of $Re_{\theta t}$ over γ. The model was designed so that F_{length} would determine the length of the transition region. However, it seems not to be the case for low free-stream turbulent intensity (approximately below 0.5%) as in these cases, the model produces sharp transitions. It also has some influence on the position of transition onset and has been reformulated or replaced with a constant by several authors in the past decade due to its empiricism [56–59]. F_{onset} is the function supposed to dictate the position of transition onset. It is calculated by the difference of two other functions F_{onset2} and F_{onset3}. F_{onset2} determines whether a point is eligible for transition or not based on a local comparison between $Re_{\theta t}$ and the strain rate. F_{onset3} limits F_{onset2} when ω is strong compared to k. The interaction between F_{onset2} and F_{onset3} is a critical part of the model. Both functions include a fair part of empiricism and should be considered carefully when calibrating the model.

$$P_1 = F_{\mathrm{length}} c_{a1} \rho S \left[\gamma F_{\mathrm{onset}}\right]^{c_\alpha} \quad P_2 = c_{a2}\rho\Omega\gamma F_{\mathrm{turb}} \quad P_3 = c_{\theta_t}\frac{\rho^2 u_i^2}{500\mu_l} Re_{\theta_t}(1 - F_{\theta_t})$$

$$D_1 = c_{e1}\gamma P_1 \qquad D_2 = c_{e2}\gamma P_2 \qquad D_3 = c_{\theta_t}\frac{\rho^2 u_i^2}{500\mu_l}\tilde{Re}_{\theta_t}(1 - F_{\theta_t}) \tag{2.3}$$

$$F_{\mathrm{length}} = F_{\mathrm{length}}\left(1 - F_{\mathrm{sublayer}}\right) + 40 * F_{\mathrm{sublayer}} \quad F_{\mathrm{sublayer}} = \exp\left(-\left(\frac{R_{e\omega}}{200}\right)^2\right)$$

$$R_{e\omega} = \frac{\rho\omega d^2}{\mu_l} \qquad F_{\mathrm{turb}} = \exp\left(-\left(\frac{R_T}{4}\right)^4\right) \tag{2.4}$$

$$R_T = \frac{\rho k}{\mu\omega}$$

$$F_{\text{onset}} = \max\left(F_{onset2} - F_{onset3}, 0\right) \qquad F_{\text{onset3}} = \max\left(1 - \left(\frac{R_T}{2.5}\right)^3, 0\right)$$

$$F_{\text{onset2}} = \min\left(\max\left(F_{\text{onset1}}, F_{\text{onset1}}^4\right), 2.0\right) \qquad F_{\text{onset1}} = \frac{R_{ev}}{2.193 R_{e\theta c}} \tag{2.5}$$

$$R_{ev} = \frac{\rho S d^2}{\mu}$$

$$F_{\theta t} = \min\left[\max\left(F_{\text{wake}}\exp\left(-\left(\frac{d}{\delta}\right)^4\right), 1 - \left(\frac{c_{e2}\gamma - 1}{c_{e2} - 1}\right)^2\right), 1\right] \quad F_{\text{wake}} = \exp\left[-\left(\frac{R_{e\omega}}{10^5}\right)^2\right] \tag{2.6}$$

$$\delta = \frac{375 * \Omega \mu_l R_{e\theta t} d}{\rho u_k u_k}$$

$$R_{e\theta t} = \begin{cases} (1173.51 - 589.428 Tu + 0.2196 Tu^{-2}) F(\lambda_\theta), & Tu \leq 1.3 \\ 331.50 (Tu - 0.5658)^{0.671} F(\lambda_\theta), & Tu \geq 1.3 \end{cases} \tag{2.7}$$

$$F(\lambda_\theta) = \begin{cases} 1 + \left[12.986\lambda_\theta + 123.66\lambda_\theta^2 + 405.689\lambda_\theta^3\right] \exp\left(-\left(\frac{Tu}{1.5}\right)^{1.5}\right), & \lambda_\theta \leq 0 \\ 1 + 0.275\left[1 - \exp(-35.0\lambda_\theta)\right] \exp\left(-\frac{Tu}{0.5}\right), & \lambda_\theta \geq 0 \end{cases} \tag{2.8}$$

$$\theta_t = \mu_l \frac{R_{e\theta t}}{\rho\sqrt{u_k u_k}} \qquad \lambda_\theta = \frac{\rho \theta_t^2}{\mu_l} \frac{dU}{ds} \tag{2.9}$$

$$\begin{aligned} c_{e1} &= 1.0 \quad c_{e2} = 50 \quad c_{a1} = 2.0 \quad c_{a2} = 0.06 \\ c_{\theta t} &= 2.0 \quad \sigma_\gamma = 1.0 \quad \sigma_{\theta t} = 2.0 \end{aligned} \tag{2.10}$$

$$D_k = \min(\max(\gamma_{\text{eff}}, 0.1), 1.0) * D_{k_{\text{SST}}} \quad P_k = \gamma_{\text{eff}} * P_{k_{\text{SST}}} \tag{2.11}$$

2.2 Turbulence Decay Correction

As was shown in [81], this transition model can be sensitive to low variations of FSTI. Consequently, the ambient turbulence decay feature of the $k\omega$-SST model needs to be taken into account in order to have the correct FSTI at the leading edge of an object. Several solutions are available.

One solution consists in calculating the farfield value necessary to ensure the desired FSTI at the leading edge after decay. This method is not appropriate for meshes with a long distance between the farfield and the object. Indeed, the turbulence decay will often require unreason-

able farfield values to ensure the correct flow conditions at the leading edge. Consequently, this method was not used in this work. It is described in further detail in [85]. Another is to add constant source terms in the equations for k and ω using their ambient values in order to counter the default value of their destruction terms. This method is quite effective but can be criticized because these source terms could potentially impact areas of the flow where k should be close to 0 such as the viscous sublayer or the stagnation point. In this work, a floor value for k ad ω is imposed in order to force both values to resist decay [2, 85]. In addition, the floor value is cancelled close to the surface to avoid interfering with the sublayer and stagnation point.

2.3 Transition Detection

The numerical transition is automatically acquired using the criteria developed by Robitaille et al. [45]. This method uses the normal derivative of k at the wall $\frac{dk}{dn}$ to identify whether the boundary layer is laminar or turbulent above a cell on the surface. The code checks all the cells on the surface of the solid. For each of them, the code verifies if $\frac{dk}{dn}$ has crossed a threshold value between the center of the cell and its neighbors center. If it has, a transition position is calculated by interpolation between the two cells.

The threshold value can be a concern as the value of $\frac{dk}{dn}$ in the laminar and turbulent boundary layers can change with the Reynolds number and FSTI. The threshold can be set to a value between 0.001 and 0.01 which will work most of the time and can be adjusted for exceptions. Another option is to use the formula developed in this work. The criteria used for this threshold is detailed in equation Eq. 2.12. It was determined by considering valid values on several cases.

$$\left.\frac{dk}{dn}\right|_{\text{threshold}} = \max\left(-0.04486 + Re * 4.42 * 10^{-8}, 0.001\right) \tag{2.12}$$

2.4 Optimization algorithm

Previous to using the optimization algorithms, several constants of the model were tested for their influence, or lack thereof, on the transition prediction. Out of this study, three constants were selected that were estimated to be the most effective to recalibrate the model. Interestingly, these constants, while modifying the transition criteria, do not directly affect the core correlation of the model. Attempts have been made to modify the correlation directly but they were unfruitful as the correlation seems sensitive to change and other constants were found to be more effective for the present recalibration. It is possible that the reason why

the recalibration of the original model was successful is because the modifications did not impact the correlation and thus, the intended features of the model were recovered.

The chosen constants of the model act as design variables to the optimization method. This means that the optimization algorithm returns a set of constants that locally minimized the error of the model on the chosen test cases. The cost function of the optimization is the L^2 distance between the transition location predicted by the model and the one taken as reference on one or several test cases. In the case where several test cases are used, the average of the distances measured int these cases is taken as cost function. For 3D cases, the cost function is calculated by measuring the distance between each point of the experimental data and the closest point of the modeled transition line and making an average of all the obtained distances. This cost function is what the optimization algorithm minimizes by methodically modifying the model's constants. The numerical transition is automatically acquired using the method described in section 2.3. These reference transition locations can either be experimental measurements or the modeled transition line of other computational simulations. In the following paragraphs, we refer to a "point" as a set of design variables, which are the chosen constants of the model. For each point, there is one evaluation of the cost function, which is the L^2 distance between the model's prediction and the reference. The algorithm returns a point which is found to locally minimize the cost function. In this work, the optimization of the base model was performed by minimizing the distance between the model's prediction and experimental results for the NACA0012 airfoil [4] and the flat plate cases of the ERCOFTAC T3 series and Schubauer and Klebanov [5–7]. To optimize the crossflow extension, results from 2 cases alone were used: the NLF(2)-0415 [8] and the Prolate Spheroid [86].

To evaluate the cost for a given set of constants, one has to run the code and extract the transition prediction to be compared to the reference. This process can take from a few minutes to a few hours. Therefore the optimization method should converge in a limited amount of iterations to be affordable in terms of computation time. Fortunately, the number of constants to recalibrate is very limited. In addition, the gradients of the cost function are not directly available, which narrows down the number of useful optimization methods.

Consequently, the Nelder-Mead algorithm [87], also known as the Amoeba method is well suited for the problem at hand. In the context of this work, the method systematically converged in less than 100 iterations. Its major weakness is that it may converge towards a nearby local minimum and there is no guarantee of finding a global minimum. Fortunately, the algorithm seems reliable and relatively fast. The number of iterations needed to converge is not strongly correlated to the complexity of the cost function. However, convergence

becomes significantly slower as the number of parameters increases. Figure 2.1 shows how this optimization algorithm was implemented for the present work. The idea of this algorithm is to use a moving simplex. Say we have a minimization problem with n variables. The simplex would be a collection of $n + 1$ points with n coordinates - one for each variable. For each of these $n + 1$ points, we measure the outcome of the cost function given the set of constants that are the coordinates of the point. One can then determine which point has the lowest cost and which one has the highest. The point with the highest cost has its coordinates modified through a symmetry transformation with the center of gravity of the rest of the points. The resulting new point has a cost of its own. If the new point still has the highest cost, it is modified again and brought closer to the point with the lowest cost. If instead, it has the lowest cost of all the points, it is then translated further in the same direction, hoping that a minimum exists further this way. Finally, if the cost of the new point is neither the lowest nor the highest, it means that another point now has the highest cost and nothing needs to be done. Afterward, the algorithm goes back to the reflection step.

The method is guaranteed to find a local minimum and the number of iterations needed to converge is not strongly correlated to the complexity of the cost function. A major weakness of the method is there is no guarantee of finding a global minimum. To cope with this issue, one can perform the optimization several times, starting with different points every time until a satisfactory solution is found. This is only a viable option if the optimization process is fast and computationally cheap. In this work, this technique was used successfully when recalibrating the base model. Indeed, in that occurrence, only 2 constants were being modified and the 2D flat plate test cases used for comparison between modeling and experiment allowed the optimization process to reach completion in under 1 hours using 512 cores. Used in the context of the calibration of the crossflow extension however, the Nelder-Mead method has converged in less than 50 iterations, which would take about 6 hours using 512 CPU-cores. The prolonged amount of time required to perform one instance of the Nelder-Mead optimization prohibits the use of the trail and error method described above. Instead, the Nelder-Mead algorithm was preceded with 50 iterations of the simulated annealing method [88]. The simulated annealing is an optimization method that relies on increasingly restrained random guesses to find the global minimum of optimization problems. This method is very effective at finding global minimums but requires high numbers of iterations to fully converge. In this application, this method is used to find a promising valley of the cost function and the Nelder-Mead is employed to finish the convergence. Indeed, the Nelder-Mead method is more effective at converging towards a local minimum. This combined method is an attempt at taking advantage of the qualities of both methods. This process doubles the computation costs but finds deeper solutions in one shot.

By modifying some of the constants in the model, we take the risk of damaging some of its features. Sections 3.2 and 4.2 treat the validation campaigns that were undertaken to justify the re-calibrations of the model and its extension by showing that the features of the original model are retained on test cases that were not used in the optimization process.

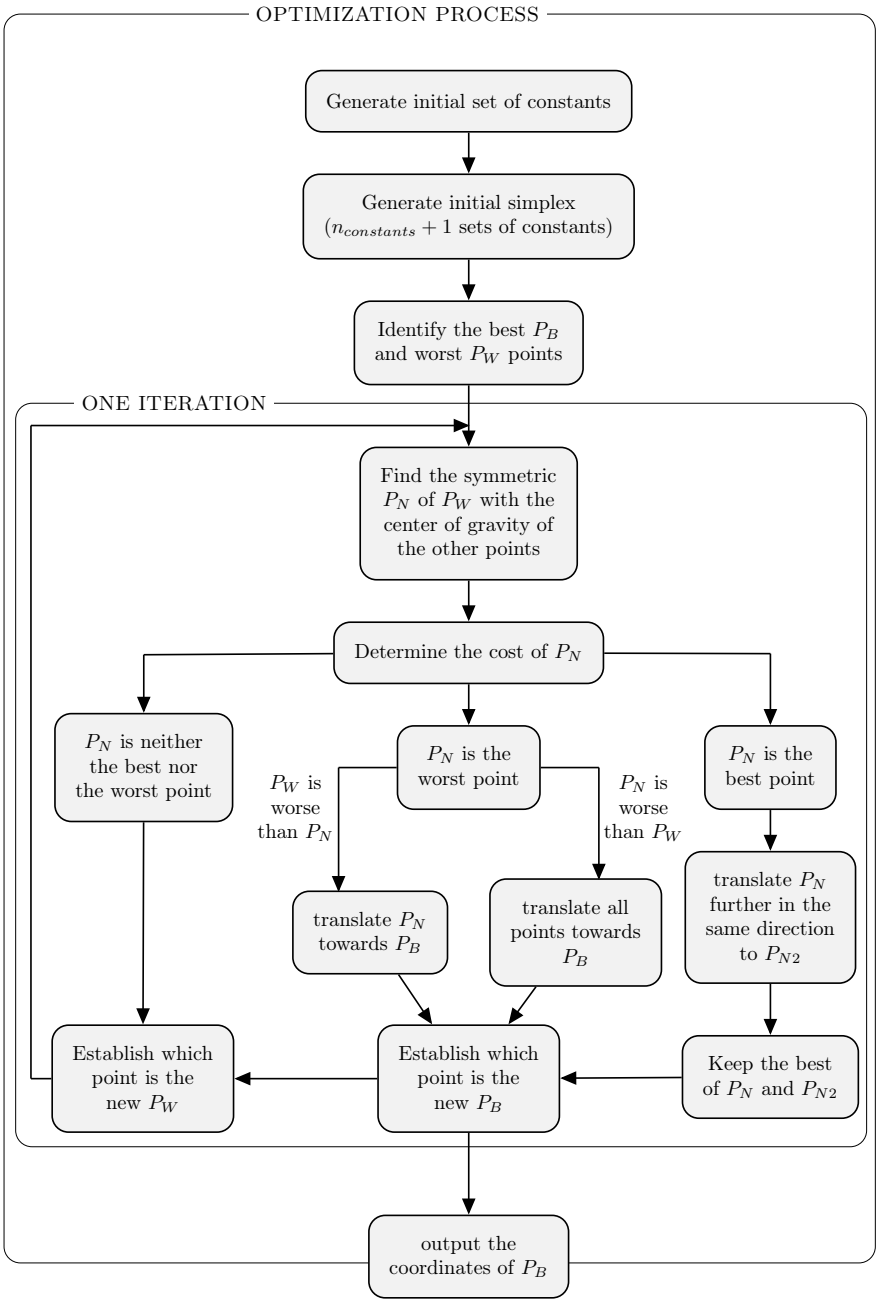

Figure 2.1 Flowchart of the optimization algorithm used for improving transition detection

CHAPTER 3 Calibration of Base Model

In this chapter, the details of the implementation and calibration of the original local correlation Langtry Menter model [54] are addressed. Then, the recalibrated model is validated on a series of test cases and a succinct mesh sensitivity study is conducted.

3.1 Implementation

Even though the turbulence model used for this implementation is supposedly the same as in the original work [54], difficulties were encountered when trying to replicate results. To cope with these difficulties, a series of modifications were brought to the model.

3.1.1 Modification of the f_{onset3} function

The f_{onset} function determines where transition starts. It is composed of 3 sub-functions: f_{onset1} and f_{onset2} are responsible for the influence of $Re_{\theta t}$ over γ, while f_{onset3} acts as a limiter based on the values of k and ω. The constants in f_{onset3} can be modified to shift the transition onset along the surface without impacting other features of the flow. Caution is advised when modifying this constant, as this modification may not be necessary or valid when implementing the model in other codes. In this work, f_{onset3} was calibrated with the optimization algorithm described in section 2.4 and reformulated as Eq. 3.2. Increasing C_{opt1} increases value of f_{onset3} and enlarges the volume where f_{onset3} is non zero. Considering the role of f_{onset3} as a limiter of f_{onset}, this means that the rise of f_{onset} will be pushed back with a similar effect on the production term P_1 in the equation for γ (see Eq. 3.1). This in turn, will delay transition. Decreasing C_{opt1} has the opposite effect. Good values of the constant c_{opt1} were found between 1.0 and 2.0. Modifying c_{opt1} practically has a linear influence on the position of transition onset. Here, we provide a range that is specific to FANSC to encourage the use of optimization to tailor the recalibration to each code. Other constants in this function can be modified for similar effects, however, c_{opt1} appeared to be less sensitive. Fig. 3.2 shows how this modification affects the results on the Schubauer and Klebanoff flat plate case. FANSC's results with the original model in pink are far upstream from the results with the modified version of f_{onset3} and from the recalibrated version of the model in blue (using all the modifications specified in this work).

$$P_1 = F_{\text{length}} c_{a1} \rho S \left[\gamma F_{\text{onset}}\right]^{c_\alpha} \qquad F_{\text{onset}} = \max\left(F_{\text{onset2}} - F_{\text{onset3}}, 0\right) \tag{3.1}$$

$$f_{\text{onset3}_{\text{new}}} = \max\left(c_{\text{opt1}} - \left(\frac{R_T}{2.5}\right)^3, 0\right) \tag{3.2}$$

3.1.2 Modification of the destruction term in the equation for k

The intermittency γ appears in two terms of the equation for k. One is the production term P_k in the shape of an effective intermittency γ_{eff} and the other is the destruction term D_k. The constant serving as a minimum value for this destruction term has a strong influence on the intensity of skin friction after transition with very little side effect on transition location. This makes for a powerful calibration tool when coupled with the aforementioned f_{onset} calibration. Indeed, by increasing C_{opt2}, one increases the minimum of the intermittency factor for the destruction of k. This means that the laminar sub-layer underneath the turbulent boundary layer post-transition will slowly grow in thickness, thus modifying the boundary layer profile. The result is an increased skin friction in the turbulent boundary layer. In this work, D_k was calibrated with the optimization algorithm described in section 2.4 and reformulated as Eq. 3.3. Good values of the constant c_{opt2} were found between 0.06 and 0.08.

$$D_{k_{\text{new}}} = \min(\max(\gamma_{\text{eff}}, c_{\text{opt2}}), 1.0) * D_{k_{\text{SST}}} \tag{3.3}$$

Fig. (3.2) shows how this modification brought the skin friction coefficient after transition from an abnormally low value to a reasonable one which matches the experiment. In this graph, The red squares represent the experimental results and The green ones refer to the results of the original model as in the work of Langtry et Al [54]. The blue points are the result generated by FANSC with the recalibrated model and in pink, the results of FANSC with no recalibration. Finally, the results of FANSC with only the modification applied to f_{onset3} are displayed in dark grey and the results with only the modification on the destruction of k are in orange. Note that the modification of the calculation of the local turbulent intensity has had no influence on these results. These results were obtained with the Schubauer and Klebanoff flat plate case [5]. In this simulation, the turbulent intensity is set to 0.1% and the dimensionless turbulent viscosity at 1.0 at the far-field. This modification improved the agreement between the simulation and the experiment significantly.

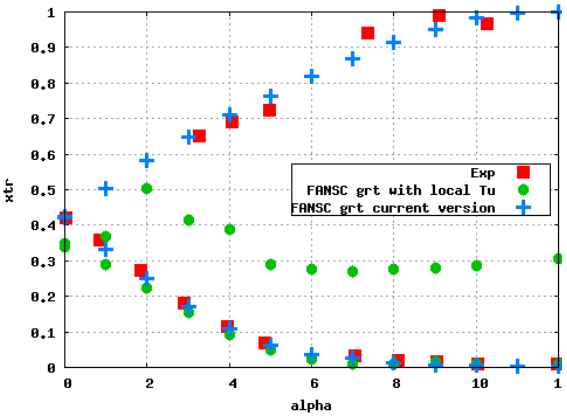

Figure 3.1 Transition position as a function of the angle of attack for the NACA0012 case [4] with the original model and the modified version compared with experimental data. ($M = 0.16$, $Re = 2.88 * 10^6$, $FSTI = 0.003$, $\mu_t/\mu_l = 100$)

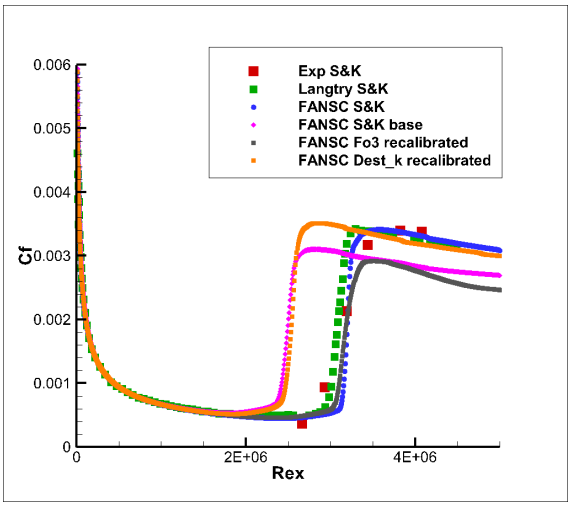

Figure 3.2 Friction coefficient as a function of the Reynolds number along the surface for the Schubauer and Klebanoff flat plate case [5] with the original model and the modified version compared to experimental data. ($M = 0.2$, $Re = 5 * 10^6$, $FSTI = 0.001$, $\mu_t/\mu_l = 1.0$)

3.1.3 Smoothing of the f_{onset} function

Some functions in the $\gamma Re_{\theta t}$ model are not differentiable. For instance, F_{length} and F_{onset} both include min() and max() functions. It was found that these non-differentiable functions can introduce instabilities, preventing convergence. The same observation was made by Piotrowski and Zingg [57, 89]. In their article, they describe a smoothing of both F_{length} and F_{onset3}, successfully improving the model's robustness and convergence speed. In the present work, a different smoothing is suggested for F_{onset}. Other non-differentiable functions of the model did not prove as problematic as F_{onset} and were left unchanged. As a result, the F_{onset3} function was modified as in Eq. 3.5 where c_{opt3} can be chosen between 0 and 0.1:

$$F_{\text{onset}} = \max\left(f_{o2} - f_{o3}, 0\right) \tag{3.4}$$

$$\begin{cases} F_{\text{onset}_{\text{new}}} = F_{\text{onset}} & \text{if } F_{\text{onset}} > c_{\text{opt3}} \\ F_{\text{onset}_{\text{new}}} = \exp\left(\frac{f_{o2} - f_{o3} - c_{\text{opt3}}}{c_{\text{opt3}}}\right) * c_{\text{opt3}} & \text{if } F_{\text{onset}} \leq c_{\text{opt3}} \end{cases} \tag{3.5}$$

Fig. 3.3 and 3.4 show the effectiveness this modification. The first graph presents the convergence of the code without smoothing of the f_{onset} function. The code quickly stops

converging and stalls at a residual of about 10^{-3}. With smoothing, however, convergence to 10^{-10} is achieved after a few thousand iterations. Fig. 3.5 shows that the effect of the smoothing of f_{onset} on skin friction is marginal. Indeed, the prediction with smoothing in red almost perfectly matches the prediction without smoothing in black. In addition, the lift coefficient predicted is exactly the same and the drag perdiction is 49.74 drag counts without smoothing and 49.67 with smoothing. The results are very close but smoothing the f_{onset} function provides a much deeper convergence.

3.1.4 Turbulent intensity Tu

The local value for Tu is used in the empirical correlation for the transition onset momentum-thickness Reynolds number $Re_{\theta t}$. It is calculated with equation 3.6. It was observed that in some cases, the predicted value of Tu is unphysically high near the leading edge. The issue stems from the fact that Tu is a ratio between the turbulent kinetic energy k and the mean velocity U. However, k and U do not converge towards 0 at the same rate when approaching the leading edge of an obstacle. As a result, Tu may end up with unreasonably high values at the leading edge. This, in turn, creates low values of $Re_{\theta t}$ along the boundary layer and eventually triggers transition too far upstream. To avoid this issue, it was decided to replace the turbulent intensity in the correlation with F_{Tu}, a function of the ratio between the local turbulent fluctuation speed and the free-stream velocity U_∞. The formulation of F_{Tu} is given in equation 3.7 where C_{Tu} is a constant between 75 and 85.

$$Tu = 100\frac{\sqrt{2k/3}}{U} \tag{3.6}$$

$$F_{Tu} = C_{Tu}\frac{\sqrt{k}}{U_\infty} \tag{3.7}$$

This turbulent intensity issue impaired some of the prediction of transition at high angles of attack. For instance, figure 3.1 shows the transition prediction for the NACA0012 airfoil [4] for each angle of attack from 0 to 12 degrees, both with and without the modified turbulent intensity. These results include all the modifications specified in sections 3.1.1, 3.1.2 and 3.1.3. Before the modification, the predicted transition was significantly too far upstream. This adjustment improved the agreement between the model and the experiment.

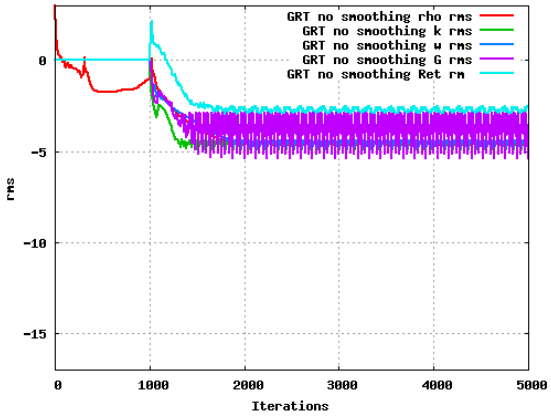

Figure 3.3 Residual convergence of the code on the NACA0012 case without smoothing the f_{onset} function ($M = 0.16$, $Re = 2.88 * 10^6$, $\alpha = 0$, $FSTI = 0.003$, $\mu_t/\mu_l = 100$)

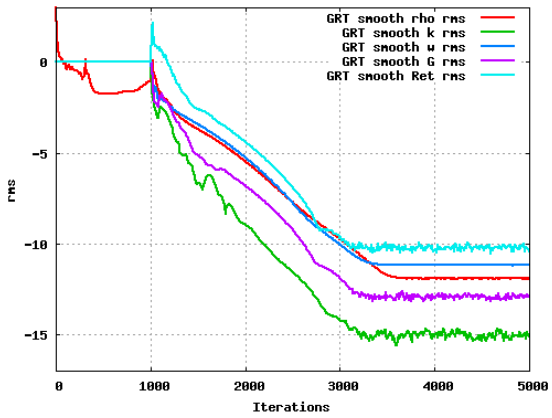

Figure 3.4 Residual convergence of the code on the NACA0012 case with smoothing the f_{onset} function

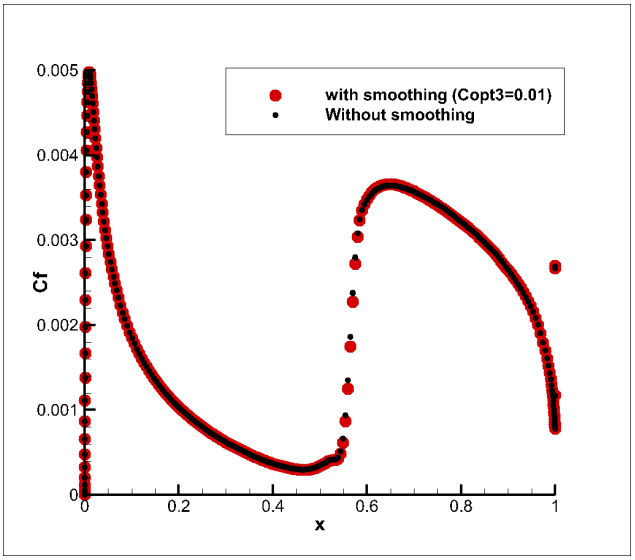

Figure 3.5 Skin friction on the NACA0012 airfoil with and without smoothing the f_{onset} function ($M = 0.16$, $Re = 2.88 * 10^6$, $\alpha = 0$, $FSTI = 0.003$, $\mu_t/\mu_l = 100$)

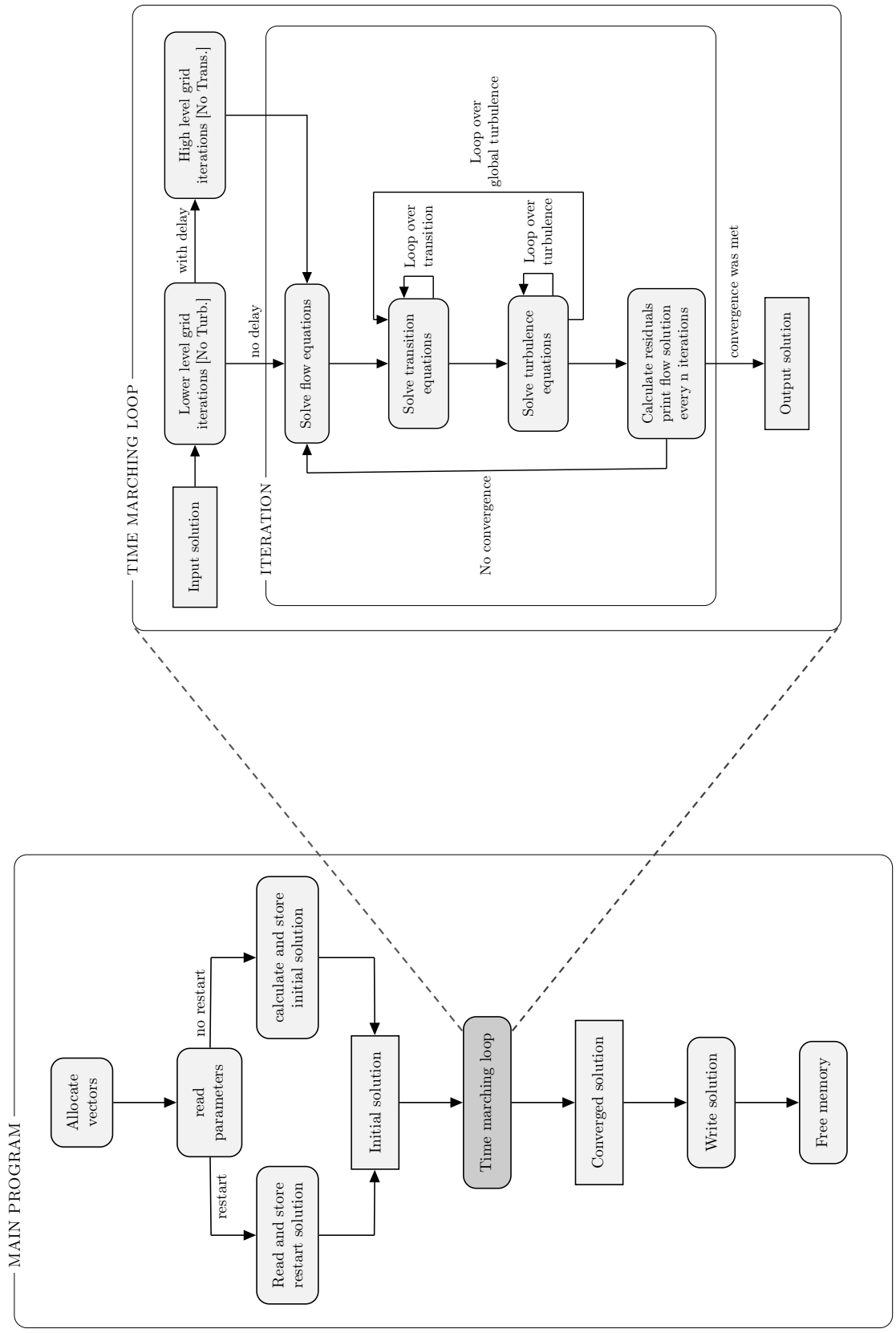

Figure 3.6 Flowchart of a segregated $k\omega\gamma Re_\theta$ transitional turbulence model for RANS code

3.2 Computational results

The present section focuses on the validation of our implementation. The list of the cases that were chosen to demonstrate its robustness is displayed in tables 3.1 and 3.2. The model is tested for natural, bypass and separation induced transition predictions. No cross-flow extension has been integrated so far, hence 3D results are only preliminary and are compared to other non-cross-flow results from the literature for validation purposes.

All the validation was performed using FANSC: a finite volume structured code with second-order implicit Euler pseudo-time marching and second-order Roe solver for the RANS equations. The method described in [24] for jacobian assembling was used to solve the γ-$Re_{\theta t}$ equations. The turbulence and transition equations are treated separately using the fully segregated approach described in [2, 82]. The meshes were generated either using Pointwise or the in-house mesh generator MBGRID. Special attention was brought to the meshing of the near-wall region. The first 2 cells from the wall have identical height and the expansion ratio is below 1.1 in the first 32 cells from the wall. Wall orthogonality was enforced with the help of mesh smoothing tools developed by Hasanzadeh et al. [84].

For 2D airfoil cases, the O-type meshes were generated with 513 nodes on the surface and 129 nodes from the surface to the far-field. This resolution was found to be a good compromise between accuracy and speed. These specifications do not apply to flat plate cases as each of them feature different length scales and have different mesh requirements. Moreover, difficulties can arise from the presence of a singularity point at the leading edge of the flat plates. As a result, the Schubauer and Klebanov case required a finer mesh than the other flat plates. The resolution of the mesh used for the Schubauer and Klebanov case is not representative of the model's requirements for cases that do not suffer the presence of a singularity point.

3.2.1 2D cases

3.2.1.1 Flat plate cases

2D Flat plate cases are often used to validate transition models. The ERCOFTAC (European Research Community on Flow, Turbulence, and Combustion) T3 series [6, 7] that includes natural transition, bypass transition and separation induced transition with some of them including non-zero pressure gradients are famous for this purpose. They were present in Langtry's original publication along with the Schubauer and Klebanoff case (SK) that addresses natural transition with a low turbulent intensity of 0.1%. Here we will focus on the Schubauer and Klebanoff case [5] for natural transition and the T3A and T3B cases that

Table 3.1 2D Cases specifics

2D cases	Mach	Reynolds	transition	FSTI(%)	$\frac{\mu_t}{\mu_l}$	α	y+
Flat plate S&K	0.2	$5 * 10^6$	natural	0.1	1.0	0	0.1
Flat plate T3A-	0.2	$3 * 10^6$	natural	0.5	8.72	0	0.05
Flat plate T3A	0.2	$1 * 10^6$	bypass	3.3	12	0	0.2
Flat plate T3B	0.2	$1 * 10^6$	bypass	6.5	100	0	0.2
NACA0012	0.16	$2.88 * 10^6$	natural	0.3	100	0 : 12	0.1
NLF0416	0.1	$2 * 10^6/4 * 10^6$	nat./separ.	0.16	10	-9 : 9	0.1
S809	0.1	$2 * 10^6$	separation	0.19	10	-10:15	0.1

Table 3.2 3D Cases specifics

3D cases	Mach	Reynolds	transition	Tu(%)	$\frac{\mu_t}{\mu_l}$	α	y+
Spheroid 6:1	0.13	$6.5 * 10^6$	natural+CF	0.15	10	5, 15	0.2
Sickle wing	0.16	$2.75 * 10^6$	natural+CF	0.17	10	-2.6	1.0
DLR-F5	0.82	$1.5 * 10^6$	shock	0.5	10	0, 2	0.2

address bypass transition with a zero pressure gradient flow. The details of the flow conditions are given in Tab. 3.1. The mesh used for the T3 series cases is composed of 448 cells along the surface and 384 cells normal to it and a total of 104,448 cells. The SK case was performed using the same mesh with 4 times as many cells in the streamwise direction. Fig. 3.8 presents the results of FANSC with the calibrated model and with the original model, along with the experimental results and the results provided by Langtry et Al. [54] for the four chosen cases. The predicted transition region appears slightly more abrupt in comparison to the experiment. This is a common issue with this model [54]. Bypass transition is accurately predicted on both the T3A and T3B cases. Of all the attempts at recalibrating the model, none seemed to perform well on the T3A- flat plate. Consequently, it was decided to recalibrate the model regardless of this case. After recalibration, the model is able to deal with the T3A- case only by using a turbulent intensity of 0.5% instead of the 0.875% prescribed in the experimental work.

3.2.1.2 NACA0012

The NACA0012 airfoil was developed in the Langley research center as part of the NACA series. It is a classical validation test case and can be found on the NASA Turbulence Modeling Resource website. In the context of transition, Gregory and O'Reilly conducted in 1973 a study on this airfoil [4]. The test case involves multiple angles of attack at a higher Reynolds number than the NLF-0416 and S809 cases. An O-type mesh is generated

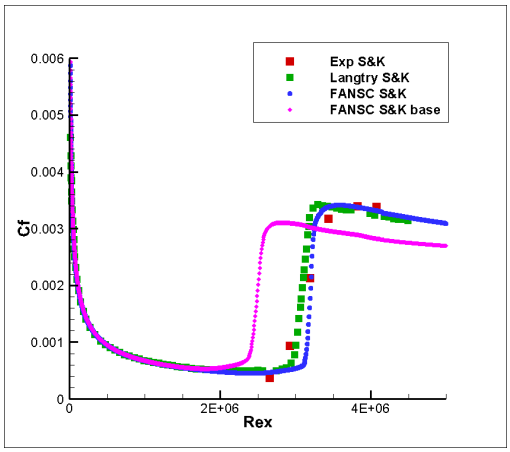

Schubauer and Klebanoff flat plate case ($M = 0.2$, $Re = 5 * 10^6$, $Tu = 0.1\%$, $\mu_t/\mu_l = 1.0$)

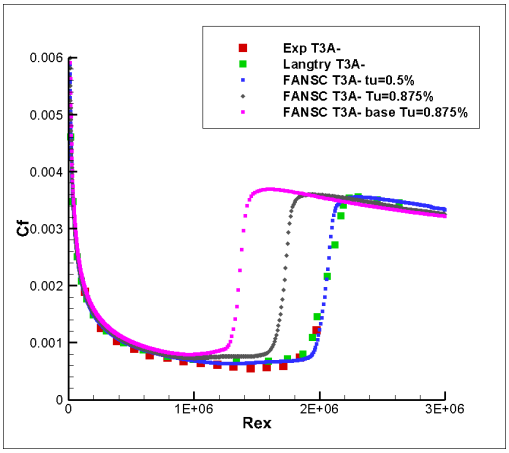

T3A- flat plate case ($M = 0.2$, $Re = 3 * 10^6$, $Tu = 0.5\%$, $\mu_t/\mu_l = 8.72$)

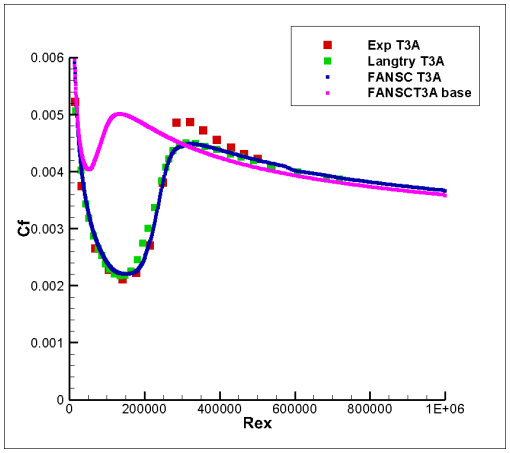

T3A flat plate case ($M = 0.2$, $Re = 1 * 10^6$, $Tu = 3.3\%$, $\mu_t/\mu_l = 12$)

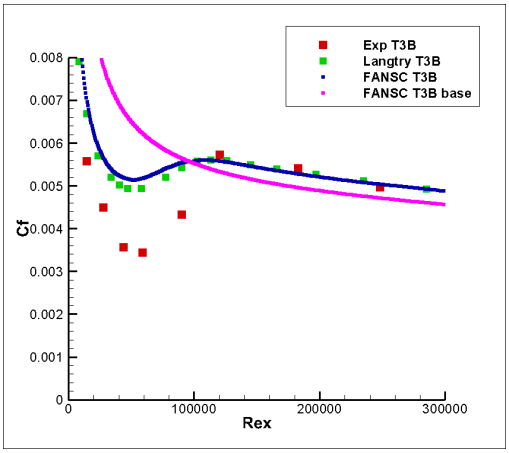

T3B flat plate case ($M = 0.2$, $Re = 1 * 10^6$, $Tu = 6.5\%$, $\mu_t/\mu_l = 100$)

Figure 3.8 friction coefficient as a function of the Reynolds number along the surface for various flat plate cases [5–7]

to simulate this case. It is composed of 512 cells along the surface and 128 cells normal to it and the domain extends to 50 chords away from the airfoil. Fig. 3.9 shows the transition position as a function of the angle of attack. The position of transition is normalized by the chord of the airfoil. Fig. 3.10 presents the lift and drag coefficients predictions along with experimental results. We compare the results of the present implementation to that of Piotrowski and Zingg [89]. The figure shows the transition location as a function of the angle of attack. At 0 degree angle of attack, transition should be identical on the upper and lower surface for this non-cambered symmetrical geometry. As the angle of attack increases, transition shifts upstream on the upper surface and downstream on the lower one. The model matches the experiment on transition location when the turbulent intensity is set to 0.3 %. The model seems to under-predict the drag coefficient C_D by 14 drag counts at a given lift coefficient C_L. A similar shift was observed by Piotrowski and Zingg [89].

3.2.1.3 S809

The S809 airfoil was designed by Somers in 1997 [8] as a turbine blade. It is designed to have separation induced transition on both sides of the airfoil between 4 and -4 degrees of angle of attack. At more extreme angles of attack, these separation bubbles disappear on the face facing the flow and transition becomes natural. An O-type mesh is generated to simulate this case. It is composed of 512 cells along the surface and 128 cells normal to it and the domain extends to 50 chords away from the airfoil. Fig. 3.11 exhibits the evolution of transition location on both sides of the airfoil when gradually changing the angle of attack. It shows a good match between the model and the experiment. The angle at which the flow separates close to the leading edge on the side opposite to the flow is about one degree off. At angles of attack higher than 13 degrees and lower than -9 degrees, transition on the side facing the flow slides too far downstream. Fig. 3.12 indicates a difference of about 5 drag counts between the simulation and the experiment. The results provided by Piotrowski and Zingg [89] showed a similar gap.

3.2.1.4 Grid convergence study

A grid convergence study was performed on the S809 case at 0 degree angle of attack. The following mesh resolutions were chosen for this task (nodes on the surface by normal nodes): 64 by 24, 128 by 48, 256 by 96, 512 by 192, 1024 by 384. The results are shown in Fig. 3.13. On the left, transition prediction is compared for each mesh resolution to the expected value where N is the total number of cells. On the right, the predicted drag coefficient is compared to the experimental value for each level of refinement.

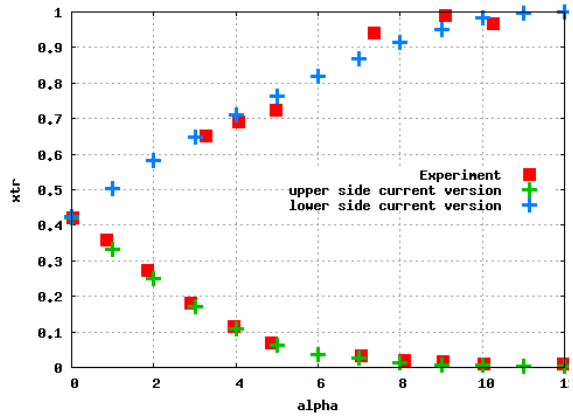

Figure 3.9 Transition position as a function of the angle of attack for the NACA0012 case [4] ($M = 0.16$, $Re = 2.88 * 10^6$, $FSTI = 0.003$, $\mu_t/\mu_l = 100$)

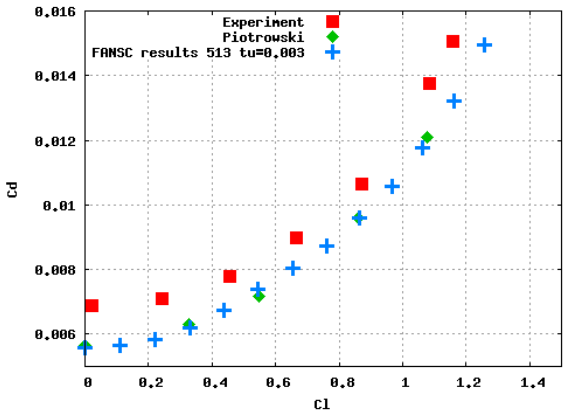

Figure 3.10 Lift coefficient as a function of the drag coefficient for the NACA0012 case [4] ($M = 0.16$, $Re = 2.88 * 10^6$, $FSTI = 0.003$, $\mu_t/\mu_l = 100$)

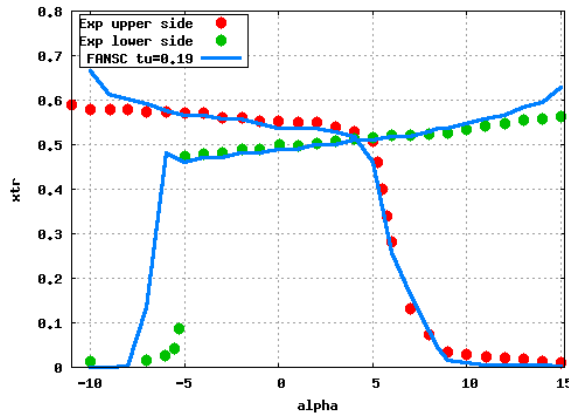

Figure 3.11 Transition position as a function of the angle of attack for the S809 case [8] ($M = 0.1$, $Re = 2 * 10^6$, $FSTI = 0.0019$, $\mu_t/\mu_l = 10$)

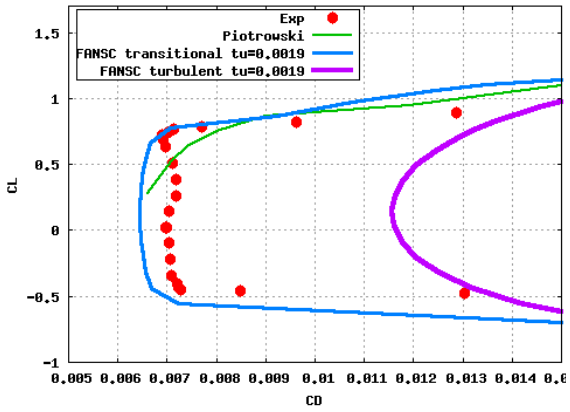

Figure 3.12 Lift coefficient as a function of the drag coefficient for the S809 case [8] ($M = 0.1$, $Re = 2 * 10^6$, $FSTI = 0.0019$, $\mu_t/\mu_l = 10$)

The results show that grid convergence is achieved. The convergence begins at a resolution of 256 by 96. To obtain reliable results while maintaining reasonable computation costs, it is recommended to use at least 256 nodes on the surface. Experience shows that 128 nodes from the surface of the object to the far-field are enough for 2D cases to allow the model to accurately predict transition location.

3.2.1.5 NLF0416

The Natural laminar flow wings are conceived to allow the laminar boundary layer to remain stable on a large portion of the surface. The NLF0416 was designed with this mindset by Somers at the Langley research center in 1981 [9]. An O-type mesh is generated to simulate this case. It is composed of 512 cells along the surface and 128 cells normal to it and the domain extends to 50 chords away from the airfoil. The source material for this case does not mention the turbulent intensity at which the measures were taken. Consequently, a value had to be chosen and $Tu = 0.16\%$ proved to give the most potent results.

Fig. 3.14 compares the transition locations found by the model on both sides of the airfoil to the experimental values for different angles of attack and a Reynolds number of 2 millions. The prediction on the lower side of the airfoil matches well with the experiment. On the upper side, however, the transition for some of the tested angles of attack was predicted as far as 5% chords away from experimental values. Fig. 3.15 shows the predicted Cl and Cd along with the experimental values for a Reynolds number of 2 millions. The model is within 10 drag counts of the experiment.

Fig. 3.16 shows the transition locations for a Reynolds number of 4 millions with varying levels of free stream turbulence intensity FSTI. Small variations of FSTI can cause substantial changes in transition location. Fig. 3.17 shows how this trend is confirmed by the predicted Cl and Cd where better results are found with higher levels of turbulence. This sensitivity for low levels of FSTI can cause uncertainties when using the model outside of canonical test cases. Finally, Fig. 3.18 and 3.19 show the convergence of FANSC on the NLF0416 case at 0 degree angle of attack and $4M$ Re.

3.2.2 3D cases

Since our model does not contain cross-flow terms, it is inaccurate when validating against experimental data. However, its numerical behavior on 3D cases is of interest as further extensions would only deteriorate, or at best maintain, these properties. This section is thus centered on verification. Additionally, since other authors historically have indeed performed

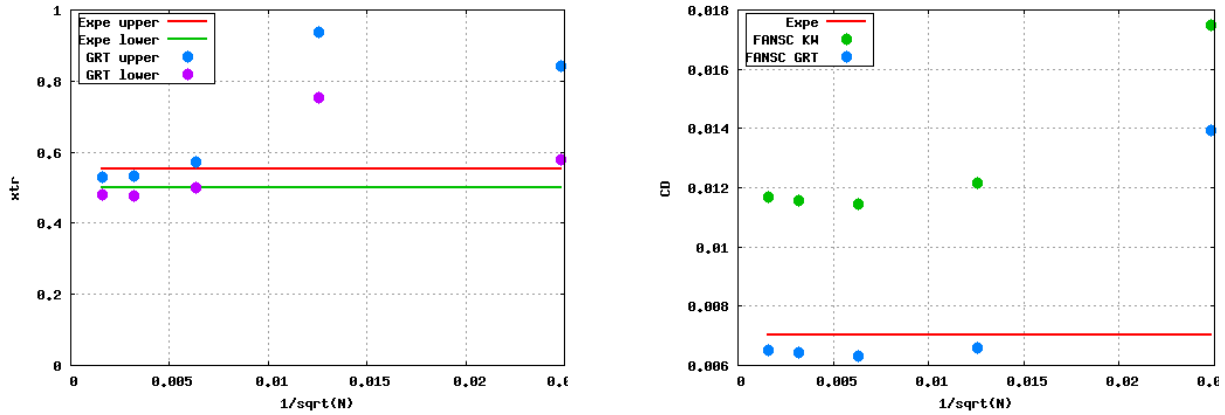

Figure 3.13 Grid convergence study of the S809 case [8]. Transition position against mesh resolution on the left and drag coefficient against mesh resolution on the right. ($M = 0.1$, $Re = 2 * 10^6$, $FSTI = 0.0019$, $\mu_t/\mu_l = 10$, $\alpha = 0°$)

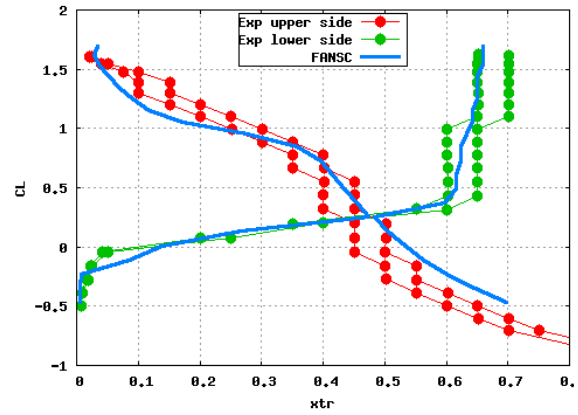

Figure 3.14 Transition position as a function of the angle of attack for the NLF0416 case [9] ($M = 0.1$, $Re = 2 * 10^6$, $FSTI = 0.0016$, $\mu_t/\mu_l = 10$)

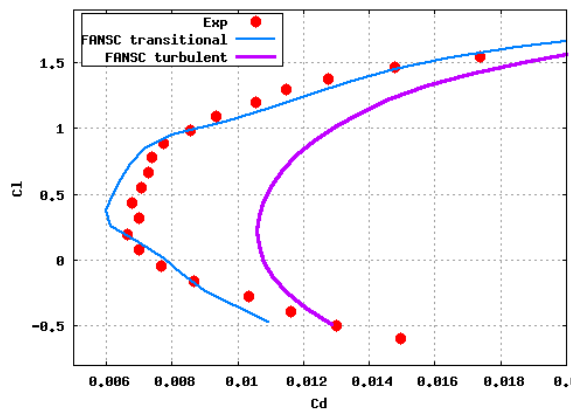

Figure 3.15 Lift coefficient as a function of the drag coefficient for the NLF0416 case [9] ($M = 0.1$, $Re = 2 * 10^6$, $FSTI = 0.0016$, $\mu_t/\mu_l = 10$)

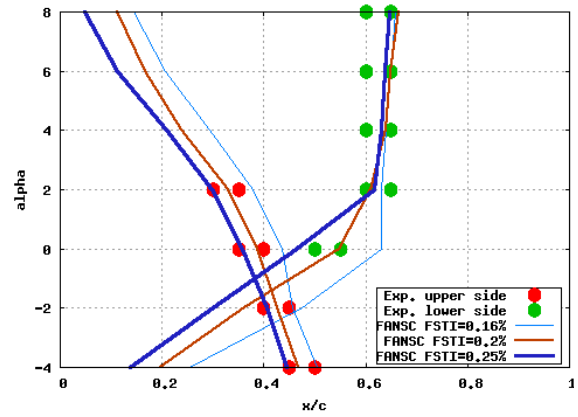

Figure 3.16 Transition position as a function of the angle of attack for the NLF0416 case with several levels of FSTI [9] ($M = 0.1$, $Re = 4 * 10^6$, $FSTI = 0.0016 : 0.0025$, $\mu_t/\mu_l = 10$)

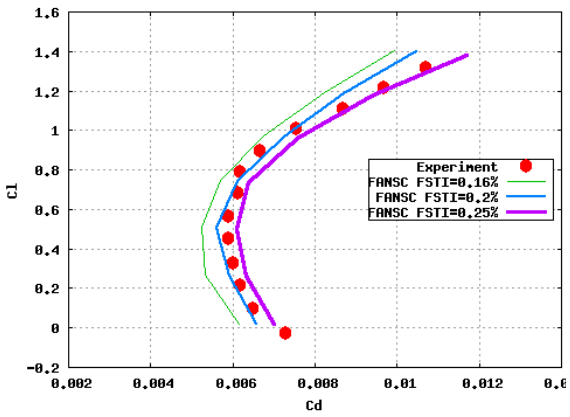

Figure 3.17 Lift coefficient as a function of the drag coefficient for the NLF0416 case with several levels of FSTI [9] ($M = 0.1$, $Re = 4 * 10^6$, $FSTI = 0.0016 : 0.0025$, $\mu_t/\mu_l = 10$)

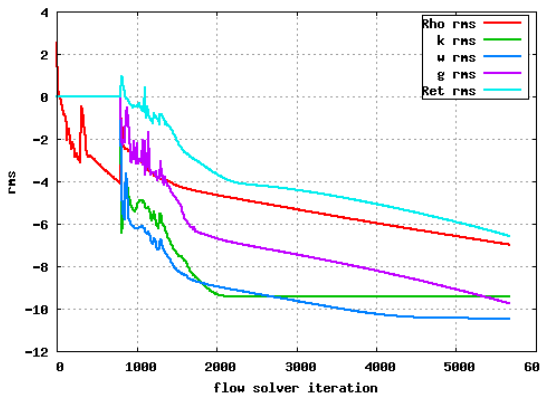

Figure 3.18 Residual convergence of FANSC on the NLF0416 case

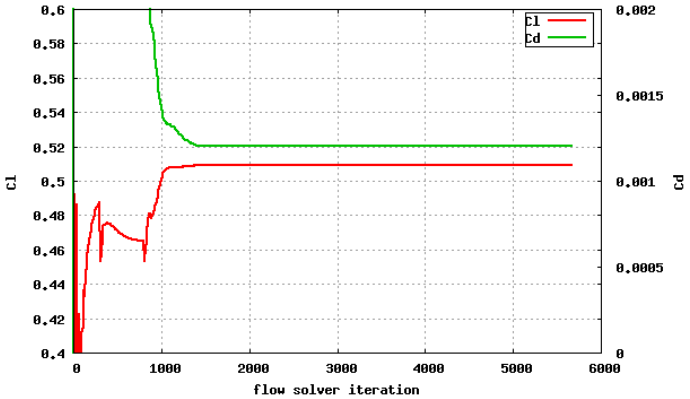

Figure 3.19 forces convergence of FANSC on the NLF0416 case

equivalent numerical tests, the section brings out interesting code-to-code comparisons despite lacking the crossflow terms.

3.2.2.1 Prolate spheroid

The prolate spheroid with a 6:1 aspect ratio was the subject of experimental studies for transition at the DLR Göttingen [10]. The geometry was studied under various flow conditions and angles of attack. This case is often used for the validation of crossflow transition models. With a turbulent intensity of about 0.2% and a Reynolds number of $6.5 * 10^6$, transition on the surface of the spheroid is caused by Tollmien–Schlichting waves, crossflow instabilities or a mix of both. Because of the dominance of crossflow transition, the present implementation cannot accurately model this case. Still, results were generated to establish the capabilities of the model and verify its 3D modeling behavior by comparing this work to similar studies from the literature [11, 41, 70, 71, 86, 90].

The symmetric properties of the geometry allow us to halve the model. The resulting structured mesh used for this study comprises 69000 cells on the surface, 512 along the chord and 128 along the span, and 8.9M cells in the volume. The details of the flow conditions are given in Tab. 3.2.

Fig. 3.20 compares the predicted skin friction coefficient of the spheroid from the present study with those of the work of Grabe, Shengyang, and Krumbein in 2016 [11]. As expected, the model implemented in FANSC does not match the experiments but exhibits similar behaviors as other non-crossflow transition models.

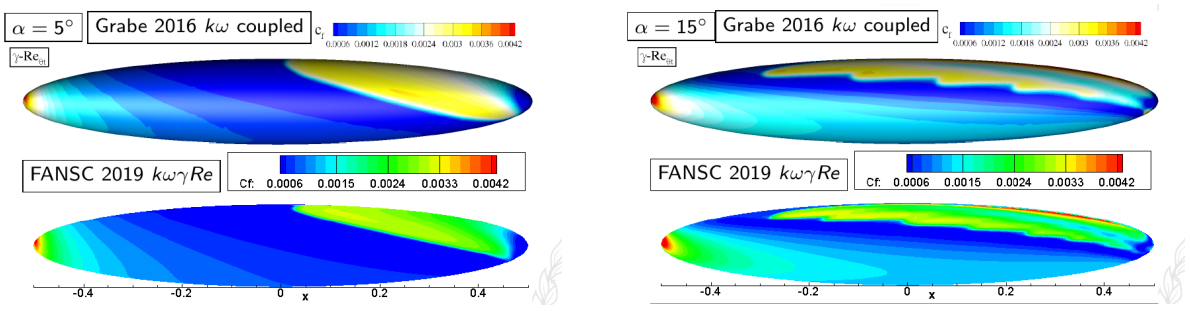

Figure 3.20 Skin friction coefficient of the prolate Spheroid 6:1 [10] at $\alpha = 5°$ (left) and $\alpha = 15°$ (right) modeled with the γRe_θ model without crossflow extension and compared with results from [11]. ($M = 0.13$, $Re = 6.5 * 10^6$, $FSTI = 0.0015$, $\mu_t/\mu_l = 10$)

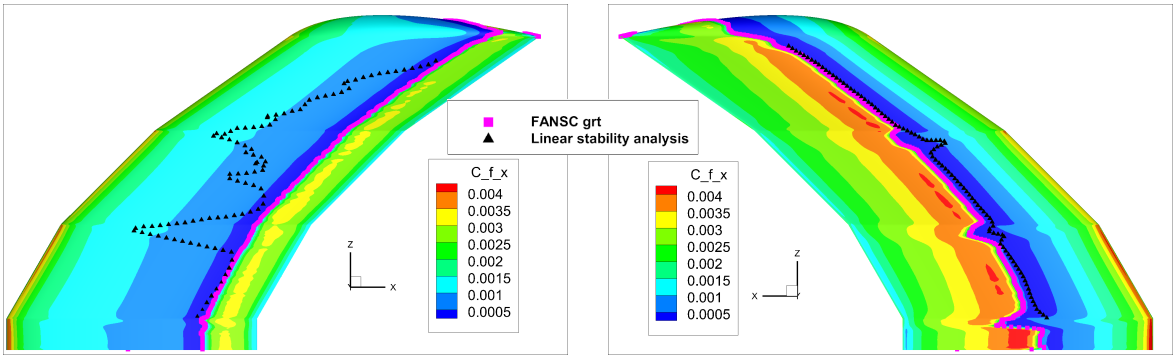

Figure 3.21 Friction coefficient on the lower side (right) and the upper side(left) of the Sickle wing [12,13] with transition line in pink and linear stability analysis in black [14]. ($M = 0.16$, $Re = 2.75 * 10^6$, $FSTI = 0.0017$, $\mu_t/\mu_l = 10$, $\alpha = -2.6°$)

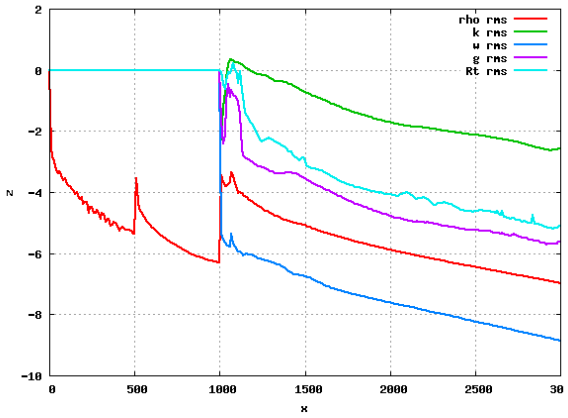

Figure 3.22 Residual convergence of FANSC on the Sickle shaped wing

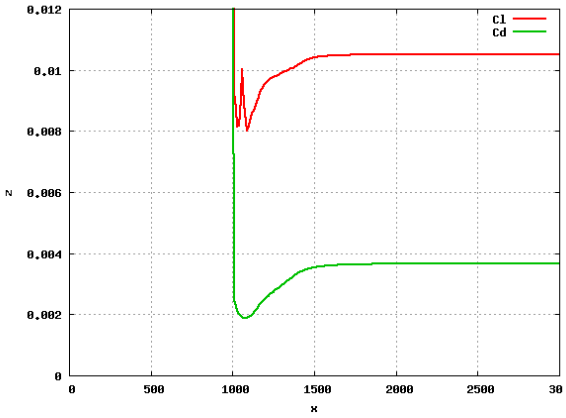

Figure 3.23 forces convergence of FANSC on the Sickle shaped wing

3.2.2.2 Sickle wing

The Sickle-shaped wing was developed in 2013 by Petzold and Radespiel [12, 13] for the specific purpose of validating transition prediction methods. The idea behind the design is to test several levels of crossflow amplification with one configuration. As a result, the wing comprises 3 sections of increasing sweep angle. The sweep angle starts at 0 degrees at the root, and then changes to 30, 45 and finally reaches 55 degrees as we progress along the span towards the tip. The upper surface of the wing is designed to amplify crossflow vortices and damp Tollmien-Schlichting waves while the lower surface amplifies both.

The geometry and the details of the case were graciously provided by the DLR. From the geometry, a structured mesh was generated with 34.7 million cells. Fig. 3.21 exhibit the predicted transition line on both sides of the wing compared with the results of a linear stability analysis from the work of Petzold and Radespiel [14]. In their article, they show that this linear stability analysis matches well with the experiment. On the figure, the black triangles represent the stability analysis and the pink squares represent the prediction by the γ-$Re_{\theta t}$ model.

The γ-$Re_{\theta t}$ model is close to the expected line on the lower side where natural transition plays an important part but is not in agreement at the kinks where the angle changes. On the upper side, close to the root, the same observation can be made. Indeed, in the section of the wing where the sweep angle is 30 degrees, natural transition predominates and the model is accurate. Further down the span, however, the predicted transition line is far downstream from the linear stability analysis result. This gap testifies to the importance of a crossflow extension for 3D transition modeling. These results are aligned with the findings of other authors who tested the model without crossflow on this case [11, 41, 91].

Finally, Fig. 3.22 and 3.23 show the convergence of FANSC on the sickle shaped wing case. After 2000 iterations, residual convergence has reached 10^{-7}.

3.2.2.3 DLR-F5

The DLR-F5 model is a swept wing with symmetrical sections that was designed in 1998 by Helmut Sobieczky at DLR Göttingen [15, 92]. It is a well-documented case for 3D transition modelling validation [54, 57]. This wing is selected for the present work to test the model's capabilities under transonic flows. Also, this case features natural and crossflow transition and two angles of attack. The details of the flow conditions are listed in table 3.2. The structured mesh used for this simulation comprises 56500 cells on the surface and 13 million cells in the volume.

Figures 3.24 and 3.25 show the predictions made by this implementation of the model with 0 and 2 degrees angle of attack and compares them to schematics from the experimental work [15]. The figure on the left originates from the test case report made public by the DLR [15], the one in the middle shows the result of the present study by outlining the turbulent region in red and the laminar region in blue. The figure on the right presents the contours of the friction coefficient with the stream-lines along the surface of the wing.

Due to strong crossflow effects, the transition prediction from the model does not closely match the experimental measures close to the root of the wing. Further down the span, a shock wave forms that induces separation of the flow which in turn triggers the transition. The present implementation successfully predicts this behavior on both angles of attack. The discrepancies of these results are related to the inability of the model to capture crossflow transition. The integration of this feature should improve the fidelity of the model for this case.

Previous research efforts have shown similar results and issues with the DLR-F5 wing when modeling it without crossflow [54, 57].

3.2.3 Convergences

It is worth mentioning that a common use for such transition prediction methods in the aerospace industry is to be implemented as part of an aerodynamic shape optimization process. This process can require to use of the transition model repeatedly for changing geometries and conditions. A good model not only needs to be accurate and robust but also fast to be relevant to this kind of usage. In this context, timely convergence is critical. This model is particularly sensitive to this issue as, by adding 2 equations to the RANS and $k\omega$-SST system, it is prone to convergence problems.

To address this issue, the present study uses the method of segregation of the turbulence and transition models from the flow equations introduced in the research of Mosahebi and Laurendeau [2, 82]. Also, it was found that this implementation suffered from using a low pseudo-time step when solving the equation for Re_θ. Low values of pseudo-time step are chosen to increase stability, however, it was found that in this case, convergence slowed down considerably. By choosing a high value for this pseudo time step, convergence speed was greatly improved with no negative influence on stability.

Figure 3.26 exhibits the RMS convergence rate of the transition model compared to that of the full turbulent $k\omega$-SST model on the NACA0012 case. It appears that the transition model requires about 2 times the number of iterations the turbulence model does to reach

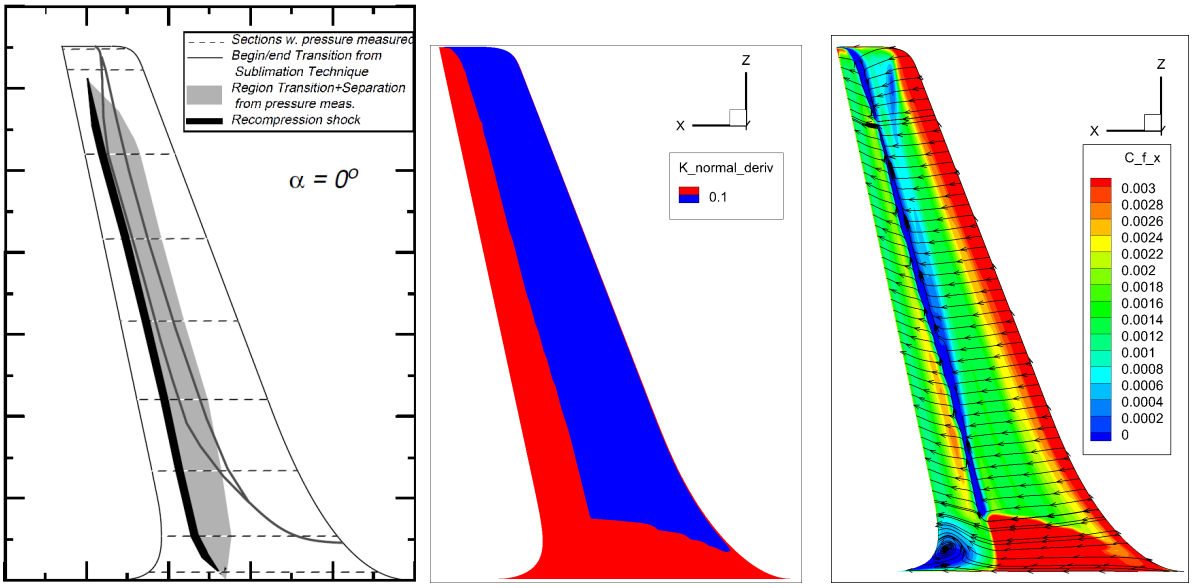

Figure 3.24 Results for the DLR-F5 case with 0 degrees angle of attack: experimental results schematics [15] [15] (left), simulated transition line (center) and friction coefficient with streamlines (right). ($M = 0.82$, $Re = 1.5 * 10^6$, $FSTI = 0.005$, $\mu_t/\mu_l = 10$, $\alpha = 0°$)

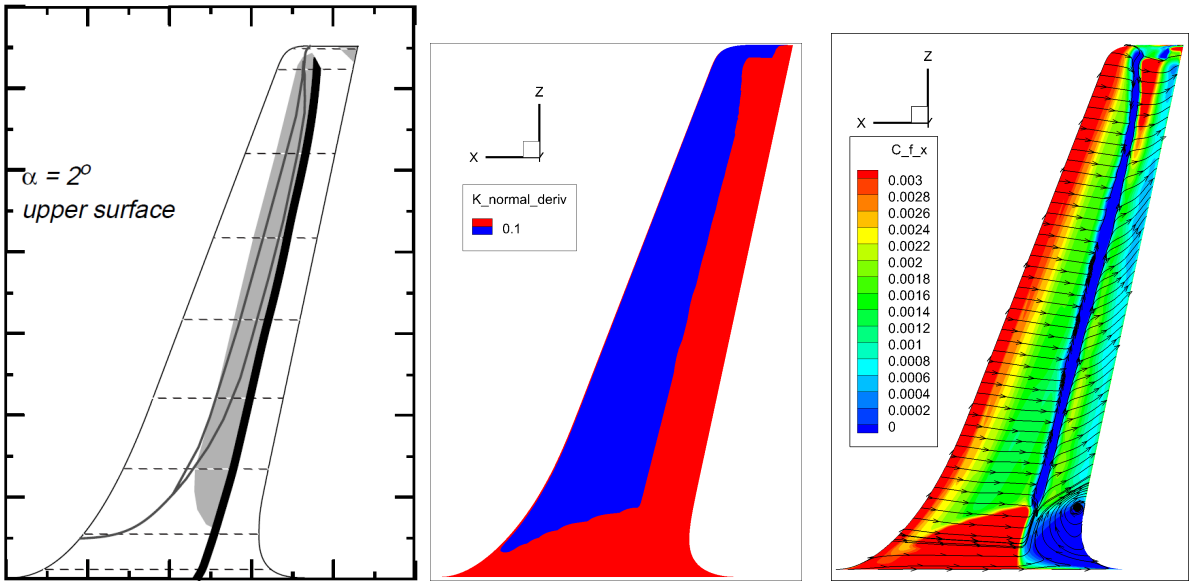

Figure 3.25 Results for the DLR-F5 case with 2 degrees angle of attack: experimental results schematics [15] (left), simulated transition line (center) and friction coefficient with streamlines (right). ($M = 0.82$, $Re = 1.5 * 10^6$, $FSTI = 0.005$, $\mu_t/\mu_l = 10$, $\alpha = 2°$)

convergence.

Figure 3.27 shows the residual and drag convergence behavior of the model on the Sickle wing case. The model is slower to converge than on smaller 2D meshes but does achieve convergence.

3.3 Conclusion

The γ-$Re_{\theta t}$ transition model is implemented in a structured finite volume RANS code and modifications are made to improve the robustness and accuracy of the implementation. An optimization algorithm was developed to help in this process, for which the Nelder-Mead method was chosen as a basis. Results were obtained for a range of 2D test cases that cover natural, bypass and separation induced transition on both flat plates and airfoils under various flow conditions. The 2D results show good agreement with experimental measurements as well as with other numerical studies. Several 3D cases from the literature were studied, such as the Prolate spheroid, as well as the Sickle wing. Predictions on the 3D cases show discrepancy with experimental results where crossflow effects dominate the boundary layer, as the model in its current implementation has no means of taking this type of transition into account. However, if natural or separation induced transition takes over, the model shows an appropriate agreement with experimental observations. Efforts were made to optimize the model's convergence properties. Special attention is paid to non-differentiable functions, pseudo-time stepping and segregation of the equations.

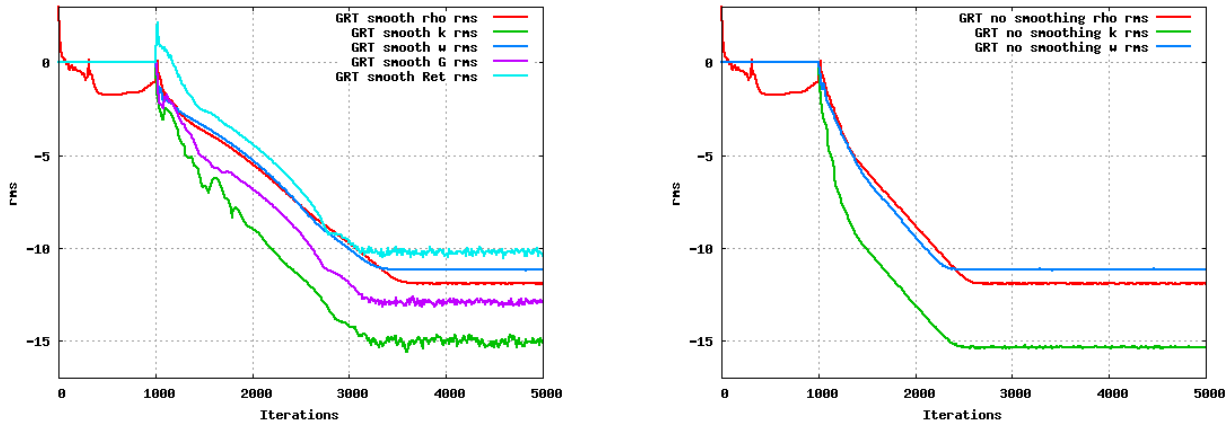

Figure 3.26 Convergence behavior of the γ-$Re_{\theta t}$ model on the 0 degree angle of attack NACA0012 case [4] with 65000 cells. Residual convergence of the $k\omega$-γ-$Re_{\theta t}$ model on the left and convergence of the $k\omega$-SST model alone on the right. ($M = 0.16$, $Re = 2.88 * 10^6$, $FSTI = 0.003$, $\mu_t/\mu_l = 100$, $\alpha = 0°$)

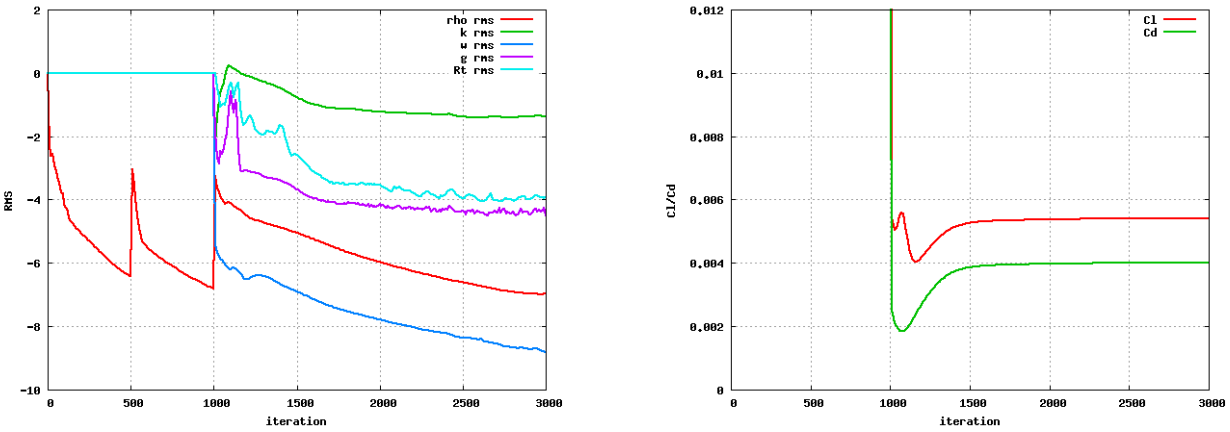

Figure 3.27 Convergence behavior of the $\gamma Re_{\theta t}$ model on the Sickle wing case [12, 13] with 34 million cells. Residual convergence on the left and drag convergence on the right.

CHAPTER 4 Calibration of Crossflow Extension

In this chapter, the transition model described in chapter 3 is extended to include crossflow effects in the prediction of transition. The implemented crossflow extension is heavily inspired from the model created by Müller and Herbst [58]. It is recalibrated using the method described in 2.4 and validated on a series of 3D cases where the influence of crossflow on transition is significant.

4.1 Crossflow Extension

3 different cross-flow extensions were implemented as they are described in their respective publication:

- The helicity based extension published by Grabe et Al. in 2016 [11]
- The helicity extension published by Langtry in 2015 [41]
- The extension published by Muller and Herbst in 2014 [58]

However, the results presented in [11], [41] and [58] could not be reproduced with the recommended formulations. This issue could be caused by the modifications brought to the original model prior to the addition of a crossflow extension. In order to match experimental results, the crossflow extension was re-calibrated. To do so, the optimization method described in section 2.4 was used to tune the constants.

The first attempt at optimizing these extensions only included the NLF-0415 infinite swept wing case with 6 flow conditions [93]. This process was able to drastically improve results on all 3 extensions. In figure 4.1 the predictions made by FANSC are compared with the results of Muller and Herbst [58], Grabe and Al. [11], Jung and Al [70] and the experimental measures by Dagenhart and Saric [93]. The graph on the left shows the transition prediction made by the γRe_θ model without cross-flow extension. Despite some minor differences, the results without cross-flow seem to match what can be found in the literature. The graph on the right contains the results with cross-flow extensions. The new optimized calibration shows promise as it predicts transition location very close to the experimental value. Figure 4.2 is the same graph but featuring the extension from Langtry instead. Again, the optimized extension performs well. the optimization was performed on all 3 extensions (Grabe and Al. [11], Muller and Al. [58] and Langrty [41]) and was able to improve results for each. On

this case alone, the 3 optimized extensions seem on par with each other in terms of accuracy. However these recalibrations did not perform well on other 3D test cases. Consequently, the optimization was remade using both the NLF(2)-0415 and the Prolate Spheroid cases. These cases are described and studied in sections 4.2.1 and 4.2.2. Out of the 3 models, the extension from Muller and Herbst was the most successful.

This extension adds a destruction term D_{CF} to the right hand side of the Re_θ equation as shown in Eq.4.2. D_{CF} reads Eq.4.1 where c_i are calibrated constants. This destruction term uses helicity through a non-dimensional number Re_H as in Eq.4.3. Moreover, the helicity Reynolds number Re_H was modified to $Re_{H|New}$ as in Eq.4.4, following the example of Grabe et al [11] to avoid over-reliance on the momentum thickness θ. Section 4.2 addresses the results of this recalibrated crossflow extension on several 3D test cases.

$$D_{CF} = \min\left(\max\left[0, \left(\frac{\rho}{1000.t}\left(\frac{Re_H}{6}\right)^{c_1}(Re_\Omega)^{c_2}\left(\frac{12\theta}{d}\right)^{c_3} - c_4\right)c_5\right], c_6\right) \tag{4.1}$$

$$\frac{\partial \rho \tilde{Re}_{\theta t}}{\partial t} + \frac{\partial\left(\rho u_i \tilde{Re}_{\theta t}\right)}{\partial x_i} - \frac{\partial}{\partial x_j}\left[\sigma_{\theta t}\left(\mu_l + \mu_t\right)\frac{\partial \tilde{Re}_{\theta t}}{\partial x_j}\right] = P_3 - D_{CF} \tag{4.2}$$

$$Re_H = \frac{\theta}{\nu}\sqrt{\theta H} \tag{4.3}$$

$$Re_{H|\text{New}} = \frac{Hd^2}{U\nu} \tag{4.4}$$

4.2 Computational Results

The present section focuses on the validation of this implementation of the model on 3D cases with crossflow (CF) effects. The model was validated on 2D cases in [79] and tested for natural, bypass and separation induced transition predictions. The list of cases that were chosen to demonstrate the robustness of the code is displayed in Table 4.1.

4.2.1 NLF(2)-0415

The NLF(2)-0415 is a natural laminar flow airfoil designed by Somers at the Langley research center in 1999 [93] to study crossflow instabilities. It is treated as an infinite swept wing with 45 degrees sweep angle and -4 degrees angle of attack.

An O-type mesh is generated to simulate this case. It is composed of 384 cells along the

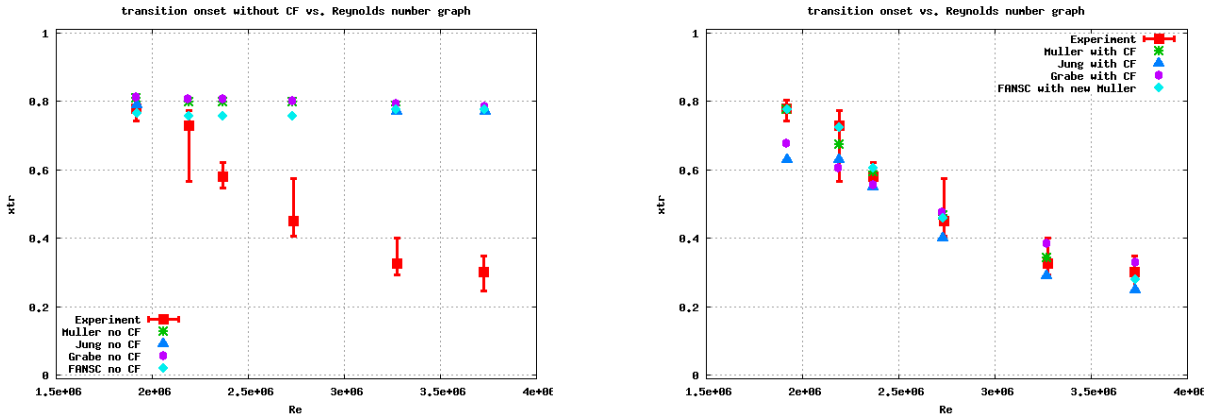

Figure 4.1 Comparison of convergence performance of the γRe_θ model with (right) and without smoothing (left) on the f_{onset} fucntion, on the NACA0012 case [4] using a 65000 cells mesh. ($M = 0.16$, $Re = 2.88 * 10^6$, $FSTI = 0.003$, $\mu_t/\mu_l = 100$, $\alpha = 0°$)

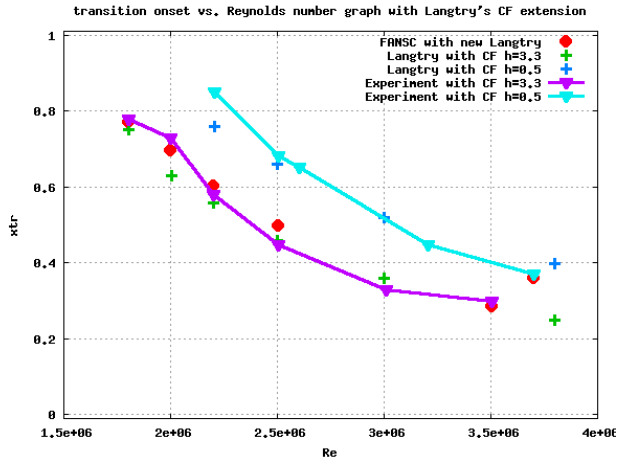

Figure 4.2 Comparison of convergence performance of the γRe_θ model with (right) and without smoothing (left) on the f_{onset} fucntion, on the NACA0012 case [4] using a 65000 cells mesh. ($M = 0.16$, $Re = 2.88 * 10^6$, $FSTI = 0.003$, $\mu_t/\mu_l = 100$, $\alpha = 0°$)

Table 4.1 3D Cases specifics

3D cases	Mach	Reynolds	transition	Tu(%)	$\frac{\mu_t}{\mu_l}$	α
NLF(2)-0415	0.12 : 0.23	$1.8 : 3.5 * 10^6$	natural+CF	0.1	10	-4
Spheroid 6:1	0.13	$6.5 * 10^6$	natural+CF	0.1	10	5, 15
DLR-F5	0.82	$1.5 * 10^6$	shock	0.5	10	0, 2
Sickle wing	0.16	$2.75 * 10^6$	natural+CF	0.17	10	-2.6

surface and 128 cells normal to it for a total of 49152 cells and the domain extends to 50 chords away from the airfoil. The y+ along the surface does not exceed 0.25 for any of the studied flow conditions. The mesh does not take wind tunnel walls into account. this study uses a free stream turbulent intensity of FSTI = 0.1% and turbulent viscosity $\mu = 10$ with varying Reynolds and Mach numbers as specified in table 4.2.

This case is used as a reference for the calibration of the crossflow extension as described in 4.1. Fig. 4.3 shows the results of the model compared with the experimental data. For all flow conditions, the model closely matches the experiment.

4.2.2 Prolate Spheroid

The prolate spheroid 6:1 is a test case from the low-speed wind tunnel of DLR Göttingen [10] that is designed to study crossflow effects. It is a classic case for the validation of crossflow transition models and was used during the 2021 AIAA transition modeling workshop. In this work, we focus on experimental results using a turbulent intensity of about 0.2% and a Reynolds number of $6.5 * 10^6$ for which transition on the surface of the spheroid is caused by Tollmien–Schlichting waves, crossflow instabilities or a mix of both.

A structured mesh was generated for this study. It is composed of 69000 cells on the surface with 512 along the chord and 128 along the span, and 8.9M cells in the volume. This study uses a FSTI of 0.1% and Turbulent viscosity of 10.0 with a Reynolds number of $6.5 * 10^6$ and Mach number of 0.13.

Fig. 4.4 and 4.5 compare the predicted skin friction coefficient of the spheroid from the present study with 5 and 15 degrees angle of attack against experimental results. With 5 degrees angle of attack, the predicted transition line is too far downstream compared to the experiment above 160 degrees and below 20 degrees. In these areas, there should be very little helicity and the crossflow extension should not trigger transition. The crossflow extension here fails to capture the physics that trigger transition early. The same issue appears with 15 degrees angle of attack. The model finds the correct transition position between 170 and 130 degrees. From 130 degrees to 30 degrees, the model predicts transition downstream from the experimental data by about 10 percent cords. This suggests the crossflow correlation is incorrect in these conditions. To improve these results, either the calibration should be

Table 4.2 NLF(2)-0415 case flow conditions

Mach	0.123	0.140	0.151	0.174	0.209	0.239
Reynolds	1.92×10^6	2.19×10^6	2.37×10^6	2.73×10^6	3.27×10^6	3.73×10^6

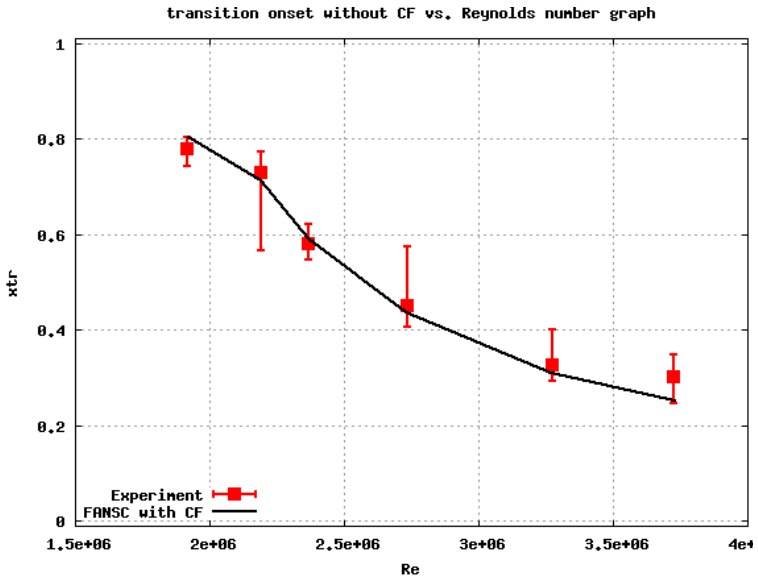

Figure 4.3 transition location compared to Reynolds number for the NLF(2)-0415 infinite swept wing case ($Tu = 0.1\%$, $\alpha = -4$)

refined or the structure of the crossflow source term should be modified.

Fig. 4.6 and 4.7 show the results of the FSTI sensitivity study conducted on the Prolate Spheroid. It takes a significantly higher turbulent intensity to resolve the aforementioned issue and this does not seem to be a viable solution. Fig. 4.8 and 4.9 show the results of a similar FSTI sensitivity study conducted without the CF extension. These results show that in areas where helicity is low, transition is predicted in roughly the same area with and without CF extension. For instance, at 5 degrees angle of attack, transition is the same at 0 degrees and 180 degrees with or without transition. At 15 degrees angle of attack, the same can be observed at 0 degree. This confirms the idea that the CF extension is inactive in these areas. An angle of attack sensitivity study is also conducted on the Prolate Spheroid. The results are comprised in Fig. 4.10 and 4.11. The results are rather insensitive to angle-of-attack variations.

4.2.3 DLR-F5

The DLR-F5 model is a swept wing with symmetrical sections that was designed in 1998 by Helmut Sobieczky at DLR Göttingen [15, 92]. It is a well-documented case for 3D transition modelling validation [54, 57]. This wing is selected for the present work to test the model's capabilities for transonic flows. The flow conditions for this case read $Re = 1.5 \times 10^6$, $M = 0.82$ and FSTI $= 0.5\%$. The structured mesh used for this simulation comprises 56500

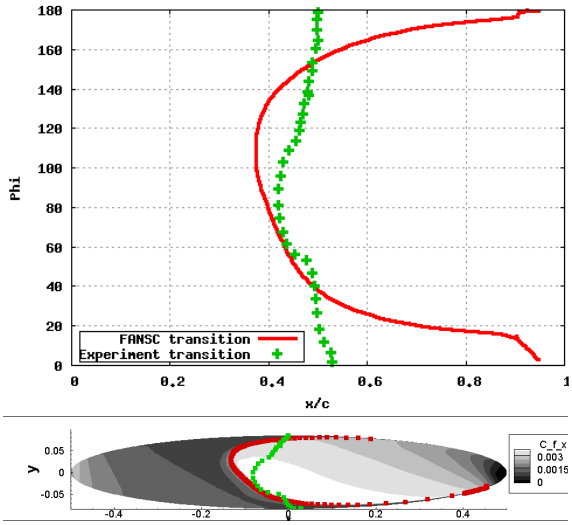

Figure 4.4 Transition prediction with crossflow extension on the Prolate Spheroid with 5 degrees of angle of attack

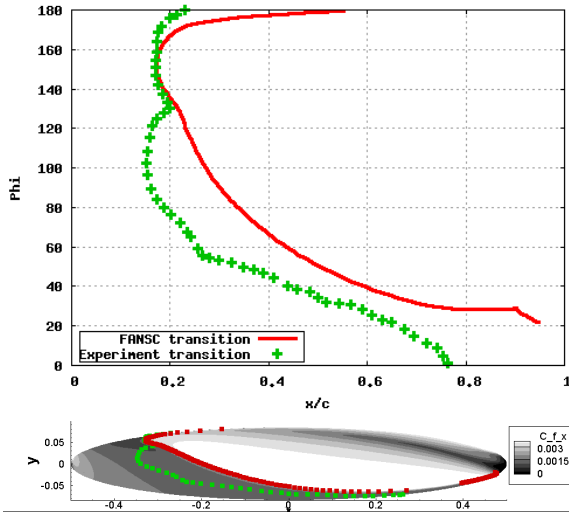

Figure 4.5 Transition prediction with crossflow extension on the Prolate Spheroid with 15 degrees of angle of attack

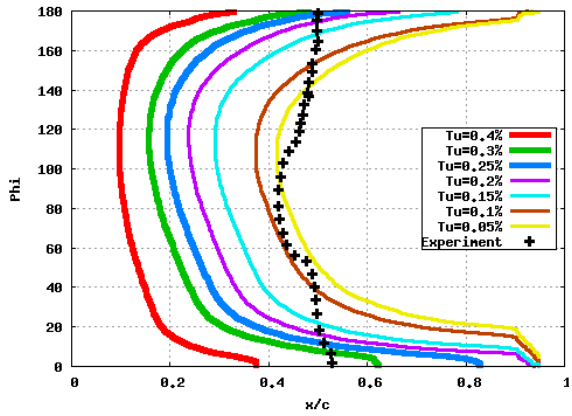

Figure 4.6 Transition prediction with crossflow extension on the Prolate Spheroid with 5 degrees of angle of attack and varying FSTI

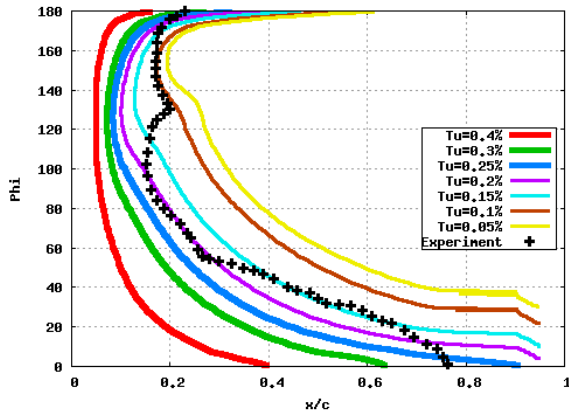

Figure 4.7 Transition prediction with crossflow extension on the Prolate Spheroid with 15 degrees of angle of attack and varying FSTI

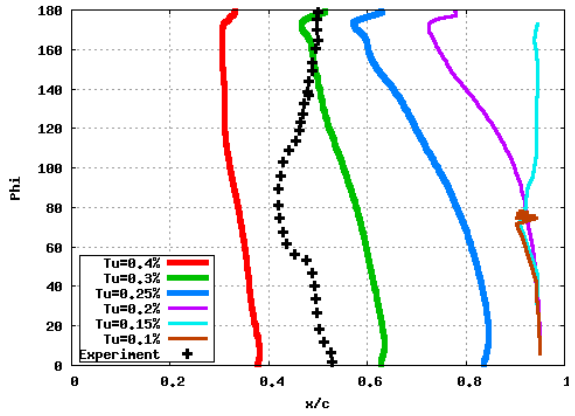

Figure 4.8 Transition prediction without crossflow extension on the Prolate Spheroid with 5 degrees of angle of attack and varying FSTI

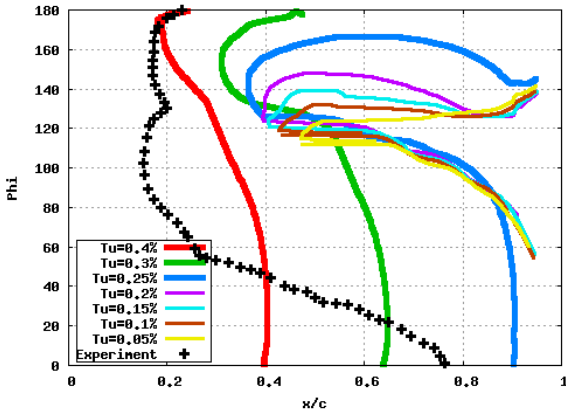

Figure 4.9 Transition prediction without crossflow extension on the Prolate Spheroid with 15 degrees of angle of attack and varying FSTI

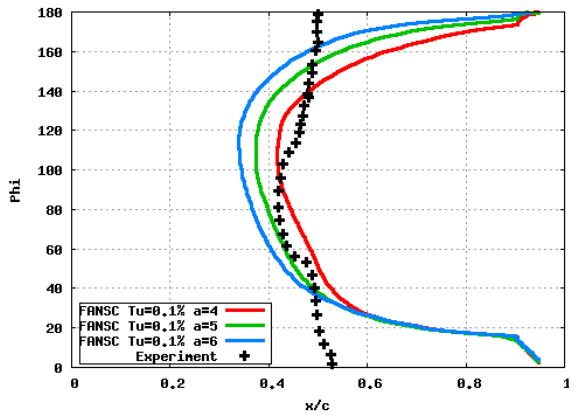

Figure 4.10 Transition prediction with crossflow extension on the Prolate Spheroid with 5 degrees of angle of attack and varying AoA

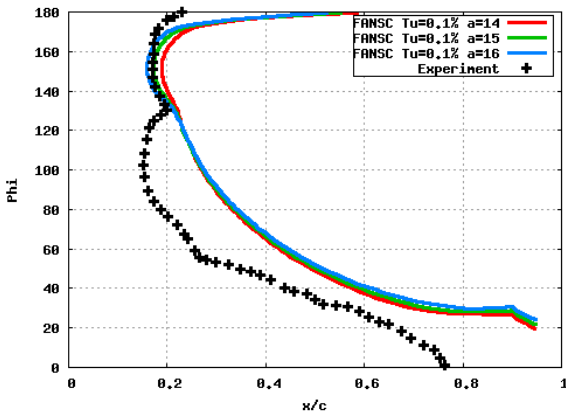

Figure 4.11 Transition prediction with crossflow extension on the Prolate Spheroid with 15 degrees of angle of attack and varying AoA

cells on the surface and 13 million cells in the volume.

Fig. 4.12 shows the predictions made by this implementation of the model with and without crossflow with 2 degrees angle of attack. The computed transition line is compared to the experimental result. This experimental data originates from the test case report made public by the DLR [15]. By comparing the crossflow transition region with and without crossflow, it is clear that the extension drastically improves the results. Fig. 4.13 displays the transition lines on top of the pressure coefficient contour plot along the surface. One can observe that when crossflow does not trigger transition, transition is triggered by the presence of the shock.

4.2.4 Sickle-shaped Wing

The Sickle-shaped wing was developed in 2013 by Petzold and Radespiel [12, 13] to study crossflow effects with spanwise variation of the flow. The geometry and instructions to model this case were graciously provided by the DLR. It features 3 connected sections with each their own sweep angle. The sweep angle starts at 0 degrees at the root, and then increases to 30, 45 and finally reaches 55 degrees as we progress along the span towards the tip. The upper surface of the wing is made to amplify crossflow vortices and damp Tollmien-Schlichting waves.The lower surface is designed to amplifies both. The flow conditions for this case are $M = 0.16$, $Re = 2.75 * 10^6$, FSTI $= 0.0017$, and $\alpha = -2.6°$.

A structured H-mesh was generated for this case. It contains 34.7 million cells in the volume, 320,000 cells on the surface and maintains a $y+$ below 1.0 along the surface. A grid sensitivity study was conducted on this case in [81].

Fig. 4.14 compares the predicted transition line with and without crossflow extension with the experimental results of Petzold and al. [14]. The extension clearly improved the prediction on the last two sections, but makes the model over predict the influence of crossflow on the first section. After examining the field values, it was discovered that the levels of helicity in the boundary layer follow the same pattern as the transition line in the figure. This suggests that the extension relies probably too much on helicity and should take some other parameter into account in order to limit the model in some areas where helicity alone would suggest that transition should take place. However, this hypothesis contradicts our previous results on the Prolate spheroid where the opposite problem was observed. This type of paradox makes the formulation and calibration of such models particularly hard. Indeed, the model is expected to match a wide variety of cases, yet the phenomena at play are not fully understood and experimental results rarely span several flow conditions or angles of attack.

Fig. 4.15 show the results of a FSTI study on the sickle-shaped. The study shows that the

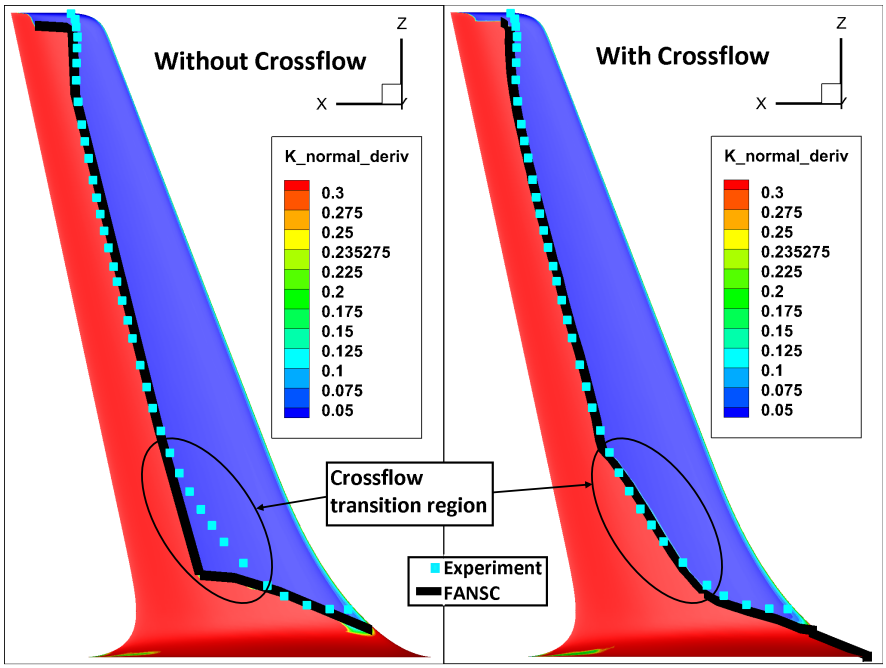

Figure 4.12 Transition prediction with and without crossflow on the DLR F5 wing

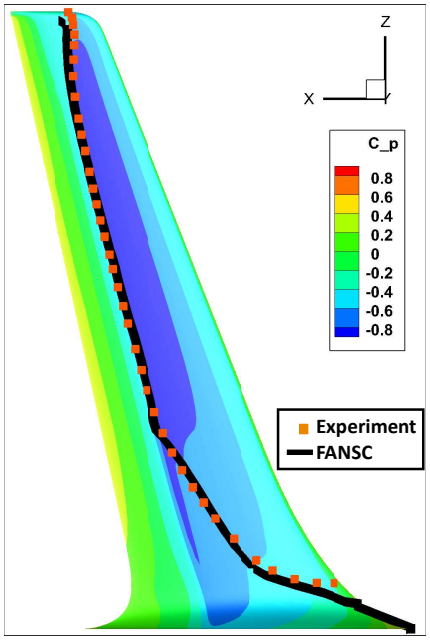

Figure 4.13 DLR F5 wing transition line with pressure coefficient

excess of crossflow instability on the first section is not an artefact of the external turbulence.

4.2.5 CRM-NLF

The final test case in this validation campaign is the CRM-NLF full aircraft case, as was used during the first AIAA transition modeling workshop in January 2021. The geometry is composed of a fuselage and a wing with 37.3 degrees of leading edge sweep angle. The flow conditions for this case are $M = 0.85$, $Re = 15 * 10^6$, FSTI $= 0.24\%$, $\frac{\mu_t}{\mu_l} = 10$ and $\alpha = 1.98$. The mesh used to model this case consists of 24 Million cells with a maximum $y+$ of 0.2. Fig. 4.16 shows a side view of the coarse mesh while Fig. 4.17 displays the surface mesh on the top side of the wing.

The model predicts lift and drag accurately as shown in fig. 4.18 where the computed results and the experimental data overlap.

Fig. 4.19-4.22 show the transition prediction of FANSC for several angles of attack along with the levels of friction coefficient on the surface of the wing. It is clear that the model overestimates the influence of crossflow effects on transition onset. Similarly to our results on the Sickle wing, the over-dependence on helicity seems to cause the model to overshoot the instability of the boundary layer.

Finally, experimental results are available for pressure coefficients on rows along the span. The placement of these rows is described in Fig. 4.23 and 4.24. From rows A to G, the computation accurately predicts the experimental transonic shock while for the rows H and I, the shock modeled is about 0.1 chords away from the experiment.

4.3 Analysis

The individual validation results show a net improvement of the transition prediction with the introduction of the crossflow extension. This section investigates potential improvements by further examining results for the Sickle Shaped Wing and the Prolate Spheroid.

The former seems to be an over prediction of the crossflow effects. A study was conducted in which the crossflow destruction term was cancelled from the root of the sickle shaped wing up to $z = 14$ which is close to the end of the first section. The result in Fig. 4.32 presents a much improved transition line. This suggests that crossflow should have little to no influence on this part of the wing. This modification is not a viable option for a general method but its results gives an indication of how to adjust the correlation to better fit this case.

With this in mind, a variant to the crossflow correlation was developed. It is shown and

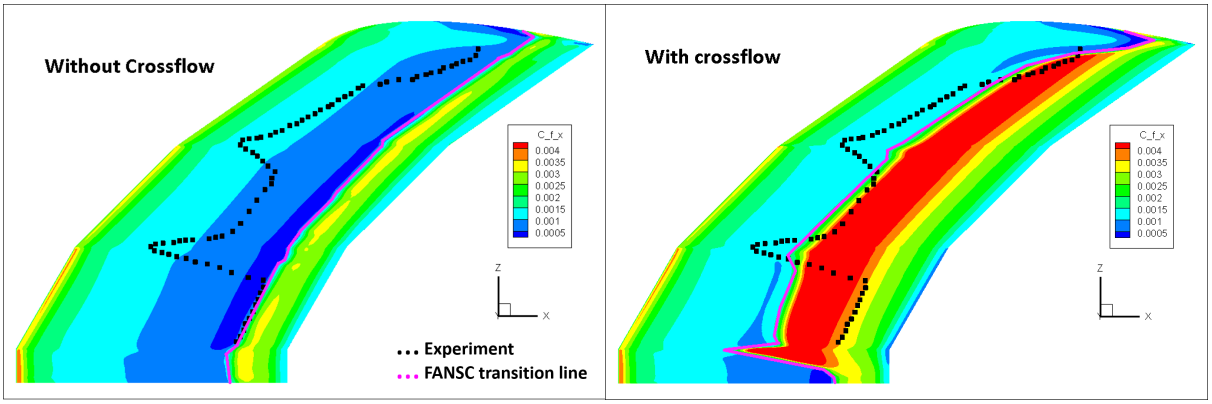

Figure 4.14 Transition prediction with and without crossflow on the Sickle-shaped wing ($M = 0.16$, $Re = 2.75 * 10^6$, $FSTI = 0.0017$, $\alpha = -2.6°$)

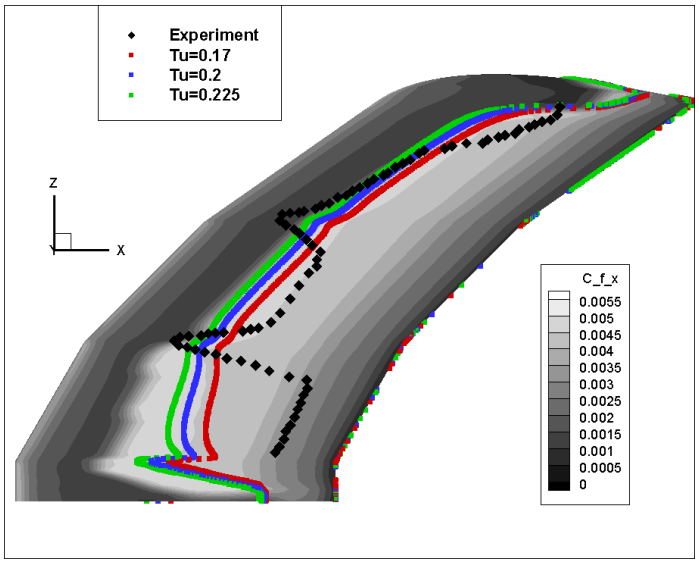

Figure 4.15 Transition prediction with crossflow and several FSTI on the Sickle-shaped wing ($M = 0.16$, $Re = 2.75 * 10^6$, $\alpha = -2.6°$)

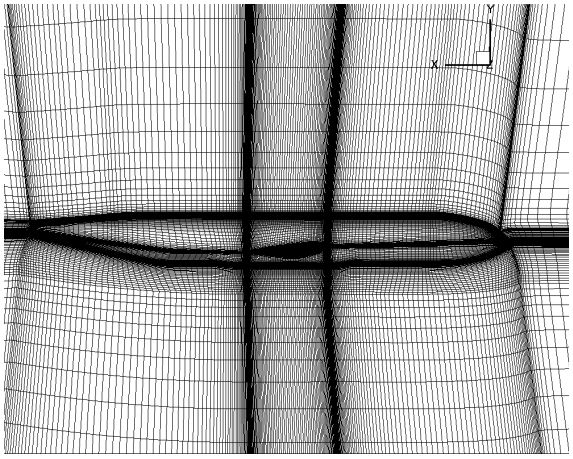

Figure 4.16 Side view of the Coarse mesh for the CRM-NLF

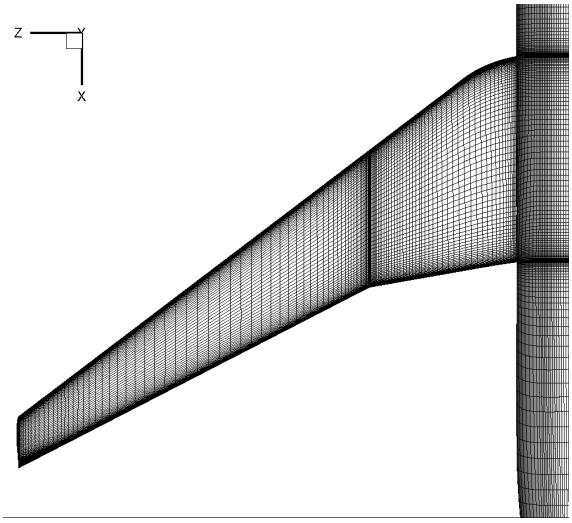

Figure 4.17 Top view of the wing on the CRM-NLF Coarse mesh

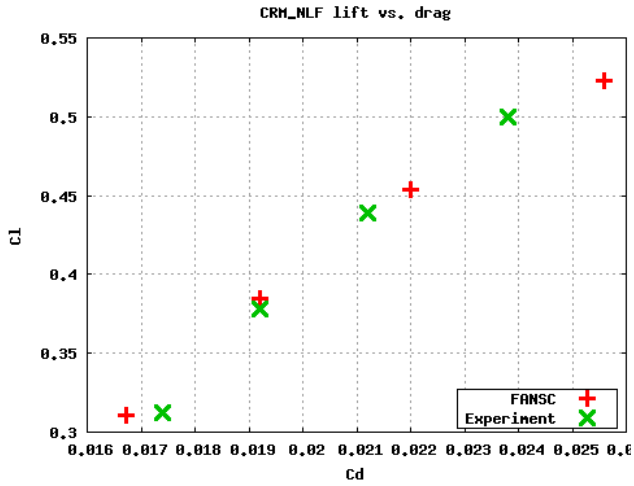

Figure 4.18 Lift / Drag comparison on the CRM-NLF

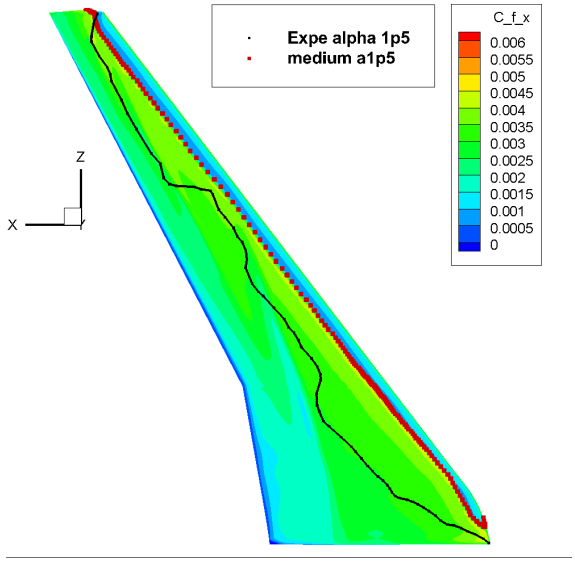

Figure 4.19 Transition line on upper surface of CRM-NLF wing $\alpha = 1.5$

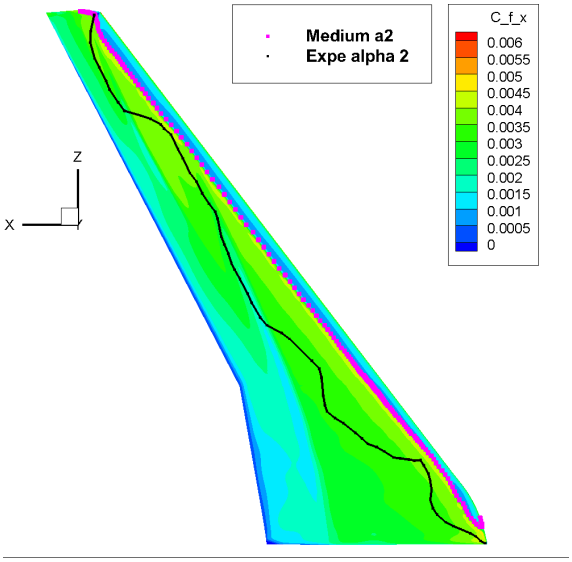

Figure 4.20 Transition line on upper surface of CRM-NLF wing $\alpha = 2.0$

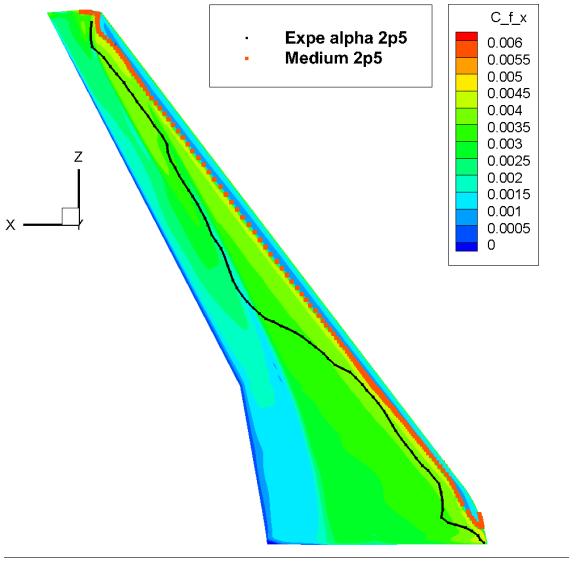

Figure 4.21 Transition line on upper surface of CRM-NLF wing $\alpha = 2.5$

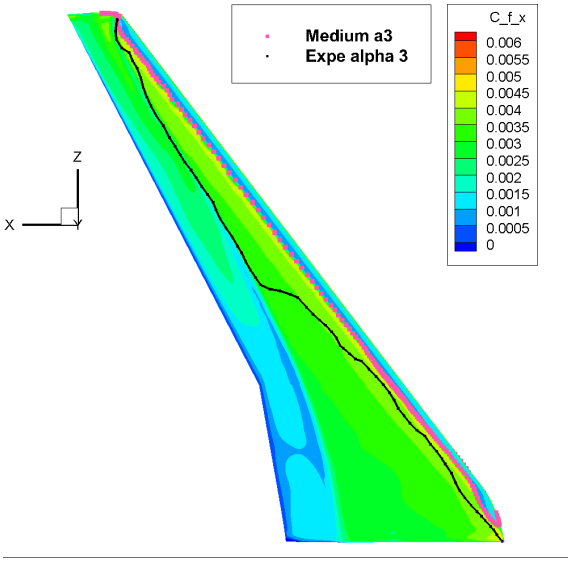

Figure 4.22 Transition line on upper surface of CRM-NLF wing $\alpha = 3.0$

Row	X_{LE} [in.]	Y_{LE} [in.]	Y/Y_{tip}	Chord [in.]	Layout
A	54.627	9.782	0.163	21.778	A
B	58.327	15.144	0.252	19.022	B
C	63.743	22.256	0.370	14.861	A
D	67.865	27.670	0.460	13.535	B
E	71.988	33.083	0.550	12.210	B
F	76.110	38.497	0.640	10.885	A
G	80.232	43.910	0.730	9.560	B
H	84.354	49.324	0.820	8.235	A
I	88.476	54.738	0.910	6.909	B

Figure 4.23 Spanwise Location of Pressure Port Rows.

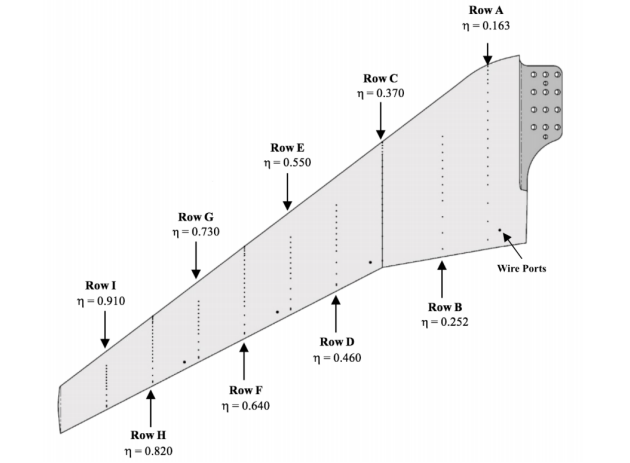

Figure 4.24 Platform View of Wing Upper Surface Showing Pressure Port Rows.

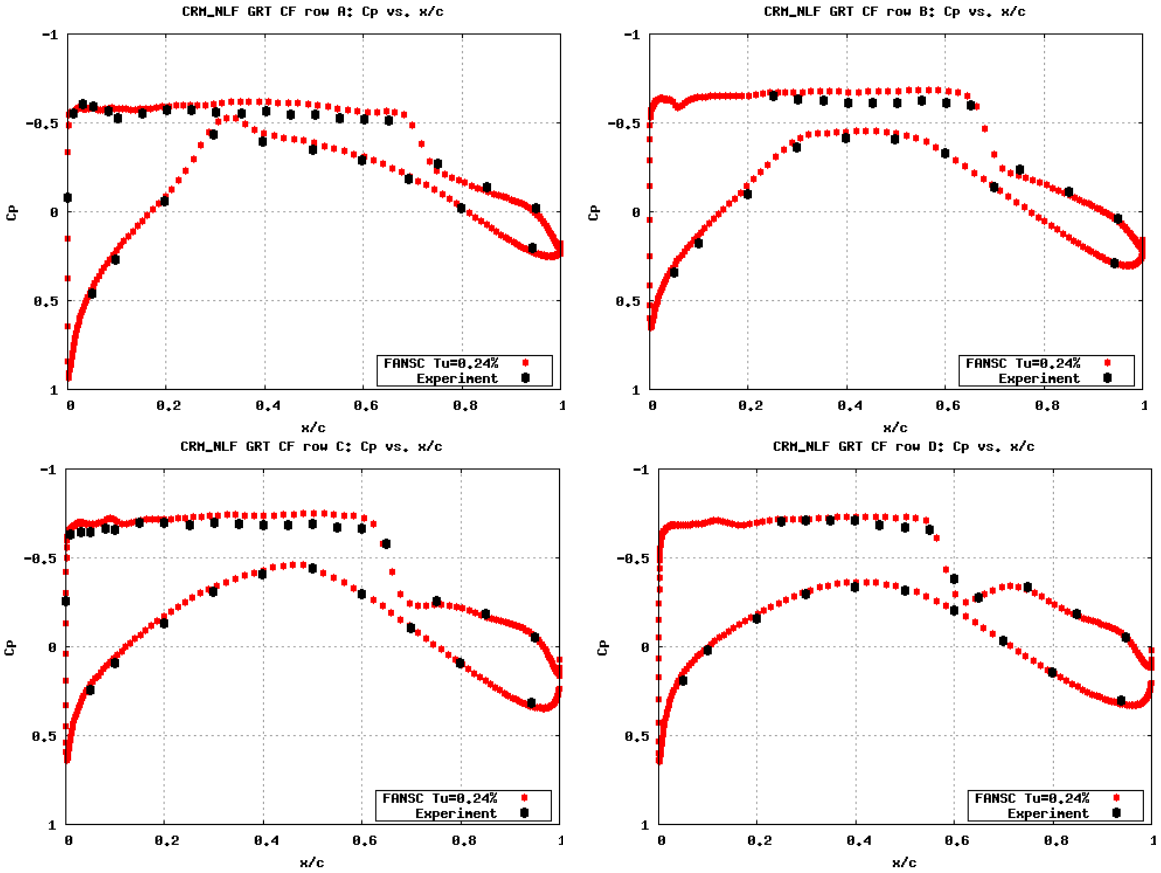

Figure 4.25 Pressure coefficient distributions on pressure rows A to D of the CRM-NLF wing

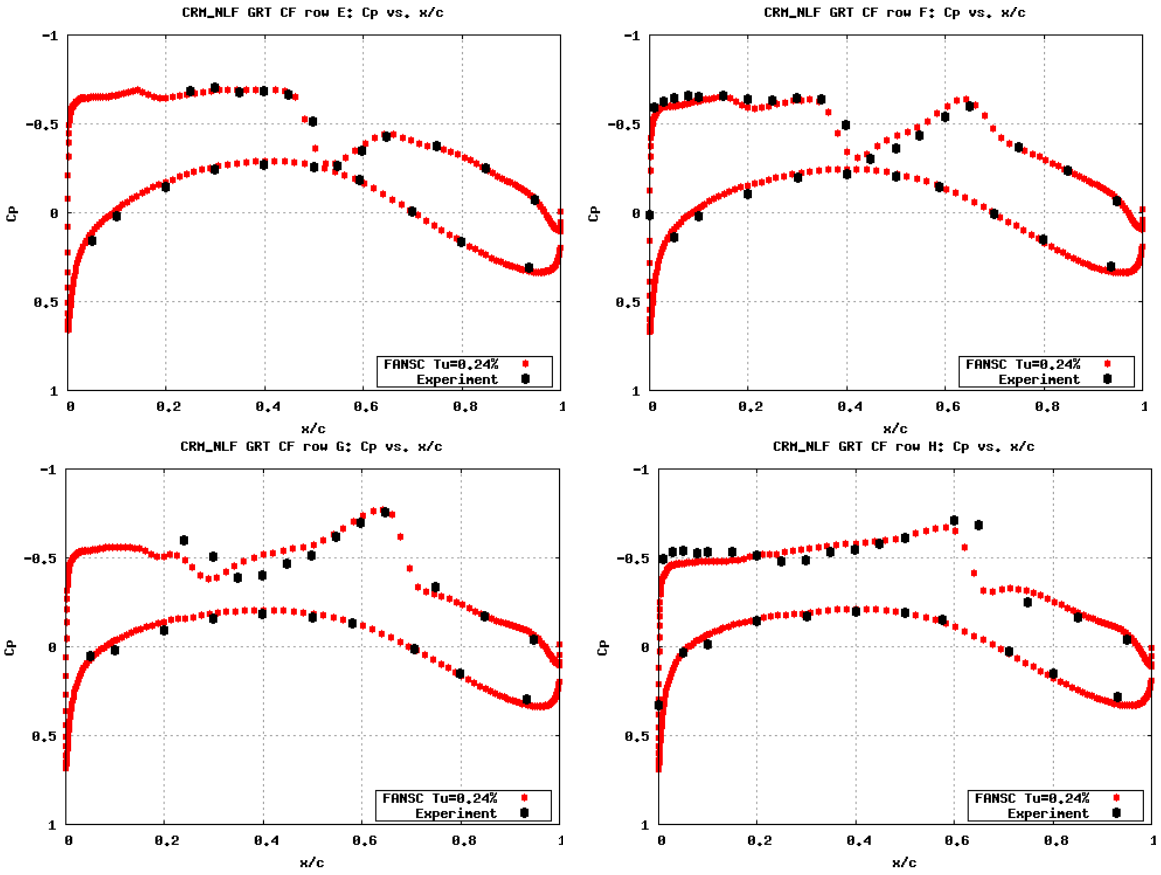

Figure 4.26 Pressure coefficient distributions on pressure rows E to H of the CRM-NLF wing

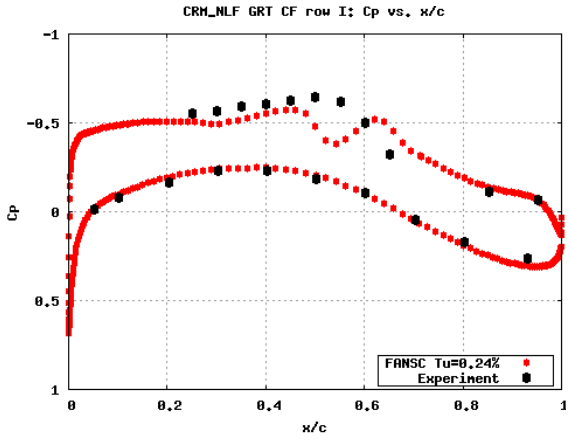

Figure 4.27 Pressure coefficient distribution on pressure row I of the CRM-NLF wing

compared to the optimized version of the correlation in Fig. 4.28. The "Sickle variant" of the correlation reduces the crossflow term to 0 for $Re_{He} < 600$ and is equal to 1.2 times the optimized version for $Re_{He} > 600$. Fig. 4.33 shows the prediction made by this version of the correlation compared to the optimized correlation and the experiment. Again, the transition line is much closer to the experiment. Negating the crossflow term for low values of Re_{He} canceled the influence of crossflow on the first section of the wing while increasing the term for high values of Re_{He} maintained the transition on the rest of the wing. This is a significant improvement from the results of the optimized crossflow extension on the sickle wing. However, the benefits observed on this case do not translate as well to the other test cases.

A similar study was conducted on the Prolate Spheroid. The optimized correlation predicts transition too far downstream on many areas of the surface. For 15 degrees angle of attack, the experimental transition line shows a kink at 130 degrees from the bottom side. The optimized correlation does not capture this feature and predicts transition 0.15 chords downstream from 0 to 130 degrees. A "Prolate Spheroid 6:1" variant to the crossflow correlation was developed to improve the results on this case only. The variant is displayed in fig. 4.28. It multiplies the crossflow term by 2 for $Re_{He} > 400$. The results of this variant are shown in Fig. 4.29 and 4.30. While the results with 5 degrees angle of attack have remained the same, the kink of the 15 degrees angle of attack is captured and can be observed at 155 degrees from the bottom side. Transition is very close to the experiment from 175 to 25 degrees. This is a dramatic improvement from the optimized version of the crossflow extension. This modification does not improve the issue of dowstream transition close to the symmetry plane.

Indeed, the current model cannot predict transition like the experiment would suggest if the crossflow extension relies mainly on helicity because the stationary solution forces helicity to be 0 at the symmetry plane. Helicity is the scalar product of velocity and vorticity. At the symmetry plane, velocity is co-linear to the plane and vorticity is orthogonal to it, meaning their product can only be 0. The value for helicity at the symmetry plane is thus 0 and gradually increases as we move away from it. This means that any non-stationary flow features that could appear where the flow separates from the surface that could create helicity and induce crossflow instabilities cannot be taken into account by this model. Consequently, the crossflow correlation as formulated in eq. 4.1 is bound to fail close to the symmetry plane. A study was conducted in which Re_{He} is forced to be greater that 500 close to the symmetry plane but away from the leading edge stagnation point. The result on the Prolate Spheroid with 5 degrees is highlighted in figure 4.31. It shows an improvement of the transition position close to the symmetry plane. Again, this is not a viable long term solution as this adjustment is not justified for other cases but it highlights a deficiency of the model.

These two studies show that the correlation can be modified to fit each case easily. The optimization algorithm was able to craft a correlation that fits most of the case relatively well and is a major improvement from the baseline model. However, some inaccuracies remain. It seems the crossflow term as formulated in eq. 4.1 cannot accurately fit both the Sickle Shaped Wing and the Prolate Spheroid cases at the same time, no matter the calibration. In addition, it seems helicity alone cannot accurately predict crossflow transition within the context of a RANS solver, as the geometrical properties of certain cases can disable it. This suggests that the formulation should be revisited with additional terms independent from helicity.

4.4 Conclusion

The γ-$Re_{\theta t}$ transition model is implemented in a structured finite volume RANS solver. A crossflow extension is added and recalibrated to better fit experimental data. The calibration is carried out using an optimization algorithm using the Nelder-Mead and Simulated Annealing methods on 2 cases. Five 3D cases are involved in the validation of the model. The crossflow extension greatly improves the accuracy of the model on all 3D cases. Results on the NLF(2)-0415 and DLR-F5 are excellent. The drag and lift coefficients on the CRM-NLF case are very close to the experiment. Finally, the results on the Prolate spheroid and the Sickle-Shaped wing have improved compared to results without crossflow terms. However, the model still has shortcomings. On the Prolate Spheroid, the model fails to capture crossflow transition where helicity is low and the model predicts transition too close to the leading edge on the first section of the Sickle-shaped wing. These deficiencies, although relatively minor compared to the improvements, could stand to be corrected. Although the model could be improved by further calibrating its constants, it is unlikely that it would suffice to solve all of the observed issues. It is more likely that the crossflow destruction term needs a more substantial modification to decrease the influence of Helicity, which seems to occasionally not be enough to capture all crossflow transition cases correctly.

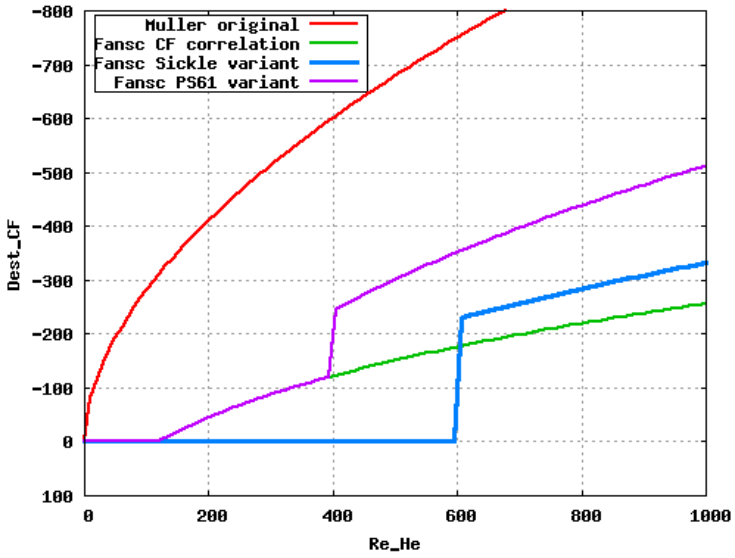

Figure 4.28 Various variants of correlations for the calculation of the crossflow destruction term in the $Re_{\theta t}$ equation

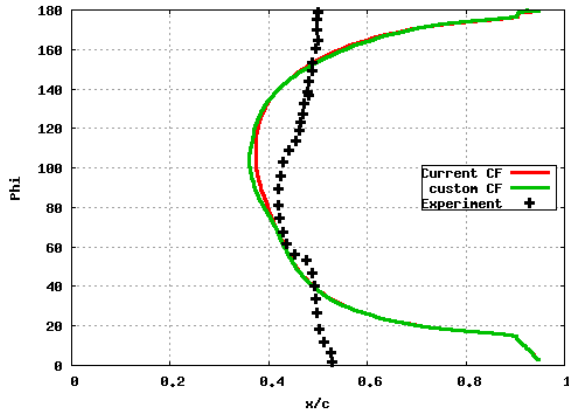

Figure 4.29 Transition prediction with current and alternative crossflow extension on the Prolate Spheroid with 5 degrees of angle of attack

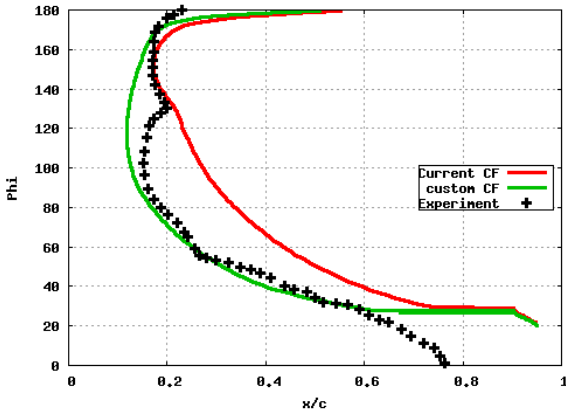

Figure 4.30 Transition prediction with current and alternative crossflow extension on the Prolate Spheroid with 15 degrees of angle of attack

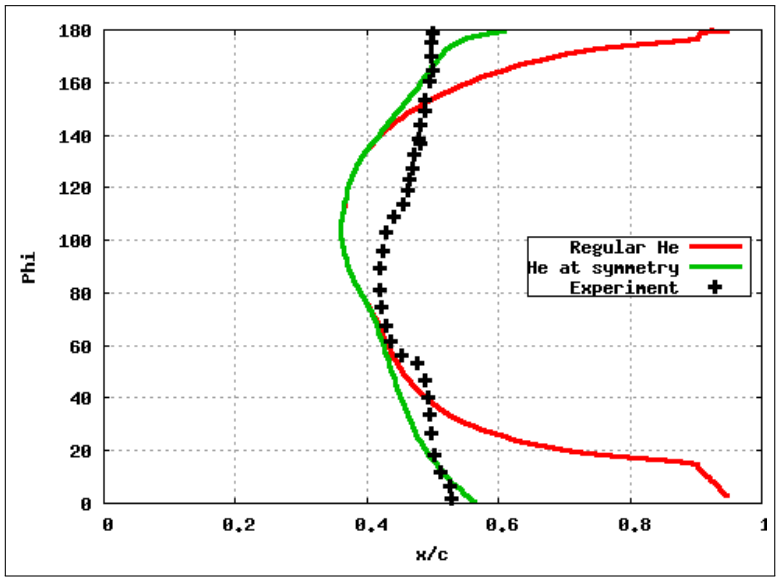

Figure 4.31 Transition prediction with higher helicity Reynolds number (minimum 500) close to the symmetry plane on the Prolate Spheroid with 5 degrees of angle of attack.

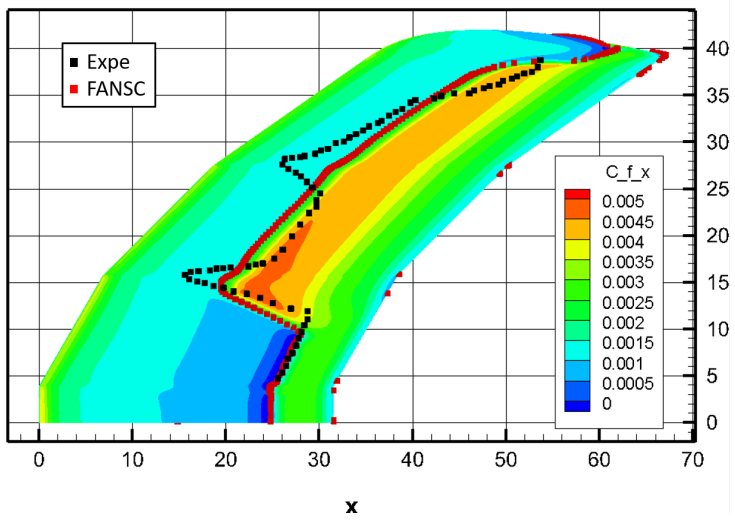

Figure 4.32 transition line and friction coefficient contours on the upper surface of the Sickle shaped wing by deactivating the crossflow effects for $z < 14$.

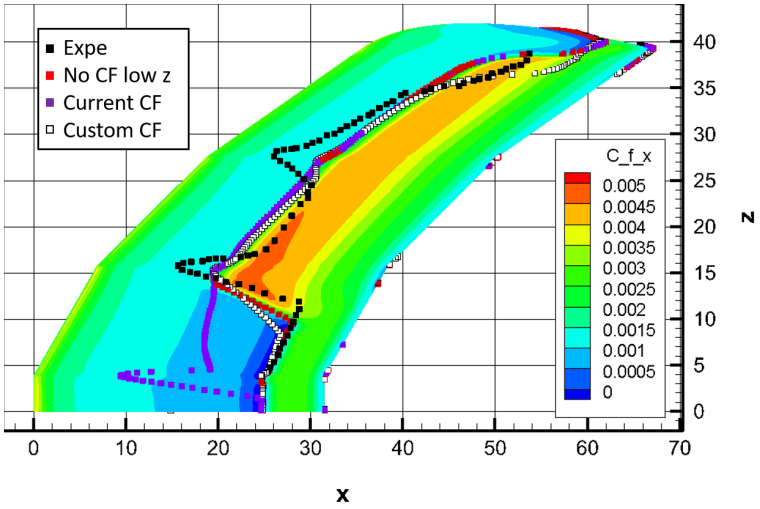

Figure 4.33 transition line and friction coefficient contours on the upper surface of the Sickle shaped wing by using the alternative crossflow extension (Fig. 4.28)

CHAPTER 5 Model sensitivity

In this chapter, we discuss the sensitivity of the model to different parameters and conditions, and how to handle them. Then, the results of a sensitivity study are shown to establish standards for which the model can be considered reliable.

5.1 Discussion and Analysis

5.1.1 Free Stream Turbulent Intensity Tu

Free stream turbulent intensity is a key parameter of the model used to define the free stream turbulent kinetic energy k (Eq. 5.1). If the turbulent intensity is high, bypass transition will take place close to the leading edge. In this case or if a laminar bubble causes transition, a small change in turbulent intensity will have a small impact on transition. However, if the turbulent intensity reaches low values (below 0.3%), natural transition or cross-flow transition will take place, in which case a small change in turbulent intensity may cause a wide displacement of transition onset.

Unfortunately, it can be difficult to accurately measure turbulent intensity in experiments. This makes calibration hard to perform and diminishes the reliability of the model. Some may have to try different values on a single test case to get the best accuracy or establish how reliable their results really are.

$$Tu = \frac{(2k/3)^{1/2}}{U} \tag{5.1}$$

5.1.2 Turbulent viscosity μ_t

Turbulent viscosity μ_t is used in conjunction with Tu to determine the free stream value of the specific turbulent dissipation rate ω (Eq. 5.2). It determines how strong the turbulent decay is. The turbulent decay is a feature of the Menter-2003 $k\omega$-SST model which has k and ω progressively decrease along the streamlines. The higher the turbulent viscosity, the slower the decay. Consequently, if μ_t is low enough and the edge of the grid is far enough from the solid, k will decease significantly from the free stream to the solid and effectively simulate a low turbulent intensity, to which the model is quite sensitive and a small variation of μ_t will significantly impact transition prediction.

$$\mu_t = \frac{k}{\omega} \tag{5.2}$$

A potential solution to this issue is the use of decay correction methods. One of these methods consists in using a non-zero floor value for k and ω, preventing them from reaching unrealistic values. This method however could have a negative influence in the sub-layer or at the stagnation point where k should be null. It has been observed that an excessively large value of turbulent intensity at the stagnation point can cause premature transition prediction [79]. This can be prevented by cancelling this floor value close to the surface.

Another option was devised by Spalart and Rumsey in 2007 [85] and consists in adding a source term in the equations for k and ω. This method can be criticized for similar reasons. The introduction of an additional source term which does not tend to 0 close to the surface could impact the boundary layer in unintended ways. The same method of canceling this term close to the surface can be used to appease this suspicion.

If either of these methods are used, the influence of μ_t on transition onset is mostly negated. Nonetheless, this parameter should not be ignored as it has a significant influence on the turbulence model and on the flow in general.

5.1.3 Mesh refinement

One concern raised by some participants of the first transition modeling workshop held in January 2021 was the difficulty of reaching grid convergence when using correlation-based transition models. Indeed, several parameters of grid generation close to the surface can impact grid convergence and transition prediction stability. The model seems sensitive to how the surface of the solid is discretized. Indeed, it has been found that the model requires a finer refinement in the streamwise direction than in the spanwise direction for wings. Also, some geometries require higher grid resolutions to reach grid convergence. Finally, changes in the wall spacing appear to disturb transition prediction and prevent grid convergence.

5.2 Test cases

A series of test cases are used to exemplify the aforementioned sensitivities. The details of each test case are displayed in table 5.1.

Table 5.1 Test cases specifics

Test case	Mach	Reynolds	transition type	FSTI(%)	$\frac{\mu_t}{\mu_l}$	α
NLF0416	0.1	$4 * 10^6$	natural/separation	0.16	10	$-9 : 9$
Sickle wing	0.16	$2.75 * 10^6$	natural+CF	0.17	10	-2.6
CRM-NLF	0.85	$15 * 10^6$	natural+CF	0.24	10	1.98

Table 5.2 Mesh specifics of the NLF0416 grids

Mesh level	Number of nodes	Nodes on surface	y+
Very Fine	1 051 137	2 048	0.1
Fine	263 425	1 024	0.2
Medium	66 177	512	0.4
Coarse	16 705	256	0.8

5.2.1 NLF0416

The NLF0416 is a natural laminar flow airfoil designed by Somers at the Langley research center in 1981 [9]. An O-type series of meshes is generated to simulate this case. The medium mesh is composed of 512 cells along the surface and 128 cells normal to it and the domain extends to 50 chords away from the airfoil. The details of each mesh are presented in table 5.3. The flow conditions are chosen as prescribed for the Transition Modeling Workshop of January 2021. Consequently, this study uses Mach 0.1, Reynolds 4 million, free stream turbulent intensity of FSTI = 0.15% and turbulent viscosity $\mu = 10$.

A grid refinement study was made to investigate the sensitivity of the model to mesh resolution. Figure 5.1 shows the progression of transition when using different grid refinements. It show qualitatively that the model's transition prediction is converged. Figure 5.4 compares lift and drag prediction for the three grid refinements. The model converges for all angles of attack. Between the medium grid and the fine grid, drag changes by about two drag counts.

The same task is performed with the medium grid using various levels of free stream turbulent intensity FSTI. Figures 5.2 and 5.3 compare the predicted transition location with angles of attack between -4 and 8 degrees using turbulent intensities between 0.01% and 0.5%. This result demonstrates the sensitivity of the model to low values of turbulent intensity. Transition on the lower side of the airfoil seems to remain close to 0.6 chords. This is due to the formation of a separation bubble where the geometry causes the flow to separate. This separation triggers transition and the flow reattaches as a turbulent boundary layer. On the upper surface, transition is natural for most of the presented turbulent intensities. At FSTI = 0.5, transition moves quite far upstream, suggesting that transition is closer to the

bypass type. Figure 5.5 shows the consequence of this behavior on lift and drag predictions. Once again, small changes in FSTI cause a substantial change in drag prediction due to a shift of transition location.

These results show that a relatively small change in FSTI causes a rather large difference in transition location and forces prediction. This feature is concerning because transition location is hard to detect accurately in experiments.The calibration of the model based on experimental data is therefore compromised. Industrial applications may suffer from this dilemma because the accuracy expected for production does not match the uncertainties of modeling and experimental measuring of transition.

5.2.2 Sickle-Shaped Wing

The Sickle-shaped wing developed by the DLR [14] is a classic test case for validation of transition models with cross-flow effects. It features several sections along the span that have varying sweep angles. The first section has 30, the second 45 and the third 55 degrees sweep angle. The upper surface of the wing is designed to amplify crossflow vortices and damp Tollmien-Schlichting waves while the lower surface amplifies both.

The geometry and the details of the case were graciously provided by the DLR. From the geometry, a series of structured meshes was generated of which the details are given in table 5.4. Two grid refinement studies were conducted. The first one scales the number of cells along the span, along the chord and in the boundary layer. The second study has a constant wall spacing of $y+ = 1.0$ for all 4 meshes.

Figure 5.6 shows the transition lines of the first grid refinement study. Transition seems to be converging at first but the last two meshes are not producing quite the same transition line. Figure 5.7 shows that with a constant wall spacing, the second grid convergence study qualitatively seems to produce a much more convincing convergence of the transition line. Figure 5.8 confirms this observation. Indeed, the drag prediction of the finest mesh does not align with the previous results for grid study 1. Grid study 2 provided a better convergence

Table 5.3 Characteristics of the Sickle shaped wing grids

Mesh level	Coarse 1	Medium	Fine 1
Number of nodes	66,177	263,425	1,051,137
Nodes along surface	513	1025	2049
Nodes normal to surface	129	257	513
y+	0.4	0.2	0.1

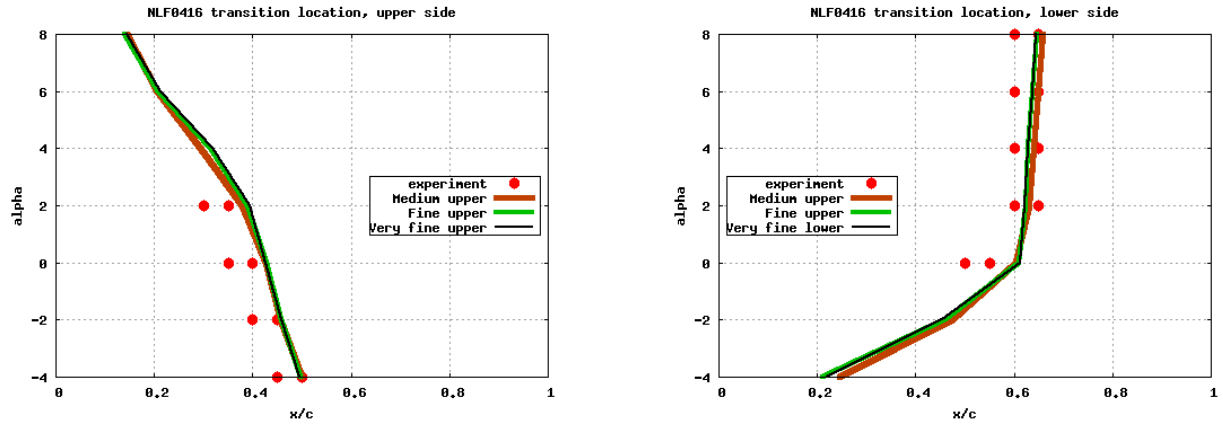

Figure 5.1 Transition location on the NLF0416 case with three grid levels. Upper side on the left and lower side on the right.($M = 0.1$, $Re = 4 * 10^6$, $FSTI = 0.15\%$,$\mu_t = 10$)

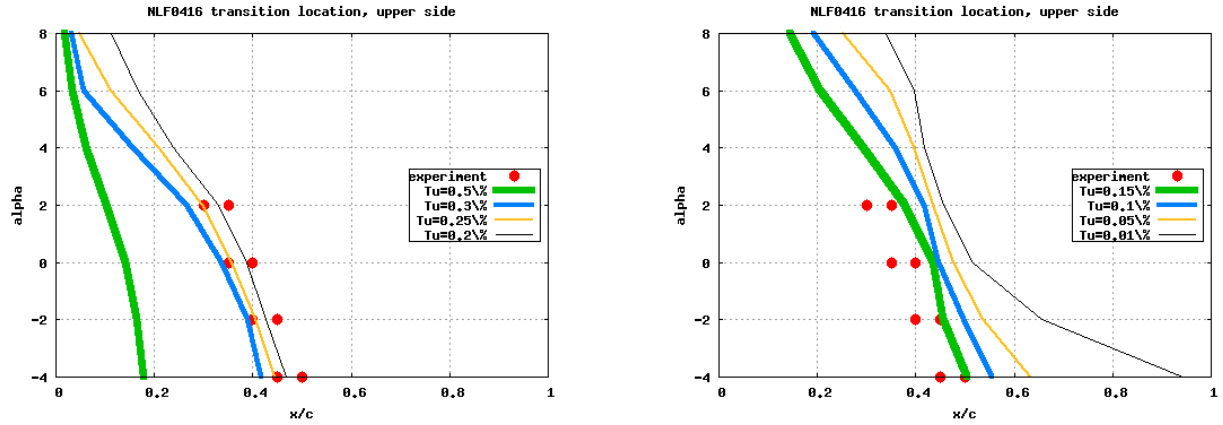

Figure 5.2 Transition location on the upper side of the NLF0416 case with several levels of free stream turbulent intensity using the Medium level grid ($M = 0.1$, $Re = 4 * 10^6$, $FSTI = 0.15\%$,$\mu_t = 10$)

Table 5.4 Characteristics of the Sickle shaped wing grids

Mesh level	Coarse 1	Medium	Fine 1	Very Fine 1	C. 2	M.	F. 2	V. F. 2
Nodes	10.1M	19.8M	61.7M	313M	10.5M	19.8M	50.3M	165.6M
Streamwise	100	200	400	800	100	200	400	800
Spanwis	100	200	400	800	100	200	400	800
y+	2.0	1.0	0.5	0.25	1.0	1.0	1.0	1.0

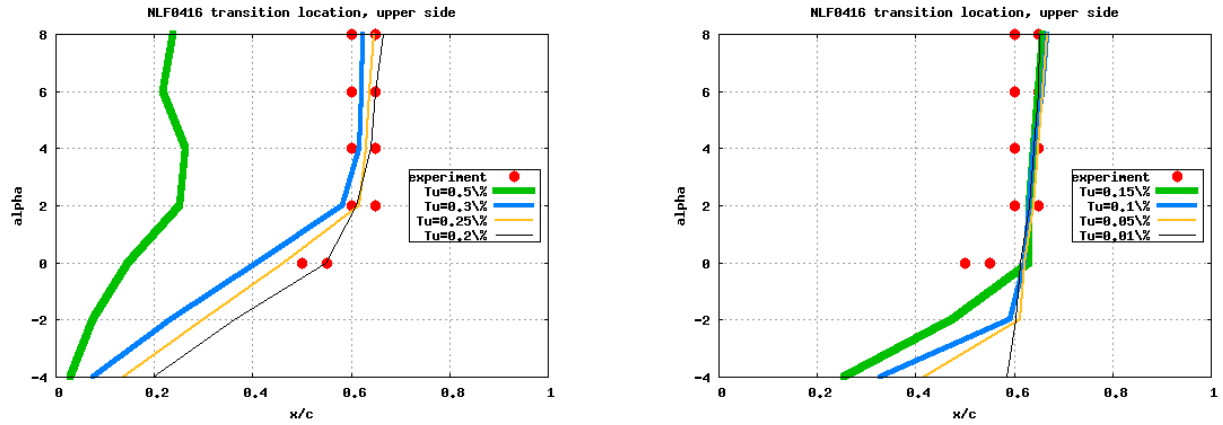

Figure 5.3 Transition location on the lower side of the NLF0416 case with several levels of free stream turbulent intensity using the Medium level grid ($M = 0.1$, $Re = 4 * 10^6$, $FSTI = 0.15\%$,$\mu_t = 10$)

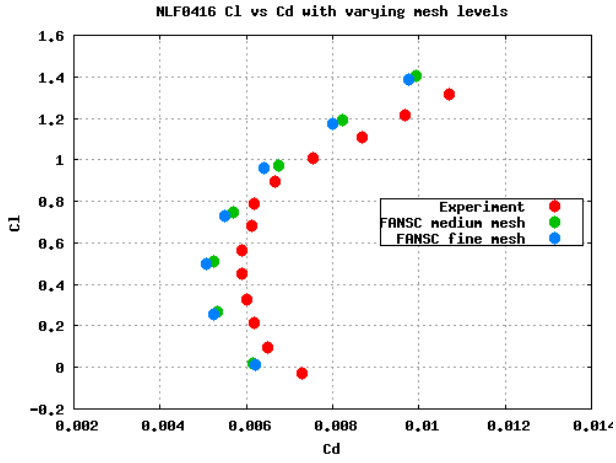

Figure 5.4 Lift and drag predictions on the NLF0416 case using several levels of grid refinements($M = 0.1$, $Re = 4 * 10^6$, $FSTI = 0.15\%$,$\mu_t = 10$)

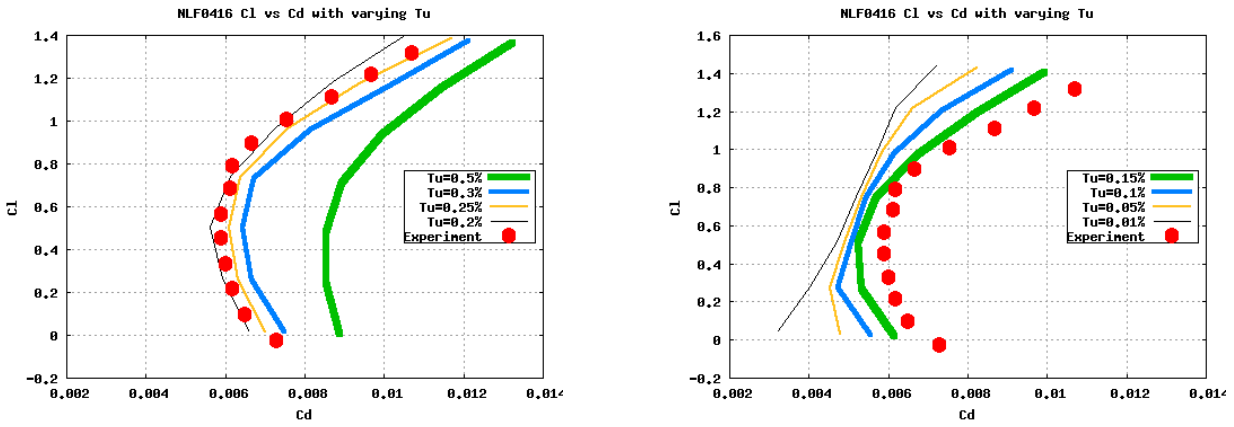

Figure 5.5 Lift and drag predictions on the NLF0416 case using the medium level grid with varying levels of FSTI($M = 0.1$, $Re = 4 * 10^6$,$\mu_t = 10$)

of the drag, which suggests that the model is sensitive to wall spacing and mesh refinement in the boundary layer not only when transition is natural but also when crossflow effects are involved. When compared to the results obtained for the NLF0416, these observations suggest that the model's sensitivities are not the same in 2D cases as in 3D cases. Indeed, the model did not show a particular dependence to wall spacing on the NLF0416 case but does on the Sickle wing case.

5.2.3 CRM-NLF

Finally, the CRM-NLF case is used to study the sensitivity effects on a full aircraft with a natural laminar design wing in subsonic conditions. It is a good example of a case where most correlation based models seem to disagree with experimental results when it comes to the transition line on the wing. This case features the following flow conditions: $M = 0.85$, $15 * 10^6$, FSTI $= 0.24\%$, $\mu_t = 10$, $\alpha = 1.98$.

A grid refinement study was conducted to establish the ability of the model to converge on this particular case. A series of meshes was created of which the details are given in table 5.5.

Figure 5.9 shows that the model's drag prediction converges relatively well. However, the lift prediction does not confirm this observation, as shown in figure 5.10. Still, the changes in lift between different discretizations are relatively small and it can be considered that this apparent trend may not be characteristic of the model's behavior.

Fig. 5.9 shows the progression of drag coefficient with mesh refinement. It seems the model follows an asymptotic behavior. This trend is not confirmed by the progression of lift co-

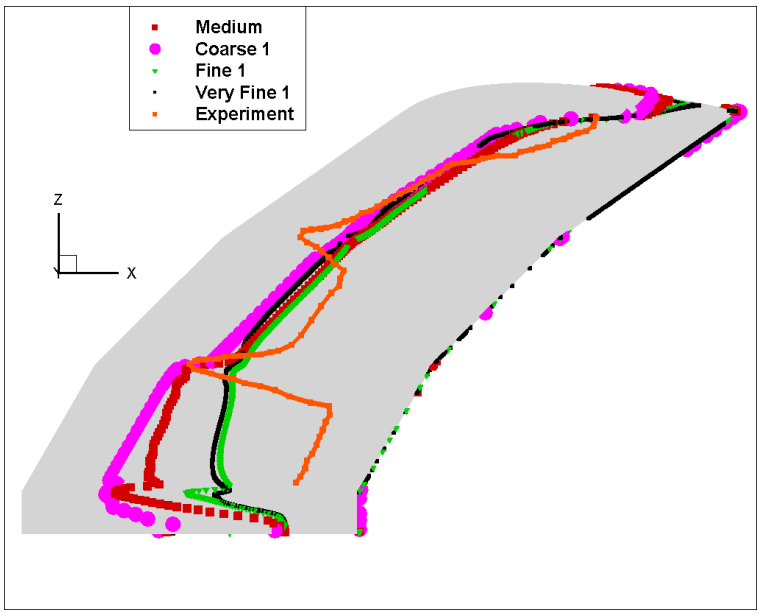

Figure 5.6 Transition lines along the Sickle-shaped wing for several grid refinements and varying wall spacing ($M = 0.16$, $Re = 2.75 * 10^6$, $FSTI = 0.0017$, $\mu_t/\mu_l = 10$, $\alpha = -2.6°$)

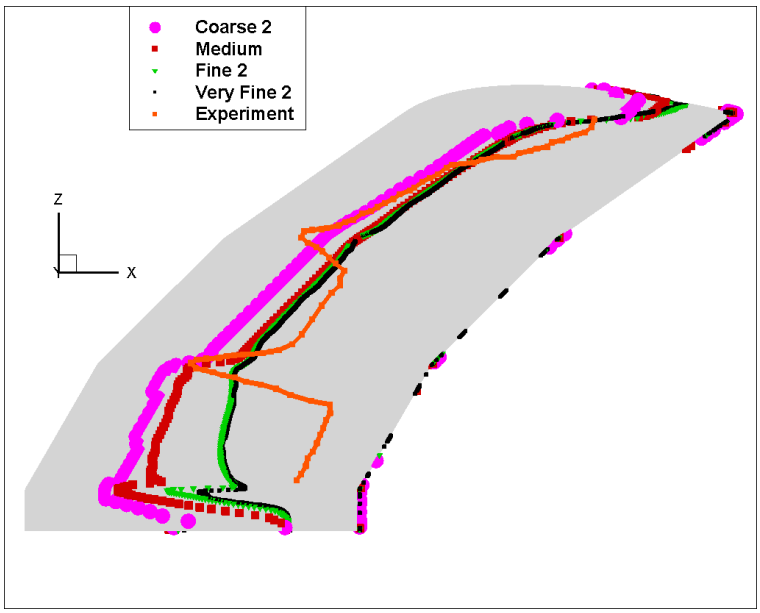

Figure 5.7 Transition lines along the Sickle-shaped wing for several grid refinements and constant wall spacing ($M = 0.16$, $Re = 2.75 * 10^6$, $FSTI = 0.0017$, $\mu_t/\mu_l = 10$, $\alpha = -2.6°$)

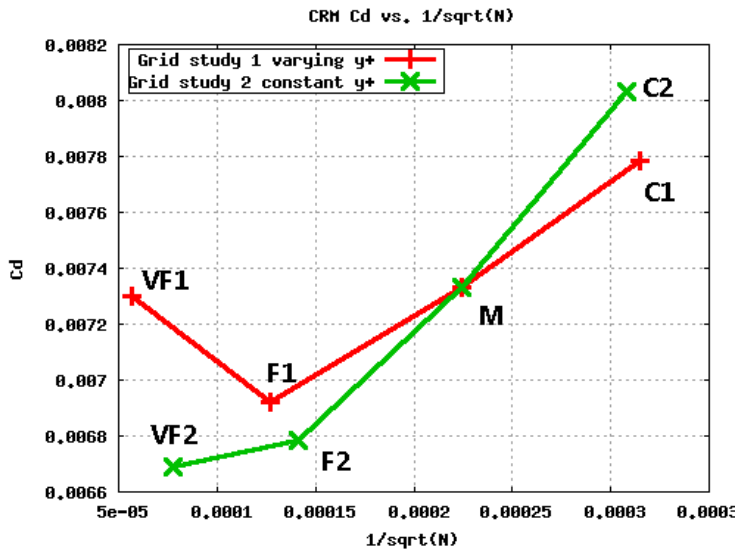

Figure 5.8 Drag predictions on the Sickle-shaped wing for several grid refinements and wall spacing policies ($M = 0.16$, $Re = 2.75 * 10^6$, $FSTI = 0.0017$, $\mu_t/\mu_l = 10$, $\alpha = -2.6°$)

efficient with mesh refinement as shown in figure 5.10. However, one can notice that the changes in lift are rather small and it can be considered that this apparent trend may not be characteristic of the model's behavior.

The behavior of the lift coefficient could be placed on the shock displacement caused by a movement of the transition location. Indeed, even though transition seems to converge, the variation between meshes causes the transonic shock to move. This is because the position of the shock is in part determined by the boundary layer thickness. This phenomenon has also been observed in the sensitivity study of [81].

Figure 5.11 shows the model's transition prediction compares to the experimental measure of transition. It is apparent that the model predicts transition far upstream from the experiment. Figures 5.12, 5.13 and 5.14 show how this transition prediction evolves as the mesh is refined. Transition progressively moves downstream as the mesh is refined. As expected, transition seems to converge as the mesh is refined. It appears that the prediction grows closer to the experiment. More importantly, the tip of the wing features a pocket of laminar boundary layer that appears in the finest resolutions of the study. This indicates that the model can capture the physics involved but may be limited by its sensitivity to various factors.

A turbulent intensity study is led on this case to determine if some of the disagreements with the experiment could be caused by a shift of turbulent intensity in the calibration of the

model. To visualize the influence of FSTI on the results, the experimental measures of Cp along key chords of the wing are compared to their computational counterpart. Figure 5.15 details the position of the pressures rows from row "A" to row "I" moving outwards. Figures 5.16 to 5.24 show the pressure coefficient distribution predicted by the model with 3 different FSTI: 0.24%, 0.15% and 0.06%. It appears that the further away a row is from the root of the wing, the more results are affected by the FSTI. What is even more interesting is that the position of the transonic shocks can move by a few percentiles of the chord when the value of FSTI is modified by 0.09%. The reason for this movement is that the position of the shock is in part determined by the boundary layer thickness. However, depending on the position of transition, the boundary layer thickness at a given point on the surface may vary. The closer the transition is to the leading edge, the thicker the boundary layer dowstream of this point. Consequently, the variations of FSTI cause a movement of transition which changes the distribution of boundary layer thickness along the surface of the wing which in turn displaces the transonic shock.

Shock displacements of this magnitude have a significant impact on the prediction of aerodynamic forces and maximum lift. Such an issue weighs heavily on the attractiveness of the model for industrial applications.

5.3 Conclusion

Studies are made on several 2D and 3D cases to investigate the sensitivity of the model to mesh refinement and Free Stream Turbulence Intensity. It is found that the model does not appear to suffer from mesh sensitivity for 2D cases with mixed behaviours on 3D cases like the Sickle shaped wing and the CRM-NLF configuration. Indeed for the Sickle wing case, whereas global mesh refinement leads to non-monotonic mesh convergence, a mesh refinement keeping a constant y+ value leads to improved numerical behaviour. For cases with low free stream turbulence intensity, a small change in turbulence can cause a large variation of transition onset location. This sensitivity is observed both on 2D ans 3D cases. When applied to transonic cases, this issue can cause small displacements of transonic shocks because transition influences the boundary layer thickness. This feature of the model raises the question of the validity of calibrations based on experimental results. Indeed, transition

mesh level	Very Coarse	Coarse	Medium	Fine	Very Fine
number of nodes	3.69M	7.87M	24.8M	75.9M	213.8M

Table 5.5 Mesh specifics of the CRM-NLF case

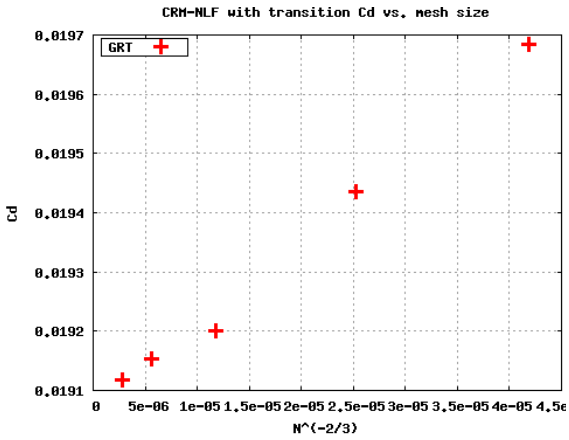

Figure 5.9 Drag prediction on the CRM-NLF with several mesh refinements

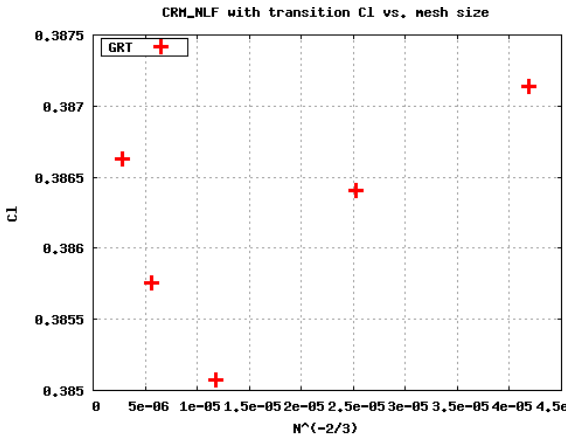

Figure 5.10 Lift prediction on the CRM-NLF with several mesh refinements

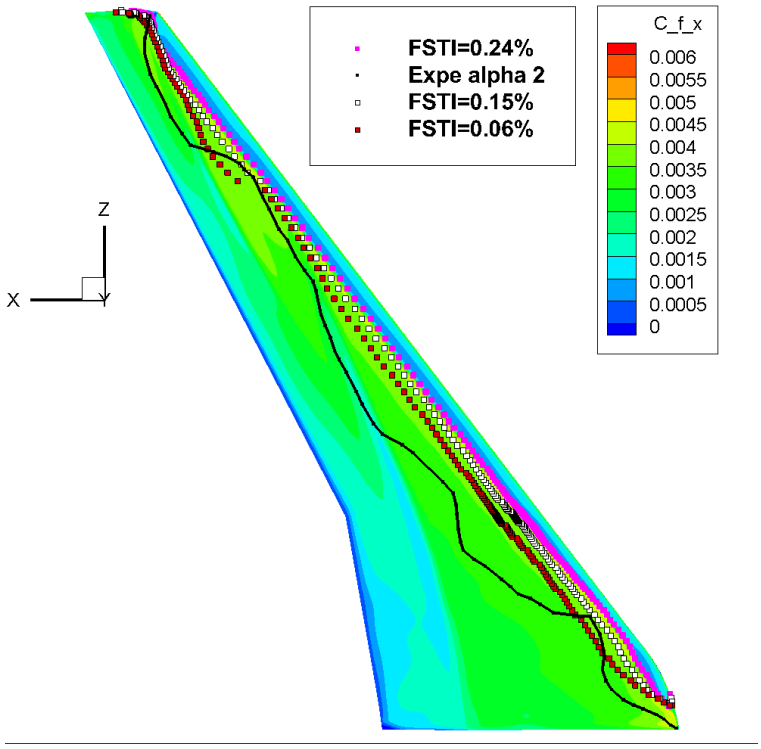

Figure 5.11 Transition line on upper surface of CRM-NLF wing $\alpha = 2.0$

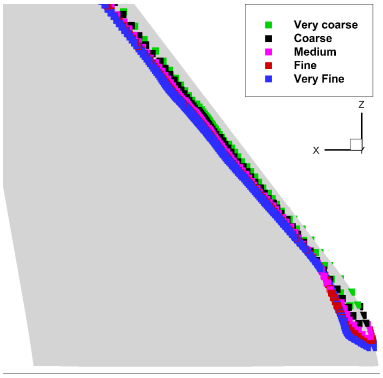

Figure 5.12 Transition line at the **root** of upper surface of CRM-NLF wing

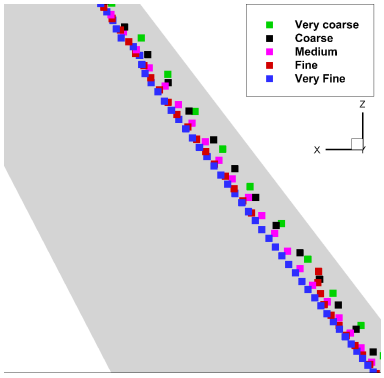

Figure 5.13 Transition line on **middle portion** of upper surface of CRM-NLF wing

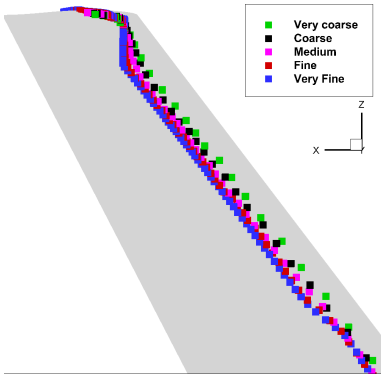

Figure 5.14 Transition line at the **tip** of upper surface of CRM-NLF wing

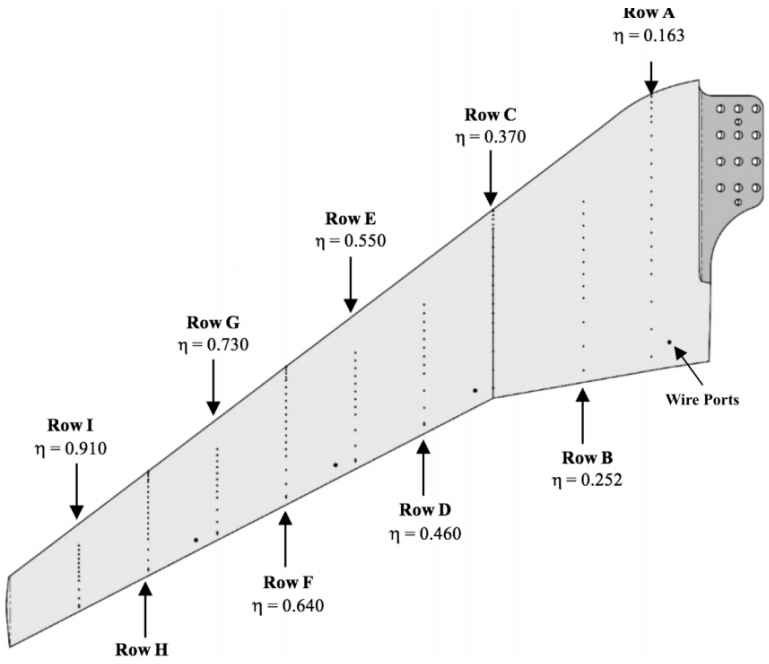

Figure 5.15 Platform view of CRM-NLF wing upper surface showing pressure port rows

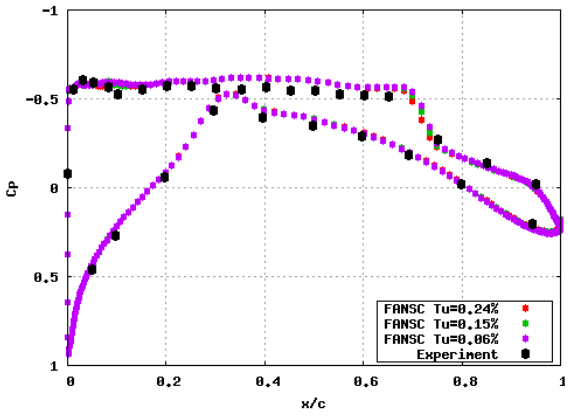

Figure 5.16 Pressure coefficient distribution on pressure row A of the CRM-NLF wing

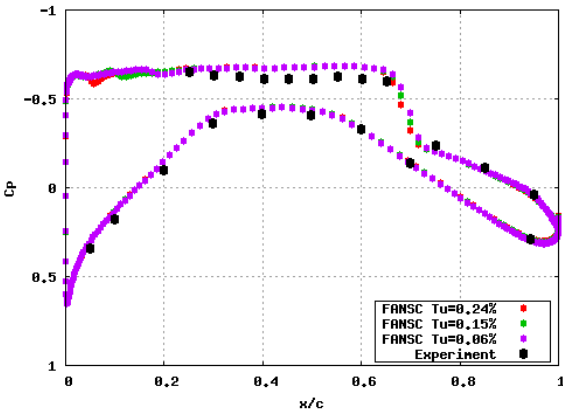

Figure 5.17 Pressure coefficient distribution on pressure row B of the CRM-NLF wing

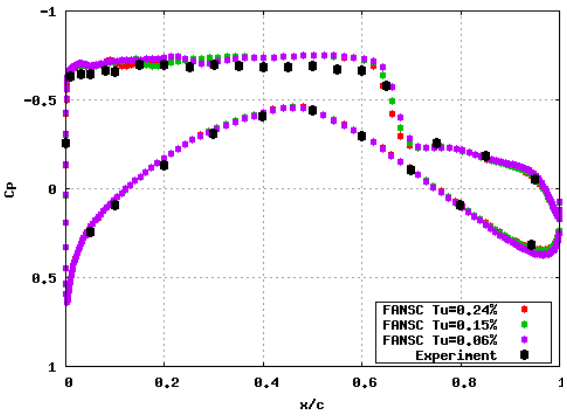

Figure 5.18 Pressure coefficient distribution on pressure row C of the CRM-NLF wing

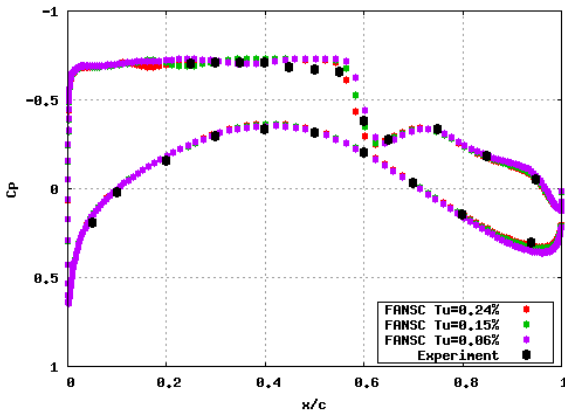

Figure 5.19 Pressure coefficient distribution on pressure row D of the CRM-NLF wing

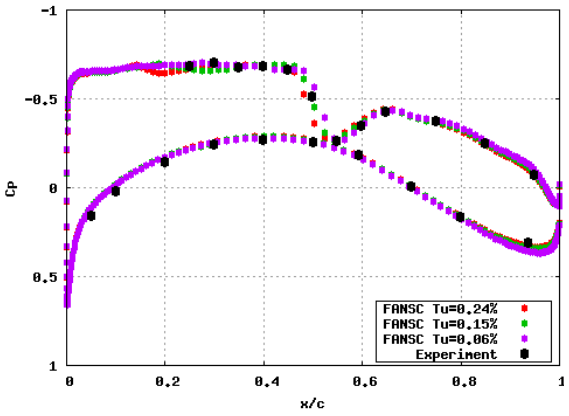

Figure 5.20 Pressure coefficient distribution on pressure row E of the CRM-NLF wing

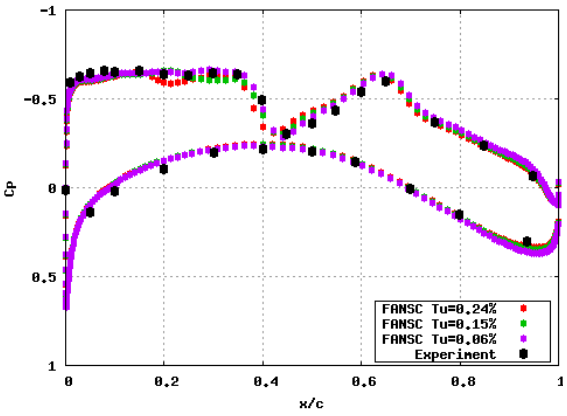

Figure 5.21 Pressure coefficient distribution on pressure row F of the CRM-NLF wing

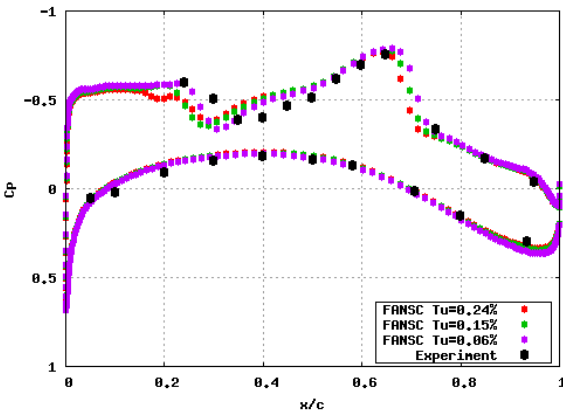

Figure 5.22 Pressure coefficient distribution on pressure row G of the CRM-NLF wing

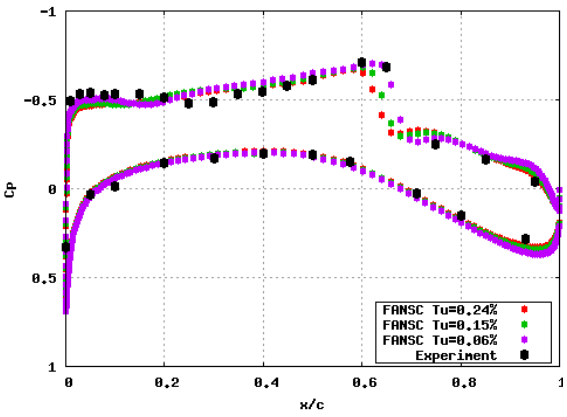

Figure 5.23 Pressure coefficient distribution on pressure row H of the CRM-NLF wing

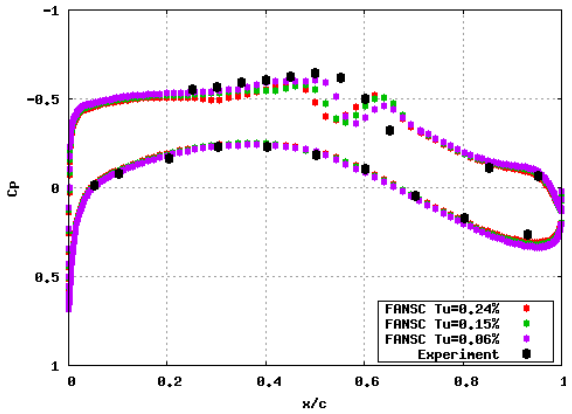

Figure 5.24 Pressure coefficient distribution on pressure row I of the CRM-NLF wing

is quite hard to reliably measure experimentally, which means that results are subject to high uncertainties. In this context, the validation of correlation based transition models is made complex to perform as sensitivities of experiments and models alike push authors to make compromises and assumption in the hope that inconsistencies are only mere artifacts of highly non-linear physical phenomena.

CHAPTER 6 CONCLUSION

Methods were designed to allow users to implement the grt model and recalibrate it for the needs of their solver. The modified model was validated on a large series of 2D test cases and tested on a few 3D cases. A crossflow extension was implemented and validated and sensitivities and potential deficiencies of the model were investigated.

The first step of this work was the implementation of the γ-$Re_{\theta t}$ correlation based transition model in a structured finite volume RANS code. Modifications were brought to the model to improve the robustness and accuracy of the implementation. An optimization algorithm was developed to help in this process, for which the Nelder-Mead method was chosen as a basis. Results were obtained for a range of 2D test cases that cover natural, bypass and separation induced transition on both flat plates and airfoils under various flow conditions. The 2D results show good agreement with experimental measurements as well as with other numerical studies. Several 3D cases from the literature were studied, such as the Prolate spheroid, the Sickle wing and DLR-F5 wings. Predictions on the 3D cases show discrepancy with experimental results where crossflow effects dominate the boundary layer, as the model in its current implementation has no means of taking this type of transition into account. However, if natural or separation induced transition takes over, the model shows an appropriate agreement with experimental observations. Efforts were made to optimize the model's convergence properties. Special attention was brought to non-differentiable functions, pseudo-time stepping and segregation of the equations. As a result, the model turns out to be ready for industrial applications where crossflow effects are negligible.

After the validation of the base model, a crossflow extension was added and recalibrated to better fit experimental data. The calibration was carried out using an optimization algorithm using the Nelder-Mead and Simulated Annealing methods on 2 cases. Several methods were applied to improve features of the solver. Five 3D cases were involved in the validation of the model. The crossflow extension greatly improved the accuracy of the model on all 3D cases. Results on the NLF(2)-0415 and DLR-F5 were excellent. The drag and lift coefficients on the CRM-NLF case were very close to the experiment. Finally, the results on the Prolate spheroid and the Sickle-Shaped wing have improved compared to results without crossflow terms. However, the model still has shortcomings. On the Prolate Spheroid, the model fails to capture crossflow transition where helicity is low and the model predicts transition too close to the leading edge on the first section of the Sickle-shaped wing. These deficiencies, although relatively minor compared to the improvements, stand to be corrected. Although

the model could be improved by further calibrating its constants, it is unlikely that it would suffice to solve all of the observed issues.

Last but not least, studies were made on several 2D and 3D cases to investigate its sensitivity to mesh refinement and Free Stream Turbulence Intensity. It was found that the model does not appear to suffer from mesh sensitivity for 2D cases with mixed behaviours on 3D cases like the Sickle shaped wing and the CRM-NLF configuration. Indeed for the Sickle wing case, whereas global mesh refinement leads to non-monotonic mesh convergence, a mesh refinement keeping a constant y+ value leads to improved numerical behaviour. For cases with low free stream turbulence intensity, a small change in turbulence can cause a large variation of transition onset location. This sensitivity is observed both on 2D ans 3D cases. When applied to transonic cases, this issue can cause small displacements of transonic shocks because transition influences the boundary layer thickness. This feature of the model raises the question of the validity of calibrations based on experimental results. Indeed, transition is quite hard to reliably measure experimentally, which means that results are subject to high uncertainties. In this context, the validation of correlation based transition models is made complex to perform as sensitivities of experiments and models alike push authors to make compromises and assumption in the hope that inconsistencies are only mere artifacts of highly non-linear physical phenomena.

6.1 Contributions

The process of recalibration of the base model brought new understandings of the behavior of each term, and how they function when modified. With this knowledge, we provide a guide on how to calibrate or modify the model based on each code specification or issues encountered when using the model. The key modifications brought to the model include the smoothing of sharp discontinuities in the model's functions which improved the convergence rate and robustness. Two key constants were recalibrated. This resulted in improved agreement with experimental results. In addition, to avoid unnaturally high values of turbulent intensity at he the leading edge, turbulent intensity was reformulated. This resulted in improved behavior of the model for the flat plate cases in which a singularity appears at its leading edge and for airfoils at high angles of attack.

Moreover, to efficiently recalibrate the model, an optimization method was developed. This automatizes the process of calibration notably through a gradient-based transition extraction criteria and ensures that the model reaches its optimal agreement with experiments given its formulation. Using the same method, a crossflow extension was recalibrated and the model was shown to perform well on numerous cases. This shows that this calibration method could

be applied on many correlation based models.

6.2 Limitations and recommendations

Some sensitivities of the model were uncovered within the literature and within this work. In particular, the position of transition is sensitive to small changes in the freestream turbulent intensity. This shows that the model should be used with caution on some applications for which turbulent intensity and other parameters are not directly available, which is a problem for accuracy. This issue takes us back to the problem of experimental observation of transition which is not an easy task to perform. Transition experiments are often not well repeatable and measurement methods often do not allow a high level of accuracy. This contrasts with the industry's high standards of accuracy for CFD.

The sensitivity study presented in this work outlines some slight discrepancies of the crossflow extension. The model appears to be particularly sensitive to freestream turbulent intensity. It was revealed during the first AIAA transition modeling workshop that many members of the research community have difficulties meeting grid convergence. Similarly, some of the workshop results showed that small changes in freestream turbulent intensity could significantly affect transition. Finally, on some cases of the workshop, the results where where quite different from participant to participant, which suggests that the implementation of the model is hard to replicate and sensitive to the coupled turbulence model and solver. The present sensitivity study demonstrates that the recalibrated model fails to fit some parts of the experimental results chosen for validation. Considering the re-calibration process and its results, it is reasonable to assume that the formulation of the present extension does not allow the model to fit experimental results regardless of the calibration. A more complex formulation is needed to improve results further.

The crossflow extension relies heavily on a correlation between crossflow effects and local helicity. However, this value comes with its own problems. Indeed, it does not behave adequately close to symmetry boundaries. Unfortunately, these are quite common in RANS modelling. Potential improvements may come from developing an additional term for the crossflow extension to add dependency to another value. Candidates for this value could be the local sweep angle or a second derivative of vorticity.

REFERENCES

[1] F. R. Menter and R. B. Langtry, *Transition Modelling for Turbomachinery Flows*, 2012.

[2] A. Mosahebi and E. Laurendeau, "Introduction of a modified segregated numerical approach for efficient simulation of gamma re theta transition model," *International Journal of Computational Fluid Dynamics*, vol. 29, no. 6-8, 2015. [Online]. Available: http://www.tandfonline.com/doi/full/10.1080/10618562.2015.1093624

[3] N. AGENCY, "SP-367 Introduction to the Aerodynamics of Flight, Chapter V. TRANSONIC FLOW." [Online]. Available: https://history.nasa.gov/SP-367/chapt5.htm#f86

[4] N. Gregory and C. L. O'reilly, *Low-Speed aerodynamic characteristics of NACA 0012 aerofoil section, including the effects of upper-surface roughness simulating hoar frost.* HM Stationery Office London, 1973.

[5] G. B. Schubauer and P. S. Klebanoff, "Contributions on the mechanics of boundary-layer transition," *NACA TN 3489*, 1955.

[6] A. M. Savill, *One-point closures applied to transition.* Springer, 1996, vol. Turbulence and transition modelling.

[7] ——, "Some recent progress in the turbulence modelling of by-pass transition," *Near-wall turbulent flows*, pp. 829–848, 1993.

[8] D. M. Somers, "Design and experimental results for the S809 airfoil," National Renewable Energy Lab., Tech. Rep., 1997.

[9] ——, "Design and Experimental Results for a Flapped Natural-Laminar-Flow Airfoil for General Aviation Applications," NASA Langley Research Center, Tech. Rep., 1981.

[10] H. P. Kreplin, H. Vollmers, and H. U. Meier, "Wall shear stress measurements on an inclined prolate spheroid in the DFVLR 3m-x-3m low speed wind tunnel, göttingen, DFVLR-AVA," 1985.

[11] C. Grabe, N. Shengyang, and A. Krumbein, "Transition Transport Modeling for the Prediction of Crossflow Transition." American Institute of Aeronautics and Astronautics, 2016. [Online]. Available: http://arc.aiaa.org/doi/10.2514/6.2016-3572

[12] R. Petzold and R. Radespiel, "Transition on a Wing with Spanwise Varying Crossflow and Linear Stability Analysis," *AIAA Journal*, vol. 53, no. 2, 2015. [Online]. Available: http://arc.aiaa.org/doi/10.2514/1.J053127

[13] M. Kruse *et al.*, "Transition Prediction Results for Sickle Wing and NLF(1)-0416 Test Cases." American Institute of Aeronautics and Astronautics, 2018. [Online]. Available: https://arc.aiaa.org/doi/10.2514/6.2018-0537

[14] R. Petzold and R. Radespiel, *Transition on a Wing with Spanwise Varying Crossflow Evaluated with Linear Stability Theory, 43rd AIAA Fluid Dynamics Conference*, 2013.

[15] H. Sobieczky, "DLR - f5: Test wing for CFD and applied aerodynamics." [Online]. Available: http://www.as.dlr.de/hs/h-pdf/H085.pdf

[16] G. Schrauf, "ON ALLOWABLE STEP HEIGHTS: LESSONS LEARNED FROM THE F100 AND ATTAS FLIGHT TESTS," p. 12, 2018.

[17] K. H. Horstmann, "Contribution to Laminar Wing Development for Future Transport Aircraft," p. 19, 2006.

[18] M. N. Lynde and R. L. Campbell, "Crossflow Attenuated Natural Laminar Flow for Transport Wings," p. 44, 2021.

[19] "Advanced Laminar Flow tAilplane report," European Comission, FOKKER AEROSTRUCTURES BV, Tech. Rep. 263243, Aug. 2019.

[20] J. Slotnick *et al.*, "CFD Vision 2030 Study: A Path to Revolutionary Computational Aerosciences," p. 58.

[21] J. Blazek, *Computational fluid dynamics: principles and applications*, third edition ed. Amsterdam: Butterworth-Heinemann, 2015, oCLC: ocn909314295.

[22] B. S. Baldwin, H. Lomax, and N. Ames, "Thin Layer Approximation and Algebraic for Separated Turbulent Flows," p. 9, 1978.

[23] D. A. Johnson and L. S. King, "A mathematically simple turbulence closure model for attached and separated turbulent boundary layers," *AIAA Journal*, vol. 23, no. 11, pp. 1684–1692, Nov. 1985. [Online]. Available: https://arc.aiaa.org/doi/10.2514/3.9152

[24] P. Spalart and S. Allmaras, "A One-Equation Turbulence Model for Aerodynamic Flows," *AIAA Paper*, no. 92-0439, 1992.

[25] S. R. Allmaras, P. Spalart, and T. F. Johnson, "Modifcations and Clarifcations for the Implementation of the Spalart-Allmaras Turbulence Model," 2012.

[26] N. Burgess and D. Mavriplis, "Robust Computation of Turbulent Flows Using a Discontinuous Galerkin Method." American Institute of Aeronautics and Astronautics, Jan. 2012. [Online]. Available: http://arc.aiaa.org/doi/10.2514/6.2012-457

[27] S. C. Cakmakcioglu *et al.*, "A Revised One-Equation Transitional Model for External Aerodynamics," in *AIAA AVIATION 2020 FORUM*. VIRTUAL EVENT: American Institute of Aeronautics and Astronautics, Jun. 2020. [Online]. Available: https://arc.aiaa.org/doi/10.2514/6.2020-2706

[28] S. C. Cakmakcioglu, O. Bas, and U. Kaynak, "A correlation-based algebraic transition model," *Proceedings of the Institution of Mechanical Engineers, Part C: Journal of Mechanical Engineering Science*, vol. 232, no. 21, pp. 3915–3929, Nov. 2018. [Online]. Available: http://journals.sagepub.com/doi/10.1177/0954406217743537

[29] W. Jones and B. Launder, "The prediction of laminarization with a two-equation model of turbulence," *International Journal of Heat and Mass Transfer*, vol. 15, no. 2, pp. 301–314, Feb. 1972. [Online]. Available: https://linkinghub.elsevier.com/retrieve/pii/0017931072900762

[30] F. R. Menter, "Two-equation eddy-viscosity turbulence models for engineering applications," *AIAA Journal*, vol. 32, no. 8, pp. 1598–1605, Aug. 1994. [Online]. Available: https://arc.aiaa.org/doi/10.2514/3.12149

[31] F. R. Menter, R. B. Langtry, and M. Kuntz, "Ten years of industrial experience with the SST turbulence model.pdf," 2003. [Online]. Available: https://cfd.spbstu.ru/agarbaruk/doc/2003_Menter,%20Kuntz,%20Langtry_Ten%20years%20of%20industrial%20experience%20with%20the%20SST%20turbulence%20model.pdf

[32] D. C. WILCOX, "Reassessment of the scale-determining equation for advanced turbulence models," *AIAA Journal*, vol. 26, no. 11, pp. 1299–1310, 1988. [Online]. Available: https://doi.org/10.2514/3.10041

[33] H. W. Emmons, "The laminar turbulent transition in a boundary layer," *J. Aero. Sci.*, vol. 18, no. 490, 1951.

[34] H. Schlichting and K. Gersten, *Boundary Layer Theory*, 1st ed. McGraw-Hill New York, 1955.

[35] J. Kendall, "Boundary layer receptivity to freestream turbulence." AIAA, Jun. 1990, p. 1504.

[36] Y. Kohama and W. S. Saric, "A high-frequency secondary instability of crossflow vortices that leads to transition." in *Boundary Layer Transition and Control, Proc. Conf, Cambridge*, 1991.

[37] Y. Kohama and D. Motegi, "Traveling disturbance appearing in boundary layer transition in a Yawed cylinder," *Experimental thermal and fluid science*, vol. 8, no. 4, pp. 273–278, 1994.

[38] A. Hatman and T. Wang, "Separated-Flow Transition: Part 1 Experimental Methodology and Mode Classification," in *ASME 1998 International Gas Turbine and Aeroengine Congress and Exhibition*. American Society of Mechanical Engineers, 1998, pp. V001T01A107–V001T01A107.

[39] B. J. Abu-Ghannam and R. Shaw, "Natural transition of boundary layers—the effects of turbulence, pressure gradient, and flow history," *Journal of Mechanical Engineering Science*, vol. 22, no. 5, pp. 213–228, 1980.

[40] R. B. Langtry, J. Gola, and F. R. Menter, "Predicting 2D airfoil and 3D wind turbine rotor performance using a transition model for general CFD codes," *AIAA paper*, vol. 395, 2006.

[41] R. Langtry, "Extending the Gamma-Rethetat Correlation based Transition Model for Crossflow Effects (Invited)." American Institute of Aeronautics and Astronautics, 2015. [Online]. Available: http://arc.aiaa.org/doi/10.2514/6.2015-2474

[42] R. D. Joslin, "AIRCRAFT LAMINAR FLOW CONTROLy," p. 29, 1998.

[43] H. Babinsky and J. Délery, "Transonic Shock Wave/Boundary-Layer Interactions," in *Shock Wave–Boundary-Layer Interactions*, H. Babinsky and J. K. Harvey, Eds. Cambridge: Cambridge University Press, 2011, pp. 87–136. [Online]. Available: http://ebooks.cambridge.org/ref/id/CBO9780511842757A010

[44] D. S. Dolling, "Fifty Years of Shock-Wave/Boundary-Layer Interaction Research: What Next?" *AIAA Journal*, vol. 39, no. 8, pp. 1517–1531, Aug. 2001. [Online]. Available: http://arc.aiaa.org/doi/10.2514/2.1476

[45] M. Robitail, E. Laurendeau, and A. Mosahebi, "Design of adaptive transonic laminar airfoils using the gamma Re theta t transition model," 2015.

[46] S. Barbarino *et al.*, "A Review of Morphing Aircraft," *Journal of Intelligent Material Systems and Structures*, vol. 22, no. 9, pp. 823–877, Jun. 2011. [Online]. Available: http://journals.sagepub.com/doi/10.1177/1045389X11414084

[47] A. Sofla *et al.*, "Shape morphing of aircraft wing: Status and challenges," *Materials & Design*, vol. 31, no. 3, pp. 1284–1292, Mar. 2010. [Online]. Available: http://linkinghub.elsevier.com/retrieve/pii/S0261306909004968

[48] M. S. Selig, M. D. Maughmer, and D. M. Somers, "Natural-laminar-flow airfoil for general-aviation applications," *Journal of Aircraft*, vol. 32, no. 4, pp. 710–715, Jul. 1995. [Online]. Available: http://arc.aiaa.org/doi/10.2514/3.46781

[49] A. Fluid Dynamics Panel, Ed., *Fluid Dynamics of three-dimensional turbulent shear flows and transition: Papers pres. and discussions at the Symposium*, ser. AGARD Conference Proceedings, Neuilly sur Seine, France, 1989, no. 438, oCLC: 20041606.

[50] A. M. O. Smith and N. Gamberoni, *Transition, Pressure Gradient and Stability Theory*. Douglas Aircraft Company, El Segundo Division, 1956, google-Books-ID: qXsxGwAA-CAAJ.

[51] D. Arnal, "Boundary layer transition: Predictions based on linear theory," Apr. 1994. [Online]. Available: http://adsabs.harvard.edu/abs/1994scpt.agar.....A

[52] N. Krimmelbein and A. Krumbein, "Automatic Transition Prediction for Three-Dimensional Configurations with Focus on Industrial Application," *Journal of Aircraft*, vol. 48, no. 6, pp. 1878–1887, 2011. [Online]. Available: https://doi.org/10.2514/1.C031230

[53] G. Bégou *et al.*, "Database Approach for Laminar-Turbulent Transition Prediction: Navier–Stokes Compatible Reformulation," *AIAA Journal*, vol. 55, no. 11, pp. 3648–3660, Nov. 2017. [Online]. Available: https://arc.aiaa.org/doi/10.2514/1.J056018

[54] R. B. Langtry and F. R. Menter, "Correlation-Based Transition Modeling for Unstructured Parallelized Computational Fluid Dynamics Codes," *AIAA Journal*, vol. 47, no. 12, pp. 2894–2906, 2009. [Online]. Available: http://arc.aiaa.org/doi/10.2514/1.42362

[55] F. R. Menter *et al.*, "A Correlation-Based Transition Model Using Local Variables—Part I: Model Formulation," *Journal of Turbomachinery*, vol. 128, no. 3, p. 413, 2006. [Online]. Available: http://Turbomachinery.asmedigitalcollection.asme.org/article.aspx?articleid=1467239

[56] K. Suluksna, P. Dechaumphai, and E. Juntasaro, "Correlations for modeling transitional boundary layers under influences of freestream turbulence and pressure gradient," *International Journal of Heat and Fluid Flow*, vol. 30, no. 1, pp. 66–75, 2009. [Online]. Available: https://linkinghub.elsevier.com/retrieve/pii/S0142727X0800146X

[57] N. Shengyang, "Extension of Transition Modeling by a Transport Equation Approach," PhD Thesis, DLR, 2017.

[58] C. Müller and F. Herbst, "Modelling of crossflow-induced transition based on local variables," *Proc. ECCOMAS, Paper*, no. 2252, 2014.

[59] S. Medida and J. Baeder, "A New Crossflow Transition Onset Criterion for RANS Turbulence Models." American Institute of Aeronautics and Astronautics, Jun. 2013. [Online]. Available: http://arc.aiaa.org/doi/10.2514/6.2013-3081

[60] S. Medida and J. D. Baeder, "Application of the correlation-based γ-$R_{e_{\theta t}}$ transition model to the Spalart-Allmaras turbulence model," in *20th AIAA Computational Fluid Dynamics Conference*. AIAA Reston, VA, 2011, pp. 1–21.

[61] M. Piotrowski, "Implementation and Investigation of a Local Correlation-based Transition Model in a Parallel Newton-Krylov-Schur Algorithm," Ph.D. dissertation.

[62] M. G. H. Piotrowski and D. W. Zingg, "Smooth Local Correlation-Based Transition Model for the Spalart–Allmaras Turbulence Model," *AIAA Journal*, vol. 59, no. 2, pp. 474–492, Feb. 2021. [Online]. Available: https://arc.aiaa.org/doi/10.2514/1.J059784

[63] H.-P. KREPLIN, H. MEIER, and A. MAIER, "Wind tunnel model and measuring techniques for the investigation of three-dimensional turbulent boundary layers," in *10th Aerodynamic Testing Conference*. American Institute of Aeronautics and Astronautics, 1978. [Online]. Available: https://arc.aiaa.org/doi/abs/10.2514/6.1978-781

[64] C. Seyfert and A. Krumbein, "Evaluation of a Correlation-Based Transition Model and Comparison with the eN Method," *Journal of Aircraft*, vol. 49, no. 6, pp. 1765–1773, Nov. 2012. [Online]. Available: http://arc.aiaa.org/doi/10.2514/1.C031448

[65] C. Grabe and A. Krumbein, "Extension of the γ-$R_{e_{\theta t}}$ Model for Prediction of Crossflow Transition." American Institute of Aeronautics and Astronautics, Jan. 2014. [Online]. Available: http://arc.aiaa.org/doi/10.2514/6.2014-1269

[66] D. Arnal, M. Habiballah, and E. Coustols, "Théorie de l'instabilité laminaire et critères de transition en écoulement bi et tridimensionnel," *La Recherche Aerospatiale*, vol. 2, pp. 125–143, 1984.

[67] J. H. Choi and O. J. Kwon, "Enhancement of a Correlation-Based Transition Turbulence Model for Simulating Crossflow Instability," *AIAA Journal*, vol. 53, no. 10, pp. 3063–3072, Oct. 2015. [Online]. Available: http://arc.aiaa.org/doi/10.2514/1.J053887

[68] ——, "Recent Improvement of a Correlation-Based Transition Model for Simulating Three-Dimensional Boundary Layers," *AIAA Journal*, vol. 55, no. 6, pp. 2103–2108, Jun. 2017. [Online]. Available: https://arc.aiaa.org/doi/10.2514/1.J055182

[69] J. Sa *et al.*, "Modeling and Prediction of the Crossflow Transition Using Transition Transport Equations." American Institute of Aeronautics and Astronautics, Jun. 2015. [Online]. Available: http://arc.aiaa.org/doi/10.2514/6.2015-3160

[70] Y. S. Jung and J. D. Baeder, "Gamma-Re-theta–SA with Crossflow Transition Model using Hamiltonian-Strand Approach." American Institute of Aeronautics and Astronautics, 2018. [Online]. Available: https://arc.aiaa.org/doi/10.2514/6.2018-1040

[71] N. Shengyang *et al.*, "Coupling of a Reynolds Stress Model with the gamma-Re-theta Transition Model," *AIAA Journal*, vol. 56, no. 1, pp. 146–157, 2018. [Online]. Available: https://arc.aiaa.org/doi/10.2514/1.J056167

[72] B. Eisfeld, "Implementation of Reynolds stress models into the DLR-FLOWer code," Jan. 2004.

[73] P. Ströer *et al.*, "Stability-Based Transition Transport Modeling for Unstructured Computational Fluid Dynamics at Transonic Conditions," *AIAA Journal*, pp. 1–13, Jun. 2021. [Online]. Available: https://arc.aiaa.org/doi/10.2514/1.J059892

[74] F. R. Menter *et al.*, "A One-Equation Local Correlation-Based Transition Model," *Flow, Turbulence and Combustion*, vol. 95, no. 4, pp. 583–619, Dec. 2015. [Online]. Available: http://link.springer.com/10.1007/s10494-015-9622-4

[75] L. Zhou *et al.*, "Improved k - omega - gamma model for crossflow-induced transition prediction in hypersonic flow," *International Journal of Heat and Mass Transfer*, vol. 115, pp. 115–130, Dec. 2017. [Online]. Available: http://linkinghub.elsevier.com/retrieve/pii/S0017931016344155

[76] S. Vallinayagam Pillai and S. Lardeau, "Accounting Crossflow Effects in One-Equation Local Correlation-Based Transition Model." American Institute of Aeronautics and Astronautics, Jun. 2017. [Online]. Available: https://arc.aiaa.org/doi/10.2514/6.2017-3159

[77] B. Lee and J. D. Baeder, "Prediction and validation of laminar-turbulent transition using SA-gamma transition model," in *AIAA Scitech 2021 Forum*. VIRTUAL EVENT: American Institute of Aeronautics and Astronautics, Jan. 2021. [Online]. Available: https://arc.aiaa.org/doi/10.2514/6.2021-1532

[78] J. Cagnone *et al.*, "Implicit multigrid schemes for challenging aerodynamic simulations on block-structured grids," *Computers & Fluids*, vol. 44, no. 1, pp. 314–327, 2011. [Online]. Available: https://linkinghub.elsevier.com/retrieve/pii/S0045793011000211

[79] B. Barrouillet, E. Laurendeau, and H. Yang, "On the calibration of the transitional k-omega-gamma-re-theta turbulence model," in *AIAA Scitech 2021 Forum*. American Institute of Aeronautics and Astronautics, 2021. [Online]. Available: https://arc.aiaa.org/doi/abs/10.2514/6.2021-0629

[80] F. R. Menter, R. Langtry, and S. Völker, "Transition Modelling for General Purpose CFD Codes," *Flow, Turbulence and Combustion*, vol. 77, no. 1-4, pp. 277–303, 2006. [Online]. Available: http://link.springer.com/10.1007/s10494-006-9047-1

[81] B. Barrouillet, E. Laurendeau, and H. Yang, "On the sensitivity of the rans-based correlation models to various parameters," in *3AF International Conference AERO 2021*. 3AF, 2021.

[82] A. Mosahebi and E. Laurendeau, "Convergence Characteristics of Fully and Loosely Coupled Numerical Approaches for Transition Models," *AIAA*, vol. 53, no. 5, 2015.

[83] K. Hasanzadeh, E. Laurendeau, and I. Paraschivoiu, "Grid-Generation Algorithms for Complex Glaze-Ice Shapes Reynolds-Averaged Navier–Stokes Simulations," *AIAA Journal*, vol. 54, no. 3, pp. 847–860, 2016. [Online]. Available: http://arc.aiaa.org/doi/10.2514/1.J054076

[84] K. Hasanzadeh Lashkajani, E. Laurendeau, and I. Paraschivoiu, "Adaptive curvature control grid generation algorithms for complex glaze ice shapes RANS simulations." American Institute of Aeronautics and Astronautics, 2015. [Online]. Available: http://arc.aiaa.org/doi/10.2514/6.2015-0914

[85] P. R. Spalart and C. L. Rumsey, "Effective inflow conditions for turbulence models in aerodynamic calculations," *AIAA journal*, vol. 45, no. 10, p. 2544, 2007.

[86] N. Krimmelbein, A. Krumbein, and C. Grabe, "Validation of Transition Modeling Techniques for a Simplified Fuselage Configuration." American Institute of Aeronautics and Astronautics, 2018. [Online]. Available: https://arc.aiaa.org/doi/10.2514/6.2018-0030

[87] J. A. Nelder and R. Mead, "A simplex method for function minimization," *The computer journal*, vol. 7, no. 4, pp. 308–313, 1965.

[88] V. Laarhoven, J. Peter, and E. H. Aarts, *Simulated annealing*. Springer, Dordrecht, 1987.

[89] M. Piotrowski and D. W. Zingg, "Investigation of a Local Correlation-based Transition Model in a Newton-Krylov Algorithm," in *AIAA Scitech 2019 Forum*. American Institute of Aeronautics and Astronautics, 2019. [Online]. Available: https://arc.aiaa.org/doi/10.2514/6.2019-2299

[90] J. G. Coder, "Further development of the amplification factor transport transition model for aerodynamic flows, AIAA SciTech forum," 2019.

[91] ——, "Standard Test Cases for CFD-Based Laminar-Transition Model Verification and Validation." American Institute of Aeronautics and Astronautics, 2018. [Online]. Available: https://arc.aiaa.org/doi/10.2514/6.2018-0029

[92] H. Sobieczky, "Configuration Test Cases for Aircraft Wing Root Design and Optimization," in *Proc. 2. Int. Symp. Inverse Problems, M. Tanaka (Ed.) Elsevier Science*, 1998.

[93] J. R. Dagenhart and W. S. Saric, "Crossow stability and transition experiments in swept wing flow," p. 150, 1999.

APPENDIX A RANS EQUATIONS

$$\frac{Dy}{Dt} = \frac{\partial y}{\partial t} + U.\nabla y \tag{A.1}$$

$$\tfrac{\partial \rho}{\partial t} + \nabla.(\rho U) = 0 \quad \Leftrightarrow \quad \tfrac{D\rho}{Dt} + \rho\nabla.(U) = 0 \tag{A.2}$$

$$\frac{\partial \rho U}{\partial t} + \nabla(\rho U \otimes U) = \nabla.\Sigma \tag{A.3}$$

$$\tfrac{\partial \rho U}{\partial t} + \nabla(\rho U \otimes U) = -\nabla p + \nabla.\tau \qquad \left(\tau = \mu\left[\nabla U + \nabla U^T - \tfrac{2}{3}\nabla.UI\right]\right) \tag{A.4}$$

$$\rho\frac{\partial U}{\partial t} + U\frac{\partial \rho}{\partial t} + \rho(U.\nabla U) + U\nabla.(\rho U) = -\nabla p + \nabla.\tau \tag{A.5}$$

$$(1.2, A.5) \Rightarrow \rho\frac{\partial U}{\partial t} + \rho(U.\nabla U) = -\nabla p + \nabla.\tau \tag{A.6}$$

$$\frac{\partial \rho U}{\partial t} + \nabla(\rho U \otimes U) = -\nabla p + \nabla.\left(\mu\left[\nabla U + \nabla U^T - \frac{2}{3}\nabla.UI\right]\right) \tag{A.7}$$

$$\begin{gathered} U = \overline{U} + u' \qquad U \otimes V = UV^T \qquad \overline{a\overline{U}} = a\overline{U} \qquad \overline{u'} = 0 \qquad \overline{au'} = \overline{a} \times \overline{u'} = 0 \\ \overline{\nabla U} = \nabla\overline{U} \qquad \overline{a+b} = \overline{a} + \overline{b} \qquad \overline{\overline{U}} = \overline{U} \end{gathered} \tag{A.8}$$

$$\frac{\partial \rho(\overline{U}+u')}{\partial t} + \nabla(\rho(\overline{U}+u') \otimes (\overline{U}+u')) = -\nabla p + \nabla.\left(\mu\left[\nabla(\overline{U}+u') + \nabla(\overline{U}+u')^T - \frac{2}{3}\nabla.(\overline{U}+u')I\right]\right) \tag{A.9}$$

$$\text{time average} \Rightarrow \nabla(\overline{\overline{\rho}(\overline{U}+u') \otimes (\overline{U}+u')}) = -\nabla\overline{p} + \nabla.\left(\overline{\mu}\left[\nabla\overline{(\overline{U}+u')} + \nabla\overline{(\overline{U}+u')^T} - \frac{2}{3}\nabla.\overline{(\overline{U}+u')}I\right]\right) \tag{A.10}$$

$$\Rightarrow \frac{\partial \overline{\rho}\overline{U}}{\partial t} + \nabla(\overline{\rho}(\overline{U}\overline{U}^T) + \overline{\rho}(u'u'^T)) = -\nabla\overline{p} + \nabla.\left(\overline{\mu}\left[\nabla\overline{U} + \nabla\overline{U}^T - \frac{2}{3}\nabla.\overline{U}I\right]\right) \tag{A.11}$$

$$\Rightarrow \tfrac{\partial \overline{\rho}\overline{U}}{\partial t} + \nabla(\overline{\rho}(\overline{U}\overline{U}^T) + \overline{\rho}(u'u'^T)) = -\nabla\overline{p} + \nabla.\overline{\sigma} + \nabla.\overline{\tau} \tag{A.12}$$

$$\overline{\sigma} = \left(\overline{\mu}\left[\nabla\overline{U} + \nabla\overline{U}^T - \tfrac{2}{3}\nabla.\overline{U}I\right]\right) \qquad \tau = -\overline{\rho u'u'^T} \tag{A.13}$$

$$\frac{\partial \overline{\rho}\overline{U_i}\overline{U_j}}{\partial x_j} = -\frac{\partial \overline{p}}{\partial x_i} + \frac{\partial}{\partial x_j}.\left(\overline{\mu}\left[\left(\frac{\partial \overline{U_i}}{\partial x_j} + \frac{\partial \overline{U_j}}{\partial x_i}\right) - \frac{2}{3}\frac{\partial \overline{U_k}}{\partial x_k}\delta_{ij}\right]\right) - \frac{\partial \overline{\rho u_i' u_j'}}{\partial x_j} \tag{A.14}$$

APPENDIX B LANGTRY MENTER 2009 MODEL EQUATIONS

$$\frac{\partial \rho\gamma}{\partial t} + \frac{\partial (\rho u_i \gamma)}{\partial x_i} - \frac{\partial}{\partial x_j}\left[\left(\mu_l + \frac{\mu_t}{\sigma_\gamma}\right)\frac{\partial \gamma}{\partial x_j}\right] = P_1 + P_2 - D_1 - D_2 \tag{B.1}$$

$$\frac{\partial \rho \tilde{R}e_{\theta t}}{\partial t} + \frac{\partial \left(\rho u_i \tilde{R}e_{\theta t}\right)}{\partial x_i} - \frac{\partial}{\partial x_j}\left[\sigma_{\theta t}\left(\mu_l + \mu_t\right)\frac{\partial \tilde{R}e_{\theta t}}{\partial x_j}\right] = P_3 - D_3 \tag{B.2}$$

With

$$\rho = \overline{\rho}\rho_\infty \qquad x = \overline{x}c \qquad u = \overline{u}\sqrt{RT_\infty} \quad P = \overline{P}P_\infty \quad t = \overline{t}\frac{\sqrt{RT_\infty}}{c} \quad \mu_l = \overline{\mu_l}\left(\rho_\infty c\sqrt{RT_\infty}\right)$$

$$\mu_t = \overline{\mu_t}\left(\rho_\infty c\sqrt{RT_\infty}\right) \quad K = \overline{K}RT_\infty \quad \omega = \overline{\omega}\frac{c}{\sqrt{RT_\infty}} \qquad \gamma = \overline{\gamma} \qquad Re_{\theta c} = \overline{Re_{\theta c}} \qquad \nu_l = \overline{\nu_l}\frac{\mu_{l\infty}}{\rho_\infty} \tag{B.3}$$

$$\hat{\nu} = \overline{\hat{\nu}}\frac{\mu_{l\infty}}{\rho_\infty}$$

$$\text{Non Dimensionalization Parameter: } \left(NDP = \frac{M\sqrt{\gamma}}{Re} = \frac{\mu_{l\infty}}{\rho_\infty\sqrt{RT_\infty}c}\right) \tag{B.4}$$

$$P_1 = F_{\text{length}}c_{a1}\rho S\left[\gamma F_{\text{onset}}\right]^{c_\alpha} \quad P_2 = c_{a2}\rho\Omega\gamma F_{\text{turb}} \quad P_3 = c_{\theta_t}\frac{\rho^2 u_i^2}{500\mu_l}Re_{\theta_t}(1 - F_{\theta_t})$$

$$D_1 = c_{e1}\gamma P_1 \qquad D_2 = c_{e2}\gamma P_2 \qquad D_3 = c_{\theta_t}\frac{\rho}{t}\tilde{R}e_{\theta_t}(1 - F_{\theta_t}) \tag{B.5}$$

$$F_{\text{length}} = F_{\text{length}}\left(1 - F_{\text{sublayer}}\right) + 40 * F_{\text{sublayer}} \quad F_{\text{sublayer}} = \exp\left(-\left(\frac{R_{e\omega}}{200}\right)^2\right)$$

$$R_{e\omega} = \frac{\rho\omega d^2}{\mu_l} = \frac{\overline{\rho\omega d^2}}{\overline{\mu_l}} \frac{\rho_\infty \sqrt{RT_\infty} c^2}{c\mu_{l\infty}} = \overline{R_{e\omega}} * \frac{1}{NDP} \qquad F_{\text{turb}} = \exp\left(-\left(\frac{R_T}{4}\right)^4\right) \tag{B.6}$$

$$R_T = \frac{\rho k}{\mu\omega} = \frac{\overline{\rho k}}{\overline{\mu\omega}} \frac{\rho_\infty RT_\infty}{\mu_\infty \frac{\sqrt{RT_\infty}}{c}} = \overline{R_T} \frac{1}{NDP}$$

$$F_{\text{onset}} = \max\left(F_{\text{onset2}} - F_{\text{onset3}}, 0\right) \qquad F_{\text{onset3}} = \max\left(1 - \left(\frac{R_T}{2.5}\right)^3, 0\right)$$

$$F_{\text{onset2}} = \min\left(\max\left(F_{\text{onset1}}, F_{\text{onset1}}^4\right), 2.0\right) \qquad F_{\text{onset1}} = \frac{R_{ev}}{2.193 R_{e\theta c}} \tag{B.7}$$

$$R_{ev} = \frac{\rho S d^2}{\mu} = \frac{\overline{\rho S d^2}}{\overline{\mu}} \frac{\rho_\infty \frac{\sqrt{RT_\infty}}{c} c^2}{\mu_\infty} = \overline{R_{ev}} \frac{1}{NDP}$$

$$F_{\theta t} = \min\left[\max\left(F_{\text{wake}} \exp\left(-\left(\frac{d}{\delta}\right)^4\right), 1 - \left(\frac{c_{e2}\gamma - 1}{c_{e2} - 1}\right)^2\right), 1\right] \quad F_{\text{wake}} = \exp\left[-\left(\frac{R_{e\omega}}{10^5}\right)^2\right] \tag{B.8}$$

$$\delta = \frac{375 * \Omega \mu_l R_{e\theta t} d}{\rho u_k u_k} = \overline{\delta} \times c \times NDP \qquad \frac{d}{\delta} = \frac{\overline{d}}{\overline{\delta}} \frac{c}{c \times NDP} = \frac{\overline{d}}{\overline{\delta}} \frac{1}{NDP}$$

$$R_{e\theta t} = \begin{cases} (1173.51 - 589.428Tu + 0.2196Tu^{-2}) F(\lambda_\theta), & Tu \le 1.3 \\ 331.50(Tu - 0.5658)^{0.671} F(\lambda_\theta), & Tu \ge 1.3 \end{cases} \tag{B.9}$$

$$F(\lambda_\theta) = \begin{cases} 1 + \left[12.986\lambda_\theta + 123.66\lambda_\theta^2 + 405.689\lambda_\theta^3\right] \exp\left(-\left(\frac{Tu}{1.5}\right)^{1.5}\right), & \lambda_\theta \le 0 \\ 1 + 0.275\left[1 - \exp(-35.0\lambda_\theta)\right] \exp\left(-\frac{Tu}{0.5}\right), & \lambda_\theta \ge 0 \end{cases} \tag{B.10}$$

$$\theta_t = \mu_l \frac{R_{e\theta t}}{\rho\sqrt{u_k u_k}} = \overline{\mu_l}\frac{R_{e\theta t}}{\overline{\rho}\sqrt{\overline{u_k u_k}}}\frac{\mu_{l\infty} c}{\rho_\infty \sqrt{RT_\infty} c} = \overline{\theta_t} \times NDP \times c$$

$$\lambda_\theta = \frac{\rho\theta_t^2}{\mu_l}\frac{dU}{ds} = \frac{\overline{\rho\theta_t^2}}{\overline{\mu_l}}\frac{d\overline{U}}{d\overline{s}}\frac{\rho_\infty c^2}{\mu_{l\infty}}\frac{\sqrt{RT_\infty}}{c} = \overline{\lambda_\theta}\frac{1}{NDP} \tag{B.11}$$

$$\lambda_\theta = \frac{\rho\theta_t^2}{\mu_l}\frac{dU}{ds} = \frac{\overline{\rho\theta_t^2}}{\overline{\mu_l}}\frac{d\overline{U}}{d\overline{s}}\frac{\rho_\infty c^2 NDP^2}{\mu_{l\infty}}\frac{\sqrt{RT_\infty}}{c} = \overline{\lambda_\theta}\frac{NDP^2}{NDP}$$

APPENDIX C NON DIMENSIONNALIZATION OF THE TRANSITION MODEL

$$P_1 = F_{\text{length}} c_{a1} \overline{\rho} \overline{S} \left[\gamma F_{\text{onset}}\right]^{c_\alpha} \frac{\rho_\infty \sqrt{RT_\infty}}{c} = \overline{P_1} \frac{\rho_\infty \sqrt{RT_\infty}}{c} \qquad P_2 = c_{a2} \overline{\rho} \overline{\Omega} \gamma F_{\text{turb}} \frac{\rho_\infty \sqrt{RT_\infty}}{c} = \overline{P_2} \frac{\rho_\infty \sqrt{RT_\infty}}{c}$$

$$P_3 = c_{\theta_t} \frac{\overline{\rho^2 u_i^2}}{500 \overline{\mu_l}} Re_{\theta_t} (1 - F_{\theta_t}) \frac{\rho_\infty^2 RT_\infty}{\mu_\infty} = \overline{P_3} \frac{\rho_\infty^2 RT_\infty}{\mu_\infty} \qquad D_1 = c_{e1} \gamma \overline{P_1} \frac{\rho_\infty \sqrt{RT_\infty}}{c} = \overline{D_1} \frac{\rho_\infty \sqrt{RT_\infty}}{c} \tag{C.1}$$

$$D_2 = c_{e2} \gamma \overline{P_2} \frac{\rho_\infty \sqrt{RT_\infty}}{c} = \overline{D_2} \frac{\rho_\infty \sqrt{RT_\infty}}{c} \qquad D_3 = c_{\theta_t} \frac{\overline{\rho^2 u_i^2}}{500 \overline{\mu_l}} \tilde{Re}_{\theta_t} (1 - F_{\theta_t}) \frac{\rho_\infty^2 RT_\infty}{\mu_\infty} = \overline{D_3} \frac{\rho_\infty^2 RT_\infty}{\mu_\infty}$$

$$\left(\frac{\partial \overline{\rho} \gamma}{\partial \overline{t}} + \frac{\partial (\overline{\rho u_i} \gamma)}{\partial \overline{x_i}}\right) \frac{\rho_\infty \sqrt{RT_\infty}}{c} - \frac{\partial}{\partial \overline{x_j}} \left[\left(\overline{\mu_l} + \frac{\overline{\mu_t}}{\sigma_\gamma}\right) \frac{\partial \gamma}{\partial \overline{x_j}}\right] \frac{\mu_{l\infty}}{c^2} = \overline{P_1} \frac{\rho_\infty \sqrt{RT_\infty}}{c} + \overline{P_2} \frac{\rho_\infty \sqrt{RT_\infty}}{c} - \overline{D_1} \frac{\rho_\infty \sqrt{RT_\infty}}{c} - \overline{D_2} \frac{\rho_\infty \sqrt{RT_\infty}}{c} \tag{C.2}$$

$$\Rightarrow \frac{\partial \overline{\rho} \gamma}{\partial \overline{t}} + \frac{\partial (\overline{\rho u_i} \gamma)}{\partial \overline{x_i}} - \frac{\partial}{\partial \overline{x_j}} \left[\left(\overline{\mu_l} + \frac{\overline{\mu_t}}{\sigma_\gamma}\right) \frac{\partial \gamma}{\partial \overline{x_j}}\right] \frac{\mu_{l\infty}}{\rho_\infty \sqrt{RT_\infty} c} = \overline{P_1} + \overline{P_2} - \overline{D_1} - \overline{D_2} \tag{C.3}$$

$$\Rightarrow \frac{\partial \overline{\rho} \gamma}{\partial \overline{t}} + \frac{\partial (\overline{\rho u_i} \gamma)}{\partial \overline{x_i}} - \frac{\partial}{\partial \overline{x_j}} \left[\left(\overline{\mu_l} + \frac{\overline{\mu_t}}{\sigma_\gamma}\right) \frac{\partial \gamma}{\partial \overline{x_j}}\right] NDP = \overline{P_1} + \overline{P_2} - \overline{D_1} - \overline{D_2} \tag{C.4}$$

$$\left(\frac{\partial \overline{\rho} \tilde{Re}_{\theta t}}{\partial \overline{t}} + \frac{\partial \left(\overline{\rho u_i} \tilde{Re}_{\theta t}\right)}{\partial \overline{x_i}}\right) \frac{\rho_\infty \sqrt{RT_\infty}}{c} - \frac{\partial}{\partial \overline{x_j}} \left[\sigma_{\theta t} \left(\overline{\mu_l} + \overline{\mu_t}\right) \frac{\partial \tilde{Re}_{\theta t}}{\partial \overline{x_j}}\right] \frac{\mu_{l\infty}}{c^2} = \overline{P_3} \frac{\rho_\infty^2 RT_\infty}{\mu_\infty} - \overline{D_3} \frac{\rho_\infty^2 RT_\infty}{\mu_\infty} \tag{C.5}$$

$$\Rightarrow \left(\frac{\partial \overline{\rho} \tilde{Re}_{\theta t}}{\partial \overline{t}} + \frac{\partial \left(\overline{\rho u_i} \tilde{Re}_{\theta t}\right)}{\partial \overline{x_i}}\right) - \frac{\partial}{\partial \overline{x_j}} \left[\sigma_{\theta t} \left(\overline{\mu_l} + \overline{\mu_t}\right) \frac{\partial \tilde{Re}_{\theta t}}{\partial \overline{x_j}}\right] \frac{\mu_{l\infty}}{\rho_\infty \sqrt{RT_\infty} c} = \overline{P_3} \frac{\rho_\infty \sqrt{RT_\infty} c}{\mu_{l\infty}} - \overline{D_3} \frac{\rho_\infty \sqrt{RT_\infty} c}{\mu_{l\infty}} \tag{C.6}$$

$$\Rightarrow \left(\frac{\partial \overline{\rho} \tilde{Re}_{\theta t}}{\partial \overline{t}} + \frac{\partial \left(\overline{\rho u_i} \tilde{Re}_{\theta t}\right)}{\partial \overline{x_i}}\right) - \frac{\partial}{\partial \overline{x_j}} \left[\sigma_{\theta t} \left(\overline{\mu_l} + \overline{\mu_t}\right) \frac{\partial \tilde{Re}_{\theta t}}{\partial \overline{x_j}}\right] NDP = \overline{P_3} \frac{1}{NDP} - \overline{D_3} \frac{1}{NDP} \tag{C.7}$$

APPENDIX D NON DIMENSIONALIZATION OF THE TURBULENCE MODEL

Non dimensionalization (Here,$\overline{\zeta}$ refers to the non dimensional value of a field ζ.):

$$\rho = \overline{\rho}\rho_\infty \qquad x = \overline{x}c \qquad u = \overline{u}\sqrt{RT_\infty} \quad P = \overline{P}P_\infty \quad t = \overline{t}\frac{\sqrt{RT_\infty}}{c} \quad \mu_l = \overline{\mu_l}\left(\rho_\infty c\sqrt{RT_\infty}\right)$$

$$\mu_t = \overline{\mu_t}\left(\rho_\infty c\sqrt{RT_\infty}\right) \quad K = \overline{K}RT_\infty \quad \omega = \overline{\omega}\frac{c}{\sqrt{RT_\infty}} \qquad \gamma = \overline{\gamma} \qquad Re_{\theta c} = \overline{Re_{\theta c}} \qquad \nu_l = \overline{\nu_l}\frac{\mu_{l\infty}}{\rho_\infty} \tag{D.1}$$

$$\hat{\nu} = \overline{\hat{\nu}}\frac{\mu_{l\infty}}{\rho_\infty}$$

$$\text{Non Dimensionalization Parameter: } \left(NDP = \frac{M\sqrt{\gamma}}{Re} = \frac{\mu_{l\infty}}{\rho_\infty\sqrt{RT_\infty}c}\right) \tag{D.2}$$

Non dimentionalizing the components of the F_1 fuction of the blending term of the ω equation:

$$\frac{500\nu}{d^2\omega} = \frac{500\overline{\nu}}{\overline{d}^2\overline{\omega}}\frac{c\mu_{l\infty}}{\rho_\infty c^2\sqrt{RT_\infty}} = \frac{500\overline{\nu}}{\overline{d}^2\overline{\omega}}NDP \qquad \frac{\sqrt{k}}{\beta\omega d} = \frac{\sqrt{\overline{k}}}{\beta\overline{\omega}\overline{d}} \tag{D.3}$$

$$CD_{k\omega} = \max\left(2\overline{\rho}\sigma_{\omega 2}\frac{1}{\overline{\omega}}\frac{\partial\overline{k}}{\partial\overline{x_j}}\frac{\partial\overline{\omega}}{\partial\overline{x_j}}, 10^{-20}\right)\frac{\rho_\infty c\sqrt{RT_\infty}^{-3}}{c^3\sqrt{RT_\infty}} = \overline{CD_{k\omega}}\frac{\rho_\infty\sqrt{RT_\infty}^{-2}}{c^2} \tag{D.4}$$

$$\frac{4\rho\sigma_{\omega 2}k}{CD_{k\omega}d^2} = \frac{4\overline{\rho}\sigma_{\omega 2}\overline{k}}{\overline{CD_{k\omega}}\overline{d}^2}\frac{\rho_\infty\sqrt{RT_\infty}^{-2}}{c^2}\frac{c^2}{\rho_\infty\sqrt{RT_\infty}^{-2}} = \frac{4\overline{\rho}\sigma_{\omega 2}\overline{k}}{\overline{CD_{k\omega}}\overline{d}^2} \tag{D.5}$$

Non dimentionalizing the k equation:

$$(1.9) \rightarrow (D.2) \Rightarrow \frac{\partial \overline{k}}{\partial \overline{t}} \frac{\sqrt{RT_\infty}^3}{c} + \frac{\partial \overline{U_i k}}{\partial \overline{x_i}} \frac{\sqrt{RT_\infty}^3}{c} = \frac{\overline{\mu_t}}{\overline{\rho}} \left(\left(\frac{\partial \overline{u_i}}{\partial \overline{x_j}} + \frac{\partial \overline{u_j}}{\partial \overline{x_i}} \right) - \frac{2}{3} \frac{\partial \overline{u_k}}{\partial \overline{x_k}} \delta_{ij} \right) \frac{\partial \overline{u_i}}{\partial \overline{x_j}} \frac{\mu_{l\infty} \sqrt{RT_\infty}^2}{\rho_\infty c^2} - \frac{2}{3} \overline{k} \delta_{ij} \frac{\partial \overline{u_i}}{\partial \overline{x_j}} \frac{\sqrt{RT_\infty}^3}{c} - \beta \overline{k} \overline{\omega} \frac{\sqrt{RT_\infty}^3}{c} + \frac{1}{\overline{\rho}} \frac{\partial}{\partial \overline{x_i}} \left[\left(\overline{\mu} + \sigma_k \overline{\mu_t} \right) \frac{\partial \overline{k}}{\partial \overline{x_i}} \right] \frac{\mu_{l\infty} \sqrt{RT_\infty}^2}{\rho_\infty c^2} \tag{D.6}$$

$$\Rightarrow \frac{\partial \overline{k}}{\partial \overline{t}} + \frac{\partial \overline{U_i k}}{\partial \overline{x_i}} = \frac{\overline{\mu_t}}{\overline{\rho}} \left(\left(\frac{\partial \overline{u_i}}{\partial \overline{x_j}} + \frac{\partial \overline{u_j}}{\partial \overline{x_i}} \right) - \frac{2}{3} \frac{\partial \overline{u_k}}{\partial \overline{x_k}} \delta_{ij} \right) \frac{\partial \overline{u_i}}{\partial \overline{x_j}} NDP - \frac{2}{3} \overline{k} \delta_{ij} \frac{\partial \overline{u_i}}{\partial \overline{x_j}} - \beta \overline{k} \overline{\omega} + \frac{1}{\overline{\rho}} \frac{\partial}{\partial \overline{x_i}} \left[\left(\overline{\mu} + \sigma_k \overline{\mu_t} \right) \frac{\partial \overline{k}}{\partial \overline{x_i}} \right] NDP \tag{D.7}$$

Non dimentionalizing the ω equation:

$$(1.9) \rightarrow (D.2) \Rightarrow \frac{\partial \overline{\omega}}{\partial \overline{t}} \frac{\sqrt{RT_\infty}^2}{c^2} + \frac{\partial \overline{U_i \omega}}{\partial \overline{x_i}} \frac{\sqrt{RT_\infty}^2}{c^2} = \frac{\gamma \overline{\mu_t}}{\overline{\rho \nu_t}} \left(\left(\frac{\partial \overline{u_i}}{\partial \overline{x_j}} + \frac{\partial \overline{u_j}}{\partial \overline{x_i}} \right) - \frac{2}{3} \frac{\partial \overline{u_k}}{\partial \overline{x_k}} \delta_{ij} \right) \frac{\partial \overline{u_i}}{\partial \overline{x_j}} \frac{\sqrt{RT_\infty}^2}{c^2} - \frac{\gamma}{\nu_t} \frac{2}{3} \overline{k} \delta_{ij} \frac{\partial \overline{u_i}}{\partial \overline{x_j}} \frac{\rho \sqrt{RT_\infty}^3}{\mu_l c} - \beta \overline{\omega}^2 \frac{\sqrt{RT_\infty}^2}{c^2} + \frac{1}{\overline{\rho}} \frac{\partial}{\partial \overline{x_i}} \left[\left(\overline{\mu_l} + \sigma_\omega \overline{\mu_t} \right) \frac{\partial \overline{\omega}}{\partial \overline{x_i}} \right] \frac{\mu_{l\infty} \sqrt{RT_\infty}}{\rho_\infty c^3} + 2 \left(1 - F_1 \right) \sigma_{w2} \frac{1}{\overline{\omega}} \frac{\partial \overline{k}}{\partial \overline{x_i}} \frac{\partial \overline{\omega}}{\partial \overline{x_i}} \frac{\sqrt{RT_\infty}^2}{c^2} \tag{D.8}$$

$$\Rightarrow \frac{\partial \overline{\omega}}{\partial \overline{t}} + \frac{\partial \overline{U_i \omega}}{\partial \overline{x_i}} = \frac{\gamma \overline{\mu_t}}{\overline{\rho \nu_t}} \left(\left(\frac{\partial \overline{u_i}}{\partial \overline{x_j}} + \frac{\partial \overline{u_j}}{\partial \overline{x_i}} \right) - \frac{2}{3} \frac{\partial \overline{u_k}}{\partial \overline{x_k}} \delta_{ij} \right) \frac{\partial \overline{u_i}}{\partial \overline{x_j}} - \frac{\gamma}{\nu_t} \frac{2}{3} k \delta_{ij} \frac{\partial \overline{u_i}}{\partial \overline{x_j}} \frac{1}{NDP} - \beta \overline{\omega}^2 + \frac{1}{\overline{\rho}} \frac{\partial}{\partial \overline{x_i}} \left[\left(\overline{\mu_l} + \sigma_\omega \overline{\mu_t} \right) \frac{\partial \overline{\omega}}{\partial \overline{x_i}} \right] NDP + 2 \left(1 - F_1 \right) \sigma_{w2} \frac{1}{\overline{\omega}} \frac{\partial \overline{k}}{\partial \overline{x_i}} \frac{\partial \overline{\omega}}{\partial \overline{x_i}} \tag{D.9}$$